Mechanical Behavior and Microstructure of Reactive-Air-Brazed Metal/Ceramic Joints

Chichi Li

Mechanical Behavior and Microstructure of Reactive-Air-Brazed Metal/Ceramic Joints

Von der Fakultät für Maschinenwesen der Rheinisch-Westfälischen Technischen Hochschule Aachen zur Erlangung des akademischen Grades einer Doktorin der Ingenieurwissenschaften genehmigte Dissertation

vorgelegt von

Chichi Li

Berichter: Univ.-Prof. Dr.-Ing. Tilmann Beck
Univ.-Prof. Dr.-Ing. Lorenz Singheiser

Tag der mündlichen Prüfung: 08.10.2013

Diese Dissertation ist auf den Internetseiten der Hochschulbibliothek online verfügbar.

Abstract

The microstructure evolution dependent deformation and damage mechanisms of reactive air brazed metal/ceramic joints were studied under long term isothermal / thermal cycling conditions.

The mechanical behavior and microstructural properties of joints produced using three Ag-base brazes, i.e. a Cu-containing braze (Ag4Cu, as a state of the art SOFC metal braze), an Al-containing (Ag0.5Al, as a newly developed advanced braze) and a pure Ag braze were compared. Ambient temperature delamination, high temperature shear and thermal cycling tests were applied to characterize the thermomechanical properties of the joints.

The interfaces prove to be the weakest link of the joints in ambient temperature delamination testing. The long-term operability of the joints was found to be limited by aging induced degradation of the braze/steel and/or the braze/ceramic interfaces.
In high temperature shear testing, competing failure of the interfaces and the braze matrix was discovered. Aging in air strengthened both the interface and the braze matrix, thus enhancing the high temperature shear and creep resistance of the joints.
Thermal cycling induced mechanical twinning of the initially single crystalline matrices of the Ag and the Ag4Cu braze, which in turn promotes recrystallization of the matrix. Both processes compensate thermal mismatch stresses arising from temperature change and thermal expansion coefficient mismatch. With the introduction of an initially polycrystalline matrix - in case of an advanced Ag0.5Al braze - both mechanisms were exploited to reach greatly increased resistance against rapid thermal cycling.

Considering the progress achieved by the advanced Ag0.5Al braze in thermal stress compensation, it could be stated that reactive air brazes have great potential especially for rapid thermal cycling application. Nevertheless brazing properties and thermomechanical stability still need further improvement. Future R&D activities in reactive air brazing should focus on joint stability during combined long term thermal cycling operation under dual atmosphere conditions.

Zusammenfassung

Die Verformungs- und Schädigungsmechanismen reaktivgelöteter Metall / Keramik-Verbindungen wurden mittels Analyse der Mikrostrukturentwicklung während isothermer Langzeitauslagerung und schneller Thermozyklen untersucht. Hierbei wurden das mechanische Verhalten und die Mikrostruktur von Lötverbindungen, mittels eines Cu-haltigen Metalllots (Ag4Cu, Stand der Technik für Lötungen in SOFC-Systemen), eines Al-haltigen Lotes (Ag0.5Al, neu entwickelt) und eines reinen Ag-Lotes hergestellter Metall/Keramik-Verbundproben verglichen. Vierpunktebiegungstests, Doppelscherversuche und Thermozyklierversuche wurden angewendet, um die thermomechanischen Eigenschaften der Lötverbindungen zu charakterisieren. Im Vierpunktbiegeversuch bei Raumtemperatur versagen alle Varianten an den Grenzflächen. Die Lebensdauer der Fügungen bei Langzeit-Warmauslagerung wird durch Degradation der Lot/Stahl- und/oder Lot/Keramik-Grenzflächen begrenzt. In den Hochtemperaturdoppelscherversuchen waren konkurrierende Schädigung der Grenzflächen und der Lotmatrix versagensbestimmend. Eine Warmauslagerung in Luft erhöht die Scherfestigkeit der Grenzflächen und der Lotmatrix und damit den Widerstand der gesamten Fügung gegen Scherbelastung.

Thermozyklen induzieren mechanische Zwillingsbildung in der ursprünglich einkristallinen Matrix der Ag und der Ag4Cu Lote, und resultieren im weiteren Verlauf in einer Rekristallisation der Matrix. Durch beide Mechanismen werden thermisch induzierte Spannungen abgebaut. Bei Vorliegen einer bereits im Ausgangszustand polykristallinen Matrix, wie im Falle des Ag0.5Al Lots, treten beide Mechanismen verstärkte auf und erhöhen deutlich die Lebensdauer der Verbindung bei schneller Temperaturwechselbelastung.

Diese mit der Lotvariante Ag0.5Al gegenüber den anderen Varianten erreichten Fortschritte, zeigen, dass das Reaktivlöten großes Potenzial für die Herstellung von Bauteilen hat, die schnellen Temperaturwechseln unterliegen. Künftige F&E-Aktivitäten zum Reaktivlöten sollten auf eine erhöhte Stabilität im kombinierten Langzeitbetrieb mit Temperaturwechseln unter Dualatmosphäre abzielen.

Contents

1. Introduction 1
1.1 Motivation 1
1.2 Scope of the work 2
2. Fundamentals 3
2.1 Solid Oxide Fuel Cells (SOFCs) 3
2.1.1 Working principle of an SOFC 3
2.1.2 Cell and Stack design 4
2.1.3 Basic components of planar SOFC stacks 5
2.2 Requirements for joining techniques 7
2.3 Current state of the art 9
2.3.1 Glass bonding 9
2.3.2 Active metal brazing 9
2.3.3 Reactive air brazing 10
2.3.4 Diffusion bonding 11
2.4 Material properties of candidate joining partners 11
2.4.1 Ceramics 11
2.4.2 Steels 13
2.5 Thermomechanical properties of Ag-based braze systems 15
2.5.1 The Ag-O system 15
2.5.2 The Ag-Cu system 22
2.5.3 The Ag-Al system 24
2.6 Mechanical behavior of the braze matrix 25
2.6.1 High temperature creep 25
2.6.2 Stress relaxation 27
2.6.3 Thermal fatigue 28
2.6.4 Nucleation criteria for recrystallization 29
3. Experimental 31
3.1 Materials 31
3.1.1 Braze 31
3.1.2 Joining partners 32
3.2 Brazing process 33

3.2.1 Temperature program....33
3.2.2 Brazing tools....34
3.3 Aging treatment....34
3.3.1 Isothermal annealing....34
3.3.2 Thermal cycling....35
3.4 Room temperature delamination testing....36
3.4.1 Sample geometry....37
3.4.2 Execution of tests....38
3.4.3 Data evaluation....40
3.5 High temperature double shear testing....41
3.5.1 Sample geometry....41
3.5.2 Execution of tests....42
3.5.3 Data evaluation....43
3.5.4 Correction of machine deformation....44
4. Results and discussion....47
4.1 Interfacial adhesion: As-brazed state....47
4.1.1 Steel/braze interface....47
4.1.2 Ceramic/braze interface....56
4.1.3 Discussion and conclusions....58
4.2 Interfacial adhesion: Aged....60
4.2.1 Aging in air....60
4.2.2 Aging in reducing atmosphere (Ar4Vol%H_2)....65
4.2.3 Discussion and conclusions....72
4.3 High temperature mechanical behavior....73
4.3.1 Constant deformation rate tests (CDRT)....73
4.3.2 Stress relaxation....79
4.3.3 Conclusions....82
4.4 Interface and matrix performance after thermal cycling....82
4.4.1 Strength degradation caused by interfacial delamination....83
4.4.2 Strength degradation caused by braze matrix deformation....86
4.4.3 Stress accommodation and redistribution during thermal cycling....87
4.4.4 Twinning and recrystallization....90
4.4.5 Discussion and conclusions....96

5. Conclusions and outlook 97
References 99

1. Introduction

1.1 Motivation

Potentially highly efficient energy conversion systems like high temperature solid oxide fuel cells (SOFCs) have gained increasing interest during the last decades, because of the increasing energy demand of the world, rising energy prices and the shortening of fossil fuels. SOFCs offer efficiencies of about 50 % in transforming chemical energy into electricity [Ste01]. Their envisaged fields of application range from stationary household combined heat and power supply, to decentralized power plants and automotive applications in so called auxiliary power units (APUs) for vehicles.

For successful, reliant long-term operation, hermetic sealing of the electrochemically active all-ceramic fuel cell to the metallic housing is crucial. Hence, joining is recognized as a key enabling technology for the future commercialization of ceramic high temperature fuel cell systems. Thermal cycling capability, which is necessary for mobile SOFC application, is a comparatively new challenge in SOFC sealing technology. Traditionally applied glass seals are comparatively sensitive to rapid temperature changes in combination with thermal expansion mismatches of the joining partner materials [Kim07b]. Research and development therefore extended from conventional glass sealing to metal brazing in the recent years.

Reactive air brazing (RAB) as a relatively novel brazing technique, which was specifically developed for application in high temperature electrochemical devices and offers ease of processing and high tolerance to rapid temperature changes. Earlier research revealed the outstanding potential of this technique for application in especially mobile SOFC systems. Nevertheless, thermomechanical and thermochemical stability of the braze joints need further optimization and fundamentals and basic principles of this brazing technique still remain unclear.

To study the fundamentals of reactive air brazing, a cooperative research project, funded by the Deutsche Forschungsgemeinschaft (DFG), was established between Forschungszentrum

Jülich GmbH (IEK-2), RWTH Aachen University and ACCESS e.V.. This thesis outlines part of the Jülich contribution on basic mechanical, damage and failure behavior of reactive air brazed joints for SOFC application.

1.2 Scope of the work

This thesis mainly focuses on the application of reactive air brazes for automotive SOFC application. For this kind of application maximum thermomechanical stability in high temperature long-term, cyclic operation is mandatory.

Previous research [Kuh08, Bra12] revealed satisfactory as-brazed properties of Ag-base braze joints of Crofer 22APU (typical SOFC interconnect material) and SOFC electrolyte materials, but the adhesion, damage and failure mechanisms still remained unclear. As a consequence, mechanism oriented research, especially concerning the influence of microstructure and microstructural changes (either caused by intentional changes in braze composition and/or aging during isothermal / thermal cycling operation) on the mechanical performance, moved in the focus of recent research.

Basic understanding of the fundamentals of reactive air brazing is mandatory for further goal oriented improvement of brazes, brazing partners and the brazing process. The microstructural and mechanical properties of three braze systems in combination with the high chromium ferritic steel Crofer® 22 H (an advanced version of Crofer® 22 APU, both developed at FZ Jülich, IEK-2 especially for SOFC application) and SOFC electrolyte materials were studied in this thesis. The testing methods and parameters were chosen according to “real-life” operation conditions of mobile application SOFCs. The investigations mainly focused on the influence of microstructure and microstructural changes on the ambient and high temperature mechanical as well as cyclic thermomechanical performance.

2. Fundamentals

2.1 Solid Oxide Fuel Cells (SOFCs)

A solid oxide fuel cell (SOFC) is a solid-state power converter that directly converts the chemical energy of fossil fuels into electricity without combustion and mechanical processes [Liu08]. It enables an efficient and thus environmentally acceptable use of the available energy resources and have been extensively studied in the past decades as a promising power conversion technology with high efficiency, low emission level and fuel flexibility [Fer05]. It can operate within a wide range of temperatures from 500 ℃ to 1000 ℃ [Ste01]. Electrical power can range from a few kilowatts to megawatts [Tie03]. Its potential application fields lie in distributed heat and power generation, domestic combined heat and power (CHP) systems and auxiliary power units (APU) for transportation applications [Blu07].

2.1.1 Working principle of an SOFC

The electrochemical reaction takes place between a fuel gas (e.g. hydrogen) and in most cases atmospheric oxygen. During operation, oxygen ions are transported from the cathode (air) side through an ion-conducting electrolyte to the anode (fuel) side, where the oxygen reacts with the hydrogen of the fuel gas to form water. Meanwhile, electrons are released which can be used in an external electric circuit [Meu03]. The driving force for the diffusion is the oxygen concentration gradient across the electrolyte. The oxygen partial pressure is about 0.2 bar (if air of 1bar is used) at the air side and approximately 10^{-18} bar at the fuel side [Fro08]. The working principle of an SOFC is schematically shown in Fig. 2.1.

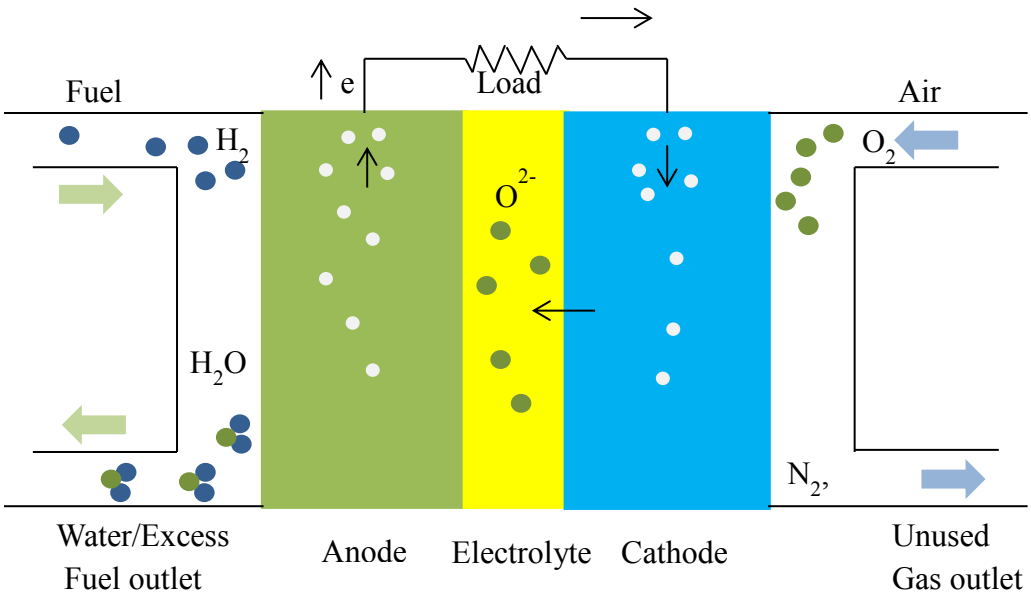


Fig. 2.1 Schematic view of the working principle of a solid oxide fuel cell [Rya12]

2.1.2 Cell and Stack design

For the cell design, two main concepts are under development: The tubular and the planar design [Mal09, Blu07]. A single cell typically provides a voltage of about 0.9 – 0.7 volts and for this reason several cells have to be connected in series (by so called "stacking") to reach technically reasonable output voltages. Stacks of both design concepts consist of several single cells ("stacking units"). The tubular design does not require any high temperature sealing and is more stable in long term operation. On the other hand, the planar design is more cost-effective in manufacturing and offers higher volumetric and gravimetric power density [Mal09, Fro08].

Depending on the application, tubular SOFCs have dimensions from small diameter (1 - 2 mm), needle-like shapes (length: 5 – 15 cm) to diameters of a few centimeters and lengths of about 1.5 – 2 m for rapid start-up times and high gross power, respectively [Van00, Sin97]. In planar design, there are mainly two supporting concepts: The electrolyte supported design and the electrode supported design (Fig. 2.2). For electrolyte supported cells, the thickness of the electrolyte varies within the range of 150 – 250 µm [Tie03]. The operating temperatures of this concept are 850 °C – 1000 °C due to the relatively high ohmic resistance of the thick electrolyte [Blu05]. The electrolyte thickness is reduced to about 10 µm in electrode supported cells [Tie03]. With the thickness reduction of the electrolyte, intermediate operating temperatures (650 °C – 800 °C) are sufficient [Tie03]. The currently most favored

electrode supported design is the anode-supported one, because it generically has low electrical resistance. Therefore, only insignificant increase in ohmic resistance is incurred by increasing the electrode thickness [Blu05]. The general tendency today is in favor of cell designs with thin electrolytes to achieve lower ohmic resistance and hence high power density and low operating temperature (500 – 800 ℃) [Men10].

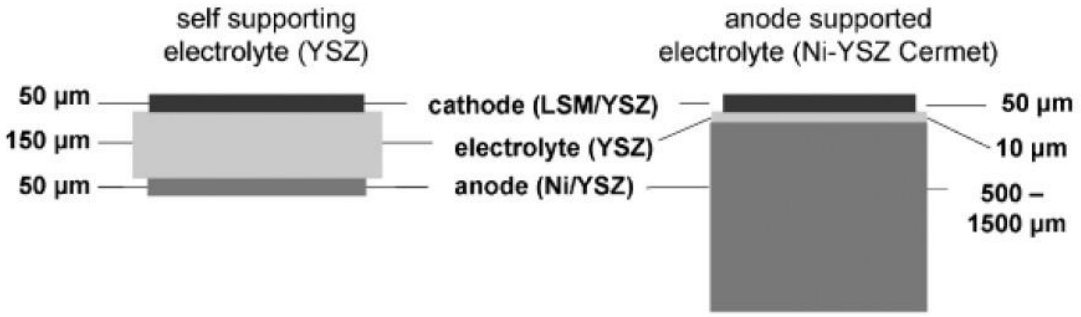


Fig. 2.2 Anode–supported cell concept (right) compared with the electrolyte-supported (left) [Blu05]

2.1.3 Basic components of planar SOFC stacks

Cathode, electrolyte and anode are the basic components of a single cell. Each single layer has to fulfill special demands, which will be outlined in the following.

- **Cathode**

For reliable SOFC operation, the cathode material has to provide

1. high mixed ionic and electronic conductivity at operating temperature,
2. high electrocatalytic activity,
3. thermochemical stability and compatibility with the electrolyte material.

Perovskite materials are frequently utilized as cathodes due to their mixed ionic and electronic conductivity [Ski01]. A frequently used cathode material is strontium-doped lanthanum manganite (La,Sr)MnO_3 (LSM) [Hol02, Juh96, Men10]. Another popular cathode material is (La,Sr)CoO_3 (LSC), which offers higher electronic conductivity than the conventional LSM material [Cha99]. However, it is more reactive with YSZ (the typical electrolyte material) and forms an intermediate phase ($La_2Zr_2O_7$ or $SrZrO_3$ [Uch08]). Furthermore it exhibits higher thermal expansion incompatibility with YSZ [Ski01, Mag00]. Currently the cell development works towards incorporating an additional interfacial doped

ceria (CeO_2) layer between the cathode and the electrolyte material, which not only increases the cell performance, but also acts as a barrier to reaction between YSZ and the cathode [Sim03, Cha99]. Generally, the cathode has to be highly porous to allow rapid gas transport and to provide increased reaction surface area.

- **Electrolyte**

SOFCs utilize solid oxide ion conductors as electrolyte materials. In order to achieve good cell performance, the materials have to possess sufficient ionic conductivity for O^{2-} ions as well as very low electronic conductivity to reduce internal short-circuit losses at operating temperature [Men10, Fro08]. Besides, it has to be gas-tight and stable in both oxidizing and reducing atmosphere [Fro08, Kuh08]. The nowadays most extensively applied electrolyte material is yttria-doped ZrO_2 (YSZ) [Ste01]. Yttrium doping stabilizes the tetragonal phase of zirconia and leads to an increase in oxygen vacancy concentration [Fro08], thus leading to higher oxygen ion conductivity. Other materials like ceria-based (e.g. CGO) or doped $LaGaO_3$ (LSGM) are gaining research interest as candidate electrolytes especially for low temperature SOFC applications (~ 500 ℃) [Tie03].

- **Anode**

Similar to the cathode material, the anode material has to possess good electrical and ionic conductivity, good gas permeability as well as excellent electrocatalytic properties [Men10]. The most commonly applied anode material is Ni/YSZ cermet (ceramic-metal), which is a ceramic-metal composite material [Kuh08]. The anode is manufactured as a mixture of nickel oxide and YSZ powder and is reduced to Ni/YSZ during the start-up phase of the cell or stack by the prevailing reducing fuel atmosphere [Men10]. Nickel, finely dispersed around the YSZ particles, serves as a catalyst for the oxidation of hydrogen. The zirconia skeleton not only mechanically stabilizes the porous electrode structure, but also creates an extended reaction zone by increasing the amount of triple phase boundaries and helps to accommodate the thermal expansion coefficients of the anode substrate and the electrolyte layer [Men10]. The overall performance and reliability of the anode can be enhanced by a bilayer design, which employs differing microstructures: A thin anode functional layer as the electrochemically active region and a thick anode substrate, which mainly serves as a current collector and conductor as well as mechanical support [Blu07]. Degradation of Ni/YSZ anodes mainly occurs by re-oxidation of Ni, sulfur poisoning and coking caused by the fuel gas decomposition [Blu07]. Volume changes are associated with the oxidation and reduction of the Ni contained in the anode induces cracking during operation [Ste01]. Besides,

contaminants contained in the fuel gas or insufficient amounts of water for internal reformation of methane would induce sulfur poisoning and coking of the anode material [Men10].

Additionally, planar SOFC stacks comprise several, mostly metallic, components like cell support frames, support inlays, gas distributors and interconnect sheets (Fig. 2.3).

- Interconnect

The interconnect sheet electrically connects the single cells of planar SOFC stacks and separates the anode and cathode gas compartments from each other [Fro08]. Both, ceramic and metallic materials have been used as interconnect materials. Because the current SOFC development favors lower operating temperatures, metallic interconnects are preferred [Men10]. Ceramic interconnects were manufactured from $LaCrO_3$-type materials, because it is one of very few perovskites that do not decompose in typical fuel gas atmospheres [Men10]. However, it can not be used at temperatures lower than 800 °C, because of its low electrical conductivity. Metallic interconnects on the other hand have high electronic and thermal conductivity combined with lower production costs [Blu07]. Nevertheless, corrosion resistance remains an important issue for long-term operation of metallic interconnects. The reduction of chromium evaporation to avoid detrimental poisoning of the cathode is still the main focus of further development [Tie03].

2.2 Requirements for joining techniques

In the light-weight planar SOFC stack design of Forschungszentrum Jülich, gastight seals must be applied along the edges of each single cell to join the cell to the cell-frames (cell/cell-frame joint, Fig. 2.3). The cell-frames are laser-welded to the interconnect sheets to form the so called “repeating unit”. Several of these repeating units are joined by sealing along their outer edges to provide an internal cathode manifold (cell-frame/interconnect joint, Fig. 2.3).

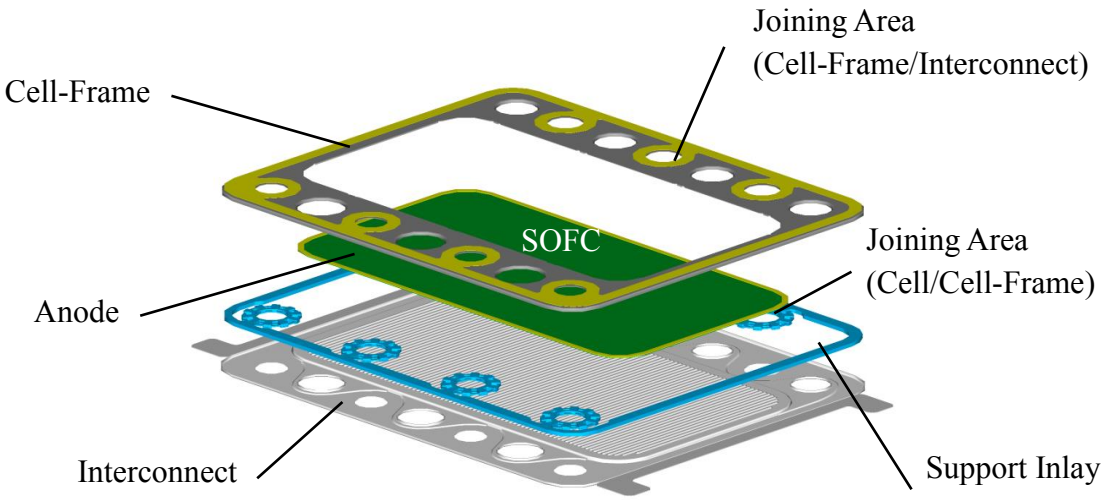


Fig. 2.3 Schematic "explosion" drawing of a repeating unit in light-weight planar SOFC-design [Kuh08]

Typical operating conditions of planar SOFCs are [Wei05a]: An average operating temperature of approximately 750 ℃, continuous exposure to oxidizing atmosphere (air) at the cathode side and a wet, reducing atmosphere (H_2, containing H_2O) at the anode side and an anticipated lifetime of approximately 15000 h for automotive and more than 40000 h for stationary applications. Therefore, to fulfill all the above mentioned operating conditions, there are several requirements that need to be met by the sealing material (Tab.1 [Mah10]).

Tab. 2.1 Properties and fabrication requirements of SOFC sealants [Mah10]

Properties	Requirements
Thermal properties	Thermal expansion coefficient of 9.5-12.0 ppm/K; thermally stable for ~ 15000 h for mobile applications and for ~ 50000 h for stationary application at 650 ℃ - 900 ℃
Chemical properties	Resistance to vaporization and compositional change in stringent oxidizing and wet reducing atmospheres at 650 ℃ – 900 ℃; limited or no reaction with other cell/stack components
Mechanical properties	Resistance to external static and dynamic forces during transportation and operation; Thermal cycling capability
Electrical properties	Electrical resistivity greater than 500 Ωcm between cells and stacks at nominal stack operating condition (0.7 V at 500 - 700 mA/cm^2)
Sealing requirements	Sealing load < 35 kPa; withstand differential pressure up to 14 – 35 kPa
Fabrication flexibility	flexible design, low processing cost, and high reliability

2.3 Current state of the art

A number of joining techniques like glass joining and active metal brazing are currently used, but each technique suffers some form of trade-off or exhibits some penalty in terms of joint properties, ease of processing, and/or cost [Kim07a].

2.3.1 Glass bonding

Glass bonding is a relatively simple, cost-effective joining method [Kim08, Wei05b]. Glasses and glass ceramics are nowadays the most widespread sealing materials in planar SOFCs [Göd11]. BaO-CaO-Al_2O_3-SiO systems are the common filler materials for glass joining [Kuh08]. During joining above the transition temperature, the glass changes from brittle to ductile behavior, by which sufficient material flow provides an adequate joint. During the joining process, the glass might partially or fully crystallize to form a rigid, bonded seal, which is typically mechanically stronger than the initial glass [Zha11].

However, glass joints are very sensitive to thermomechanical loading. The biggest problem is the brittle nature of the final joint and the resulting problems concerning thermal expansion mismatches, which ultimately affect the longevity and thermal cycling performance of glass sealed joints [Kim07b]. Another problem of glass joining is the reactivity of glass ceramic sealants with the metallic stack components [Zha11]. Interfacial reaction products with the oxide scales of the metallic interconnect might form and grow at the typical stack operating temperatures, leading to porous interfaces that may be mechanically weak and thus susceptible to thermomechanically induced cracking [Zha11].

2.3.2 Active metal brazing

Active metal brazing is a typical method of joining ceramics and metals in engineering. Because of poor wetting of the ceramic by the braze filler, reactive elements like Titanium and/or Zirconium [Wei03, Wei05b] are often employed in the filler metal, which can drastically lower the contact angle of the filler onto the ceramic and in addition improve adhesion by reacting with the oxide that constitutes the main phase of the ceramic [Sci01]. This brazing technique requires stringent atmospheric control, either high vacuum or inert cover gas, during joining to prevent the active elements from oxidation. These requirement leads to comparatively high investment and operating costs [Kim05].

For SOFC application, there are two major problems concerning active metal brazing processes: First, the active metal braze joints exhibit weak oxidation resistance during high temperature operation of the fuel cell stack [Wei03]. Complete oxidation of the active species in the braze in air may lead to rapid deterioration of the joint at the ceramic/braze interface accompanied by an eventual loss of hermeticity [Wei05b, Kim05].

Atmosphere sensitivity of the joining partners poses another problem. Recent research shows that exposure of an entire fuel cell to a reducing atmosphere at a temperature greater than 800 ℃ (typical processing temperatures in active metal brazing are higher than 1000 ℃) is deleterious to many of its complex oxides, like the cathode and anode materials [Wei05b]. It is proved that under the real brazing condition of active metal brazing, irreversible damage of the perovskite structure and reduced electrical conductivity as well as catalytic activity would be caused to the cathode materials [Kuh08]. Besides, reduction of the anode (e.g. NiO_x) during vacuum brazing and re-oxidation in following stack production or operation would cause damage of the cell [Ste01]. Therefore, active metal brazing is only suitable in combination with reduction-tolerant cathode and re-oxidation tolerant anode materials.

2.3.3 Reactive air brazing

Reactive air brazing is a comparatively new brazing technique, specifically developed for application in high temperature electrochemical devices [Wei05b]. The process is conducted in air without the need of an inert cover gas [Wei05c]. Therefore, the final joint is comparatively resistant to oxidation at high temperatures [Wei03]. The braze filler material typically consists of two ingredients, a noble metal and an oxide compound. The oxide compound is added to reactively alternate the oxide faying surface and to help the remaining molten filler material to wet on it [Kim07a]. For this brazing technique, bonding strength depends on a thin, well adhering oxide scale, that forms on the metal component during heating [Wei05a, Wei05b].

A number of metal oxide/noble metal systems like Ag-CuO, Ag-V_2O_5 and Pt-Nb_2O_5 [Wei05c] were considered for RAB. Ag-based filler metals can be used for high temperature electrochemical devices, because of its ductility and compliance, even though there is a significant mismatch in the coefficient of thermal expansion between silver (20.6×10^{-6}/K) and ceramic components like yttria-stabilized zirconia (YSZ, 10.5×10^{-6}/K) [Kim07a]. For SOFC application, reactive air brazing shows a number of advantages in comparison to

conventional active metal brazing and glass bonding: RAB would not cause any atmosphere induced damage to the joining partners (cell/stack components) during processing. The high ductility of the braze filler offers better tolerance to thermal expansion mismatches during cyclic operation. Nevertheless, technological brazing properties like pore formation and contour accuracy as well as the thermomechanical stability are still under optimization for industrial application.

2.3.4 Diffusion bonding

Diffusion bonding is a process that produces solid-state coalescence between two materials by applying pressure at a temperature below the melting points of the materials to be joined [Elr09]. The applied compression stress should be lower than the yield strength of the joining partner materials at bonding temperature [Bas12]. Because the bonding process is conducted in solid state, the contour accuracy of the joint is excellent and pore formation in the braze matrix can be avoided. Nevertheless, because of the pressure requirement, components fabricated by diffusion bonding are typically limited to simple shapes [Kim05]. Serier et al. investigated the effects of several bonding parameters on the strength of solid state bonded silver/alumina joints [Ser11a, Ser11b]. It was found that pressure, time and temperature of bonding, as well as the oxygen content of the braze greatly affect the joint strength. In conclusion, diffusion bonding can be quite effective and yields good joint properties. However, the requirement of certain pressure during bonding does limit the application of this technique.

2.4 Material properties of candidate joining partners

2.4.1 Ceramics

Ceramics have excellent strength, high wear and corrosion resistance at elevated temperatures and a variety of electrical properties [LiJ02]. Nevertheless, most of the ceramics are difficult and expensive to fabricate, especially regarding large and/or complex shaped components [Han00]. As the use of ceramic components for structural, electrical and electronic applications is rapidly increasing, high requirements arise for the joining techniques for bonding ceramics either to themselves, other ceramics or to metals. Common ceramic materials for inorganic membranes are: Porous alumina, transition metal oxide perovskites and zirconia. In this thesis, zirconia as the standard SOFC electrolyte material and alumina as

the most commonly used ceramic engineering material were utilized as the ceramic joining partners.

Alumina

Alumina ceramics (Al_2O_3) have high mechanical strength, excellent resistance to wear and corrosion, and also high electrical resistivity [LiJ02, Xia12, Kar08]. It is widely used in aviation, automotive industry and microelectronics as an electrically insulating substrate material [Ksi08, Tum89] in combination with metals.

Several techniques to produce Al_2O_3/metal joints were developed. Weil et. al studied the joint properties of polycrystalline alumina bonded with Ag-based brazes using reactive air brazing. The joints exhibited excellent mechanical and microstructural properties [Wei03, Kim08, Kim07a]. Thus the cost-effective reactive air brazing process is considered to have great potential in practical application for alumina/metal joining.

Zirconia

Although alumina is the most commonly used structural ceramic, zirconia is gaining momentum. Because of its high fracture toughness and strength zirconia (especially in case of transition strengthened zirconia) is an important structural material [Sci01]. Moreover, it is also one of the most useful electroceramics because of its good ionic conductivity at elevated temperatures [Han00]. Therefore, the application of zirconia ranges from wire drawing dies, cutting and machining tools, to oxygen sensors and fuel cells [Han00].

Zirconia exhibits three well-defined cystal structures: Monoclinic, tetragonal and cubic [Han00]. ZrO_2 adopts a monoclinic crystal structure at room temperature and transitions to tetragonal and cubic at higher temperatures [Lin1]. It is also known to be sensitive to changes in its stoichiometry, as the color of the material changes when it is reduced [Han00, Aga96]. When ziconia is blended with other oxides, the tetragonal and/or cubic phases are stabilized. Effective dopants include magnesium oxide (MgO), yttrium oxide (Y_2O_3), calcium oxide (CaO), and cerium(III) oxide (Ce_2O_3) [Eva86]. Stabilized zirconia is used in oxygen sensors and fuel cell membranes, because it offers high oxygen conductivity at elevated temperature [Nie00].

Various techniques were proposed to bond zirconia to metallic materials. Active metal brazing usually applies brazing alloys that contain titanium, which would chemically reduce the ceramic faying surface and greatly improve its wetting behavior and adherence [Sci01,

Han00, Aga96, Liu09]. Various reactive air brazing experiments have been conducted at zirconia that prove that in the presence of oxygen, the brazed interface adheres well even without reactively modifying the ceramic surface [Wei03, Kuh08, Li12a, Li12b].

2.4.2 Steels

For high temperature application, high resistance to oxidation is a major requirement for metallic materials [Kuh11]. Therefore, alumina-forming alloys, silica-forming alloys as well as chromia-forming alloys are preferred for SOFC application [Hil03].

Ferritic steels - Crofer® 22 H and Crofer® 22 APU

There are three main criteria for the interconnect materials in SOFC application: High electrical conductivity, good stability in both, reducing and oxidizing atmospheres at SOFC operating temperature and a coefficient of thermal expansion, that closely matches other SOFC components [LiY09]. Most of the studies on qualification and/or development of metallic high temperature materials for interconnect application relate to chromia-forming alloys, because of the electrical conductivity of Cr_2O_3 [Hil03]. Ebrite, Crofer® 22 APU, Haynes 230 and Haynes 242 are some Cr_2O_3-forming alloys for metallic interconnect application [Liu08]. To correspond to the thermal expansion coefficient (TEC) of the electroactive ceramic components (Zirconia-based electrolyte), ferritic steels are preferred because of their comparatively low TEC in comparison to other metallic candidate materials [Kuh11, Hil03].

Crofer® 22 H and Crofer® 22 APU are 22 % Cr ferritic steels, which were designed for solid oxide fuel cell interconnect and housing application at the Institute of Energy and Climate Research (IEK-2) of Forschungszentrum Juelich GmbH, Germany. Crofer® 22 H is an advanced version of Crofer® 22 APU employing additions of Nb and W for strengthening by fine Laves phase precipitates dispersed in the ferritic matrix [Kuh11]. The chemical composition of the two steels is listed in Tab.2 [Lin2].

Tab. 2.2 Chemical compositions of Crofer® 22 H and Crofer® 22 APU

Wt.-%	**Crofer® 22 APU**	**Crofer® 22 H**
Fe	Balance	Balance
Cr	20 % - 24 %	22 % - 24 %
C	0 - 0.03 %	0 - 0.03 %
N	0 - 0.03 %	0 -0.03%
S	0 - 0.02 %	0 -0.006%
P	0 - 0.05 %	0 -0.05%
Mn	0.3 % - 0.8 %	0.3 % -0.8 %
Si	0 - 0.5 %	0.1 % - 0.6 %
Al	0 - 0.5 %	0 - 0.1 %
W	0	1 % - 3 %
Nb	0	0.2 % - 1 %
Ti	0.03 % - 0.2 %	0.02 % - 0.2 %

Beside mechanical properties, the oxidation behavior of the interconnector material is of great importance. For Crofer® 22 APU, it is reported that iron doped chromia $(Cr,Fe)_2O_3$, Fe_3O_4 and Mn–Cr compounds form in the oxide scales in coal syngas and air at 800 ℃ after 500 hours [LiY09]. Under reducing atmosphere (wet or moisturized hydrogen), no iron or only little iron was detected in the oxide scales formed in low oxygen partial pressure environment. Instead of that, Cr_2O_3, Mn_2CrO_4 and MnO were detected [Liu08].

It is reported that with Nb addition to Crofer® 22 APU, the growth rate of the oxide layer would be enhanced [Fro08b]. Nevertheless, this undesired effect can be alleviated by suitable Si addition [Fro08b]. Therefore, with the combined addition of Nb, W and Si, Crofer® 22 H shows substantially higher creep strength than Crofer® 22 APU, without deteriorating the oxidation resistance and the electrical conductivity of the oxide scale [Fro08b].

The isothermal oxidation kinetics of Crofer® 22 APU obeys a parabolic law [Liu08], which suggests that the growth of the oxide scale is controlled by diffusion [Hor08]. This means that cation diffusion from the alloy and oxygen diffusion (from the atmosphere) through the oxide scale are rate governing. Recent research shows, that Laves phase precipitation retards the oxide scale formation of 20 % Cr ferritic steels (chemical composition of the steels are in shown in Tab. 1 in Appendix) during air annealing at 800 ℃ for 200 hours [Ide07]. Horita et. al compared the oxidation behavior of two ferritic steels for SOFC interconnect application in reducing atmosphere (H_2-H_2O). One was a Laves phase forming Fe-Cr alloy (Appendix, Tab.2) and the other was the commercial stainless steel SUS 430. It is reported that Laves phase formation at the alloy grain boundaries can effectively control the cation diffusivity, thus reducing the growth rate of the oxide scale [Hor08].

Austenitic steel - 1.4841 (AISI 314 / 314L)

Because of their high Cr and Ni contents austenitic steels are the most corrosion resistant stainless steels providing excellent mechanical properties [Lin5] and are widely used in high temperature application. Nevertheless, these grades present rather high thermal expansion coefficients (e.g. $\alpha_{1.4841}=18 \times 10^{-6} K^{-1}$[Lin3]) in comparison to the SOFC components, which would introduce high thermal mismatch stresses and might lead to low joint strength and possibly premature failure. Nevertheless the principal applicability of reactive air brazing for joining austenitic steel (1.4841) to YSZ is studied. The chemical composition of 1.4841 is given in Tab. 3 [Lin6]:

Tab. 2.3 Chemical composition of 1.4841 (AISI 314 / 314L)

Wt. -%	**1.4841**
C	0.2 %
Si	1.5-2.5 %
Mn	2 %
P	0.045 %
S	0.03%
Cr	24 -26 %
Ni	19 -22 %

2.5 Thermomechanical properties of Ag-based braze systems

With increasing effort in the development of intermediate temperature SOFC systems, Ag and Ag-based materials for sealing and interconnection have gained increased interest [Wei05c]. As a precious metal, Ag possesses good chemical stability, high electrical conductivity and lower costs than other precious metals like platinum and gold.

2.5.1 The Ag-O system

Phase diagram

Fig. 2.4 shows the phase diagram of the Ag-O system [Kar92]. Allen measured the melting temperature of silver as a function of p_{O_2}. His results show, that the liquidus temperature decreases from 961 ℃ in an oxygen-free atmosphere to 951 ℃ in air and to 928 ℃ in 0.99 bar O_2 (9.9×10^4 Pa) [All43].

Oxygen dissolves in silver by dissociation and formation of an α-phase solid solution in which both elements exist as atoms [Dus62]. The Goldschmidt atomic radius of the Ag-atom

is 1.44 Å, while that of the O-atom is 0.6 Å. Silver crystallizes in an fcc lattice with a lattice parameter of 4.08 Å [Smi62]. According to these dimensions, oxygen can occupy the octahedral interstitial sites, tetrahedral interstitial sites as well as Ag-atom vacancies in the lattice [Bai99]. Oxygen solubility in liquid Ag differs greatly from that in solid Ag: 1 at.-% of oxygen can be dissolved in liquid Ag, compared to only 0.05 at.-% in the solid [Ass97, Kar92]. This difference in oxygen solubility was reported to lead to pore formation during solidification of Ag [Kna68].

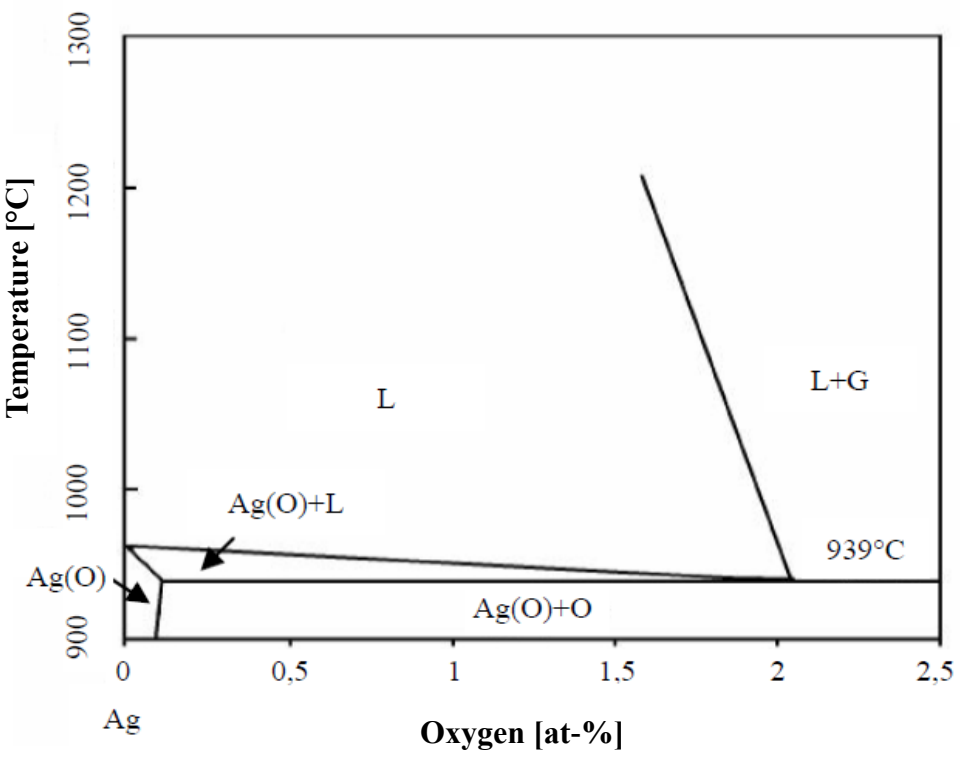


Fig. 2.4 Phase diagram of the Ag-O system [Kar92]

The effect of oxygen on wettability and thermodynamic adhesion in metal/oxide systems

It was reported by many authors [Eus99, Cha88], that pure liquid metals do not wet solid oxides in the absence of specific reactions. By adding elements which play an "active" role to the non-wetting metal or alloy at the solid-liquid interface, the interfacial specific free energy can be lowered, thus promoting wettability [Muo08]. Among all possible additives, oxygen - which is often considered as a "contaminant" - is very important in determining the surface properties and the technological characteristics of melts.

For the characterization of wettability, there are two main parameters: The macroscopic contact angle Θ and the work of adhesion (the work per unit area, which has to be provided to

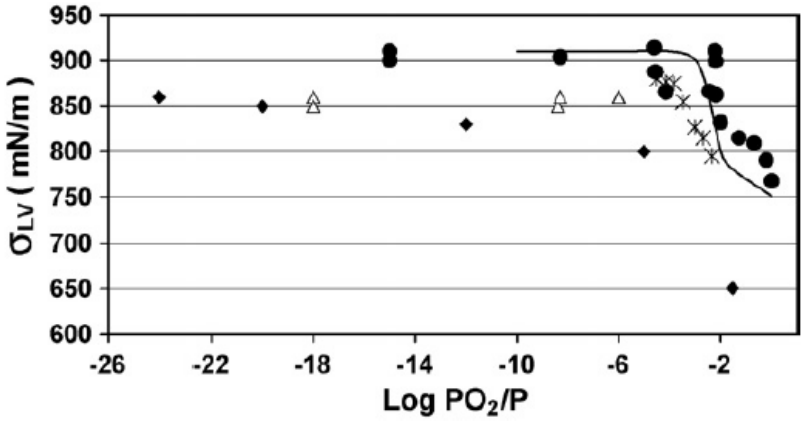
a system in order to create a reversible solid-vapor interface). According to the Young-Dupre equation (Equation 2.1), these two parameters are defined by the following equations [Cha94]:

$$\cos\theta = \frac{\sigma_{SV}-\sigma_{SL}}{\sigma_{LV}} \qquad (2.1)$$

$$W = \sigma_{LV} + \sigma_{SV} - \sigma_{SL} \qquad (2.2)$$

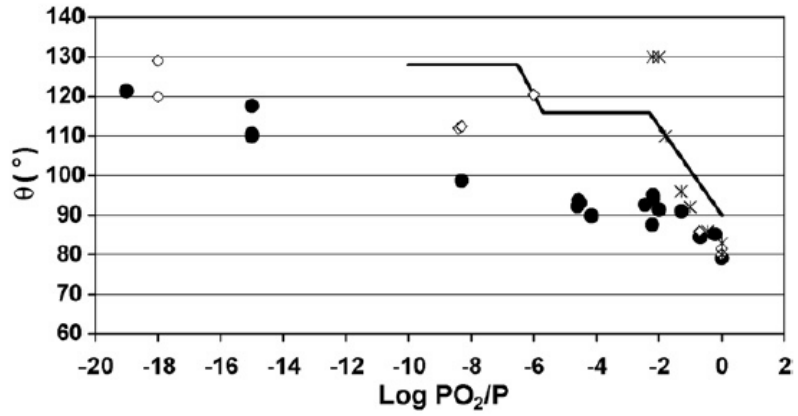
$\sigma_{LV,}$ σ_{SL} and σ_{SV} refer to the liquid-vapor, solid-liquid and solid-vapor interfacial tensions. It was reported by many authors, that surface tension of the liquid metal is reduced by increasing oxygen partial pressure in the atmosphere [Ber89, Eus01, Kar99, San82], thus promoting wetting. Muolo et. al compared all the relevant experimental data of wettability change (contact angle and work of adhesion) under different oxygen partial pressures within one diagram (Fig. 2.5) for the $Ag/O/Al_2O_3$ system [Muo08]. With increasing oxygen partial pressure the contact angle of liquid Ag on alumina clearly decreases, while the work of adhesion increases drastically. It is also concluded, that the beginning of the decrease in contact angle results from the decrease in σ_{SL} caused by the adsorption of oxygen-metal clusters at the metal/oxide interface. A further, but slight increase in p_{O2} (by one to two orders of magnitude) will cause a decrease in σ_{LV}, that in turn will affect wetting [Eus01].

(a)



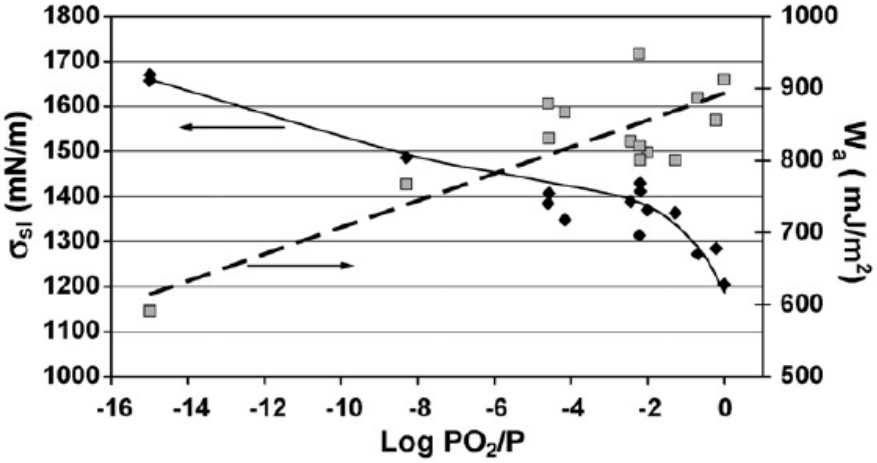
a) Variation of liquid-vapour interfacial tension σ_{LV} as a function of oxygen content in the gas phase: (●) Muolo et al., 1373K [Muo08]; (▬) Chatain et al. 1253K [Cha94]; (Δ) Chatain et al., 1373K [Cha93]; (×) Bernard et al. 1371K [Ber71]; (♦) Sangiorgi et al., 1372K [San82]

(b)



b) Variation of contact angle θ as a function of oxygen content in the gas phase: (●) Muolo et al., 1373K [Muo08]; (▬) Chatain et al. 1253K [Cha94]; (Δ) Chatain et al., 1373 [Cha93]; (×) Gallois, 1383K [Gal80].

(c)



c) Variation of solid-liquid interfacial tension σ_{SL} (continous line) and W_a (dashed line) as a function of oxygen content in the gas phase, T= 1373K. The solid-vapour surface tension has been considered constant and equal to 1350 mN/m.

Fig. 2.5 Variation of contact angle, surface tension and work of adhesion in the Ag/O/Al_2O_3 system as a function of the oxygen content in the surrounding atmosphere:

Like discussed previously, the work of adhesion increases with increasing oxygen partial pressure, what indicates an increase in interfacial energy. Serier et al. [Ser11a, Ser11b] compared the mechanical strength of Al_2O_3 solid state bonded by Ag foils of different oxygen concentrations. Joints bonded by silver with low oxygen concentration in oxygen show lower joint strength than the ones bonded by oxygen saturated silver. Kim et al. [Kim08b] studied the fracture strength and morphology of Ag and AgCu air-brazed Al_2O_3 joints after heat

treatment in hydrogen or air. It is found that heat treatment in hydrogen reduces the joint strength, while reoxidizing the joints regains the strength, what furthermore proves that the concentration of oxygen in the silver matrix is critical to the bond strength between silver and alumina. It was reported by Jarrige et al. [Jar07], that oxygen dissolved in liquid copper, improves wetting as well as the mechanical strength of AlN-copper joints. All these findings indicate, that the presence of O_2 in the braze matrix leads to stronger joints. Considering the high adhesion energy it seems to be reasonable to believe, that strong intra-molecular chemical bonds exist at the braze/ceramic interface, especially when taking the adhesion achieved by Van der Waals bonds into account.

Many assumptions were made by different researchers to explain the oxygen influence on the wettability and interfacial adhesion strength. Muolo et al. proposed the formation of a nearly complete interfacial oxygen monolayer, where the stacking of the atoms is simulated and shown in Fig. 2.6 [Muo08]. According to this theory, the bonding force between O (dissolved in Ag) and the metallic ions (in the ceramic) provides the strong interfacial adhesion between Ag and ceramic. However, many other researchers proposed other theories [Kim08b, Ser11a, Kar99, Cha94], in which the formation of Ag-O clusters at the interface is believed to be the governing mechanism. Naidich's model of oxygen-metal clusters explains this assumption (Fig. 2.7): Oxygen dissolved in the metal melt creates Me^{2+}-O^{2-} clusters with the metal atoms in its vicinity. These clusters adsorb at the metal-oxide interface, because of the electrostatic attraction between Me^{2+} cations of the cluster and O^{2-} anions emerging from the oxide surface [Nai81].

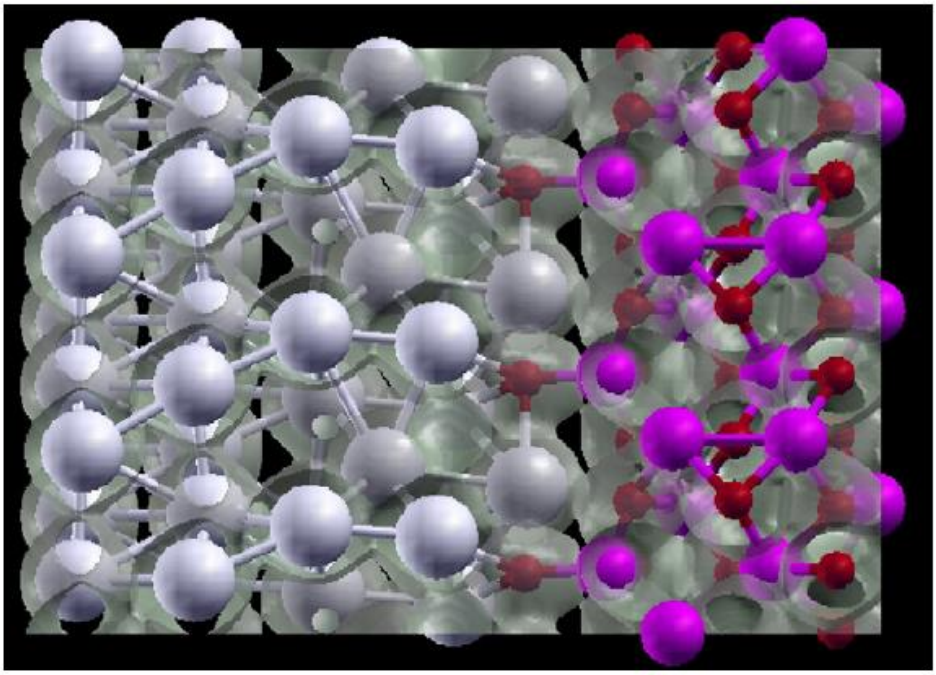


Fig. 2.6 Stacking of atoms at the Ag/Al_2O_3 (0001) interface, simulated by DFT (density functional theory) calculations: Four silver (grey atoms) layers on the left hand side, an oxygen (smaller-red) atom "layer" at the interface and alumina terminated with Al (Purple) [Muo08]

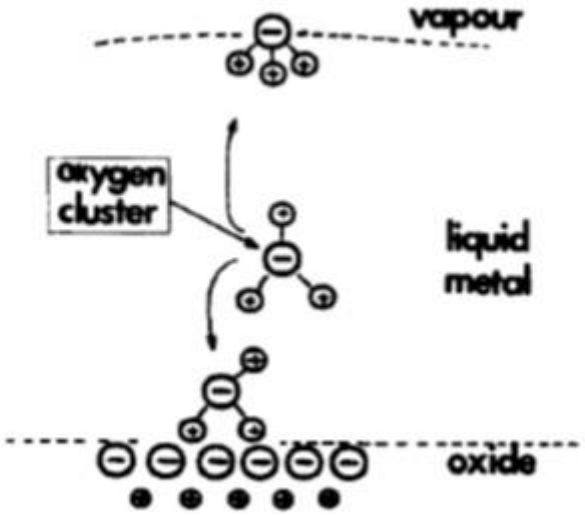


Fig. 2.7 Adsorption of oxygen-metal clusters at the metal-vapour and metal-oxide interface according to the model of Naidich [Nai81]

Pure Ag in air brazing

The wettability and adhesion strength of Ag on ceramics obviously increases with increasing oxygen partial pressure. Considering costs and ease of processing (discussed in chapter 2.3), air brazing would be a good choice for industrial application. In air, the oxygen partial pressure is about 0.2, which in turn means that - according to Muolo (Fig. 2.5) - pure Ag will show a contact angle larger than 90 ℃ and thus poor wetting for industrial applications. Moreover, like discussed previously, the differences in oxygen solubility in solid and liquid Ag would cause pore formation in the braze matrix during solidification in air. Therefore, alloying of the pure Ag is mandatory. Wettability improvement by alloying was already recognized [Cha88] in the past. Fig. 2.8 shows the wetting results of three different brazes on alumina [Li12b]. Obviously, the wetting behavior of Ag on alumina can be greatly improved with the addition of Cu and Al. Al addition not only improved the wettability, but also enhanced the contour accuracy and reduced spilling of the braze material [Li12b]. Fig. 2.9 impressively demonstrates the enhanced wetting and reduced spilling properties of Al-containing brazes even under quasi real-life geometrical conditions for SOFC application [Li12b]. The reasons for the increased wettability by alloying might be the following: Increased viscosity because of precipitate formation within the melt [Bob11], altered surface tension of the Ag melt [Bob10] and the formation of an interfacial compound, for example $CuAlO_2$, in alumina joints [Kim05].

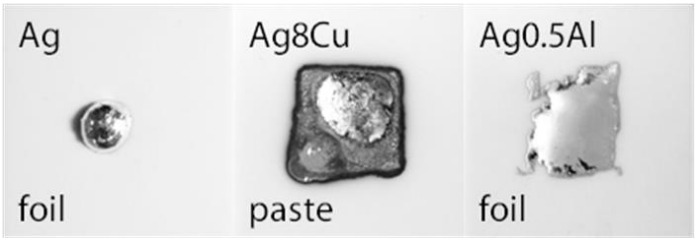


Fig. 2.8 Wetting behavior of three RAB-brazes on Al_2O_3 [Li12b]

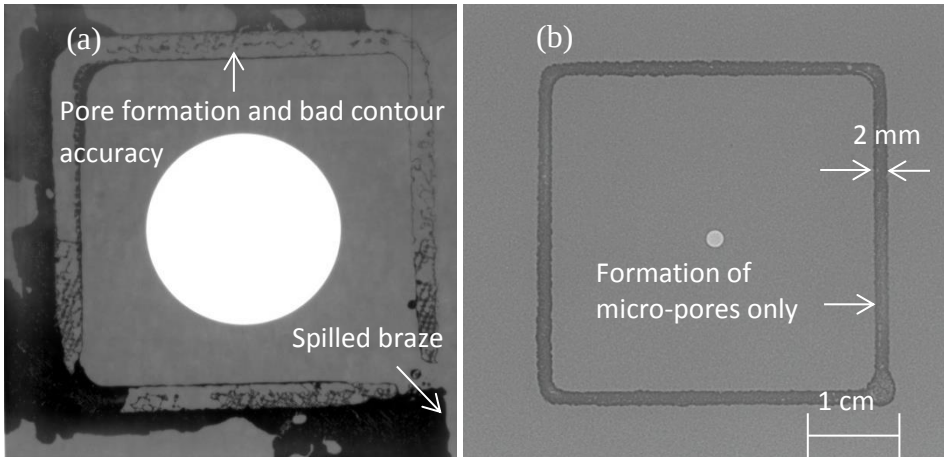


Fig. 2.9 X-ray radiographic views of hermeticity testing samples (SOFC half cells brazed to deep-drawn Crofer® 22 APU sheets) utilizing the following braze systems: a) pure Ag, b) improved Al-added braze [Li12b]

2.5.2 The Ag-Cu system

Ag-Cu braze systems are nowadays studied as candidate braze materials for reactive air brazing, because of their good wetting behavior in air. Recent research shows, that the wettability of AgCu(O) brazes on different ceramics increases with increasing Cu content [Kim05, Wei03]. The rupture strength of AgCu(O) brazes depends on compositional changes and the joining partners. It is reported that the strength of AgCu(O) brazed alumina joints reaches a maximum, when the braze contains 8 mol-% of copper oxide, but decreases dramatically at higher copper oxide content [Kim05]. The same applies for 5YSZ/AgCu(O)/FeCrAlY joints, with the maximum rupture strength ranging from 4-8 mol-% Cu(O) in Ag [Wei03, Wei05b]. Opposing effects of reaction layer formation and effectively brazed surface area on the interfacial strength are a possible explanation for this phenomenon. Increased wettability because of increasing Cu content means better contour accuracy of the joint, what subsequently leads to increased joint strength. On the other hand, the interfacial brittle reaction layer increases with increasing Cu content, what in turn has a deleterious effect on joint strength. Therefore, an increase in rupture strength would be obtained only if the wetting effect overrules the deteriorating effect.

Fig. 2.10 shows the phase diagram of the Ag-Cu-O system [Ass98]. For a AgCu(O) braze, the melting temperature constantly decreases to 941 ℃ with increasing Cu(O) content up to about 1.4 mol-%. With further addition of Cu(O), the melting temperature again rises to

969 ℃. For industrial application the brazing temperature should therefore be chosen higher than 969 ℃, to ensure thorough melting of the braze.

Besides enhanced wettability compared to pure Ag joints, gas filled pores can still be found in specimens brazed with AgCu(O) brazes [Rei08]. Although Cu has high affinity to O_2, and thus absorbs oxygen released from the Ag matrix during solidification, the decomposition of CuO to Cu_2O may in the other way release oxygen, causing additional pore formation, if the brazing temperature is chosen too high. Under atmospheric pressure CuO decomposes at a temperature of 1026 ℃ [67]. However, local circumstances may be able to favour premature decomposition of CuO during the brazing process [Rei08]. AgCu(O) braze joints were reported to be very sensitive to the exposure to reducing atmosphere at high temperature [Wei05a, Kuh08]. Exposure to hydrogen reduces the internal CuO precipitates in the filler metal and the copper mixed oxide reaction layers at the steel/braze interface to metallic copper with subsequent alloying into the Ag matrix. This reduction of copper mixed oxide reaction layers at the steel interface was reported to lead to a decrease of joint strength [Wei05a, Kuh08].

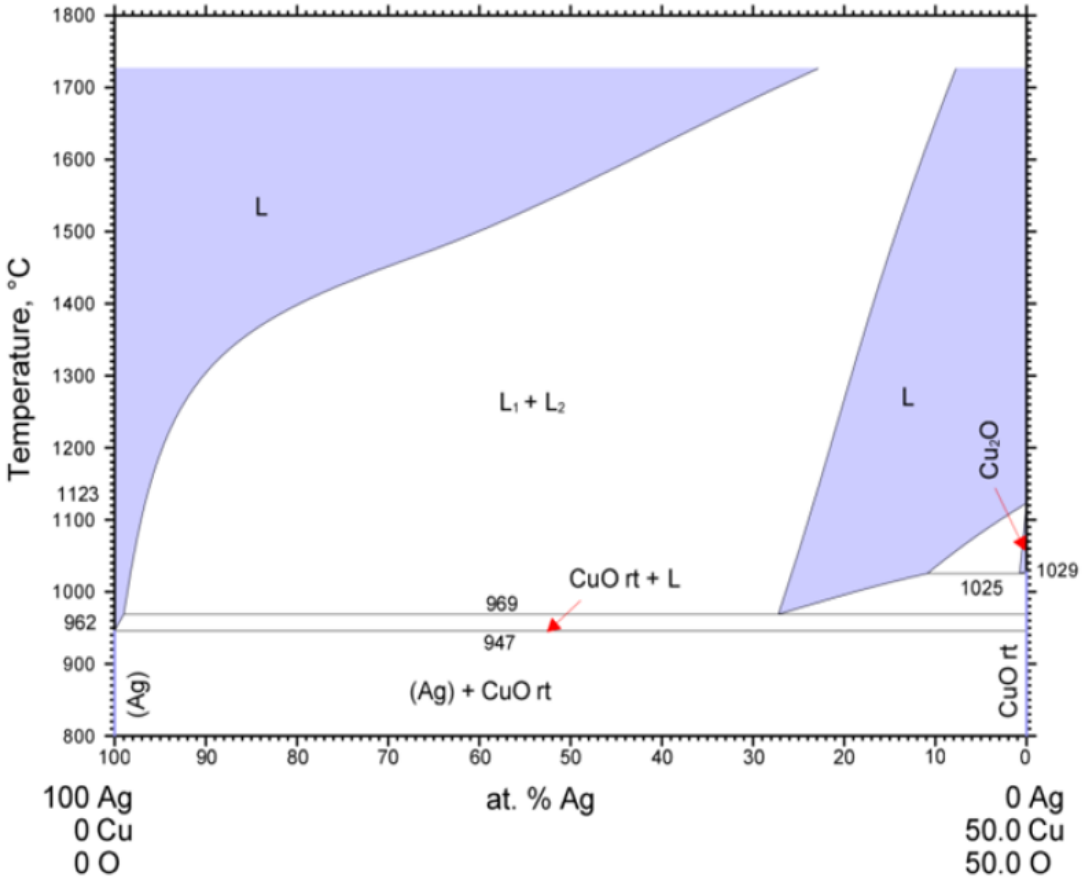


Fig. 2.10 Phase diagram of the Ag-Cu system [Ass98]

2.5.3 The Ag-Al system

Fig. 2.11 [Din91] shows the phase diagram of the AgAl system. With the addition of Al, the melting temperature of the alloy decreases constantly. According to the phase diagram it is obvious, that in order to maintain the thermomechanical properties of the brazed joints, the Al content has to be controlled within a certain range, carefully considering the desired working temperature range.

As discussed in chapter 2.5.1, the wettability and contour accuracy is greatly improved by adding Al to the Ag brazes, which results in easy and accurate processing for industrial application. Meanwhile, unlike Cu, Al has a higher affinity to oxygen than hydrogen. This property poses the great potential of AgAl brazes in O_2/H_2-containing dual atmosphere operation.

Kim et al. examined the mechanical properties and dual atmosphere tolerance of Ag-Al brazed alumina joints [Kim08]. It was found that the bending strength of the joints decreased

with increasing aluminum content. On the other hand, it was also found that metallic aluminum can be detected within the filler metal in case of Ag-Al braze foils containing more than 2 at.-% Al, which enhanced the high temperature dual atmosphere tolerance of the resulting joint [Kim08].

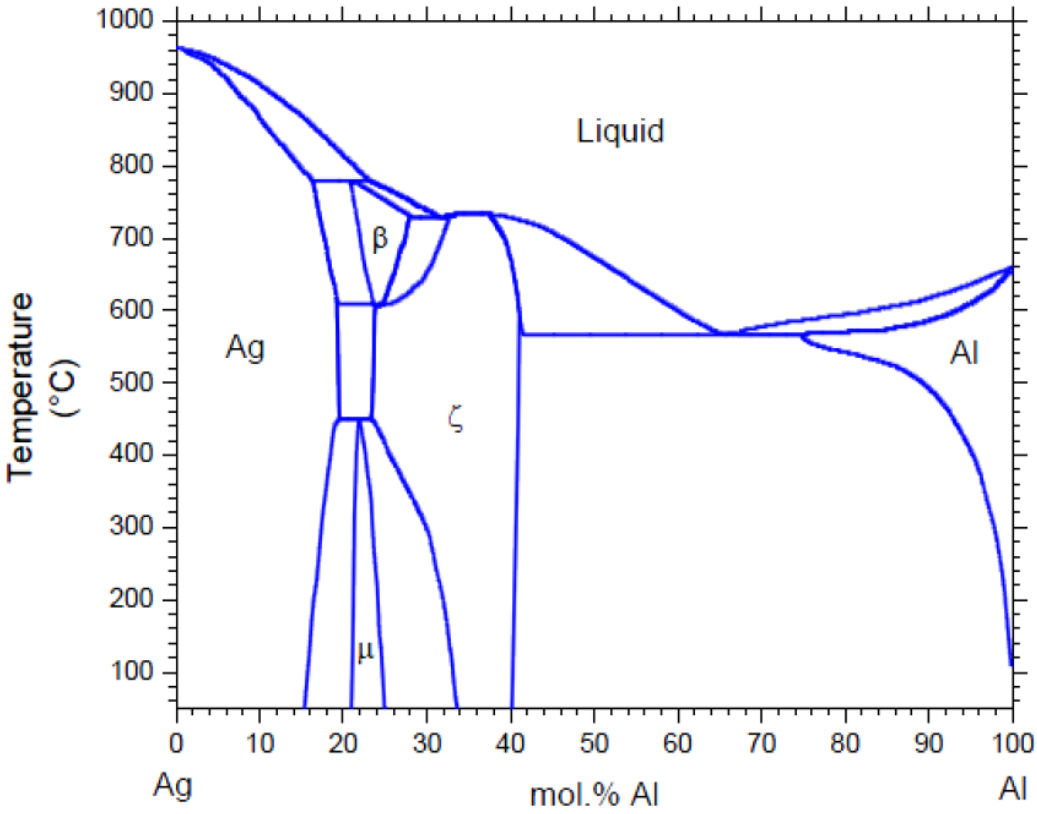


Fig. 2.11 Phase diagram of the Ag-Al system [Din91]

2.6 Mechanical behavior of the braze matrix

2.6.1 High temperature creep

When a stress – even below the yield strength - is applied to a metal or alloy at high temperature, the material may continue to deform in a time-dependent manner and finally fail. This phenomenon, known as creep, can virtually occur at all temperatures above absolute zero, but becomes more significant with increasing temperature [Eva85]. Generally, short term creep tests up to about 100 hours of duration are usually undertaken for material quality assurance, while long term tests are conducted to obtain design data [Eva85]. Typical creep curves of logarithmic creep and normal creep are shown in Fig. 2.12. In the low temperature

regime ($\leq 0.4 \times T_m$, T_m denotes the melting temperature [K] of the material) logarithmic creep takes place, in which the creep rate decreases continuously with time and the deformation processes usually do not lead to fracture. At temperatures towards $0.4 \times T_m$ a so called "primary stage", in which the creep rate decreases continuously, follows the instantaneous strain ε_0. Eventually the creep rate would become constant, which is caused by a dynamic balance of thermally activated dislocation motion, e.g: climbing, recovery and work hardening. This period is defined as the "secondary creep stage". Nevertheless, lots of materials do not show extended secondary stages with constant creep rate, but display only a short period of minimum creep rate. In the "tertiary stage" the creep rate increases till fracture occurs [Eva85].

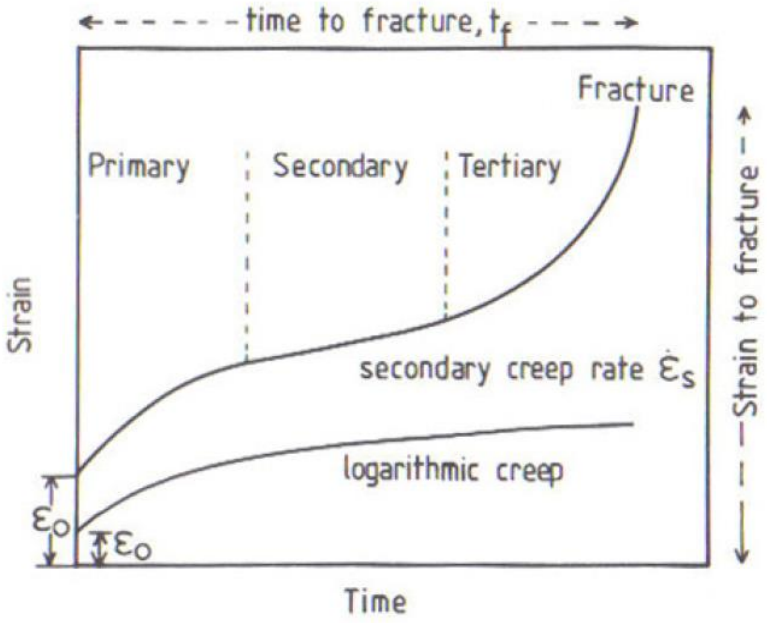


Fig. 2.12 Typical curves of logarithmic creep and normal creep [Eva85]

Creep is known to depend on the applied stress, deformation temperature and microstructure of the tested material [Klc05]. Grain size, precipitate formation and solid solution of alloying elements can strongly affect creep [Hon89, Faw09]. The dominating mechanisms of creep differ in different temperature/stress regimes. For engineering purposes deformation mechanism maps were developed, which summarize the deformation characteristics of a material as a function of stress and temperature. The deformation mechanism map of pure Ag is displayed in Fig. 2.13.

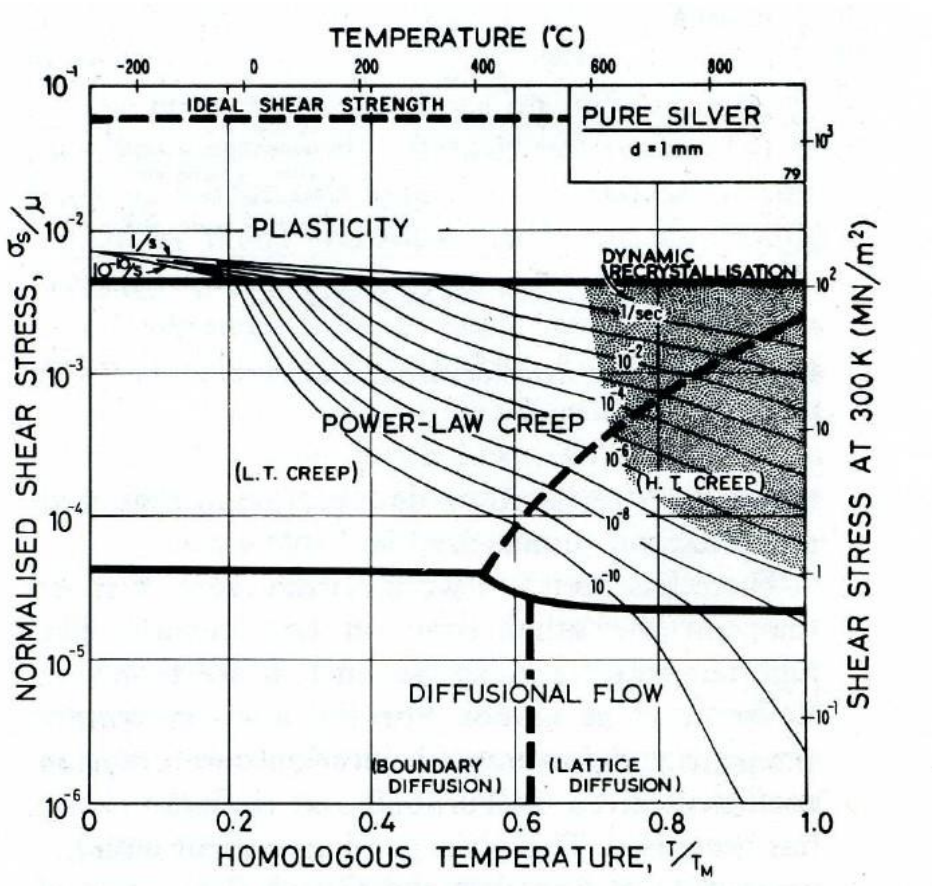


Fig. 2.13 Deformation mechanism map of pure Ag [Fro82]

It has been reported that the creep properties of Ag are strongly affected by the annealing and testing atmosphere as well as the impurity content of the tested material [Pri66]. With respect to atmospheric issues Price et al. found, that oxygen inhibits grain boundary slide and migration during creep and increases the number and growth rate of voids [Pri66]. Goretta et al. [Gor96] and Price et al. [Pri66] reported, that Ag of high impurity content (99.99 % Ag) is stronger in high temperature deformation than high purity Ag (99.999%). Strengthening by oxidation of impurities is reported to amplify the atmosphere dependence at the expense of ductility [Pri66, Gor96b].

2.6.2 Stress relaxation

Conventional constant load creep tests require a lot of specimens to determine the creep rates at different stress levels and the testing durations are usually very long (from days up to several years). Stress relaxation testing (SRT) can be a “short cut”-approach for determining minimum creep rates at various stress levels in a single experiment. For life assessment of operating components, creep strength and fracture resistance are two important values. Since

an enormous amount of data can be generated in short time by SRT, creep strength may be evaluated based on high precision short time stress relaxation tests [Woo97]. However, there are certain limitations of SRT [Sin03, Yam90]:

1. Life assessment is not possible because SRT can not account for long-term microstructural changes
2. SRT only works with good "extrapolation" accuracy, if secondary creep (i.e. the minimum creep rate constant during sufficient time and the secondary creep stage is the dominating stage throughout the whole creep lifetime) is the life-determining stage

Nevertheless, despite of these limitations, SRT is a good tool for material development.

Although stress relaxation and creep are technically different, the net effect is the same, because both loading types lead to the eventual exhaustion of a component's ductility. Differences between the creep rates measured in conventional creep testing and the plastic strain rates measured during stress relaxation tests can be caused by recovery during the relaxation phase and the precision of the Young's modulus measurement, which is essential for data evaluation from SRT [Yam90].

Stress relaxation tests are performed by applying a given total strain ε_t to a specimen and maintaining it constant, while the stress σ drops with time. The principle of this testing method is the conversion of the elastic strain ε_e in the specimen to the inelastic strain ε_p: Since the total strain $\varepsilon_t = \varepsilon_e + \varepsilon_p$ is constant after the beginning of the stress relaxation, $d\varepsilon_t/dt = 0$ and for this reason $d\varepsilon_p/dt$ is given by:

$$d\varepsilon_p/dt = -d\varepsilon_e/dt = -d(\sigma/E)/dt$$

Where E is the Young's modulus and σ is the stress at time t [Yam90].

2.6.3 Thermal fatigue

Thermally induced stresses due to constrained expansion and contraction occur in most high-temperature structures [Cla69] and can be caused either by inhomogeneous temperature distribution or uniform temperature change of a compound of several materials with different coefficients of thermal expansion. When failure occurs after a repeated number of temperature cycles, the failure mechanism is called thermal fatigue [Cla69].

Thermal fatigue damage and failure includes low temperature mechanical fatigue, as well as creep-rupture processes at high temperatures [Cla69]. At low temperatures, cyclic plastic deformation in tension and compression will ultimately exhaust the ductility of the material causing fatigue cracking, while holding at high temperature may lead to loss of strengthening (either by loss of strain-hardening or microstructural change), as well as recrystallization and recovery. On the contrary, secondary phases may precipitate along slip lines and cause hardening of the material [Cla69].

Several authors investigated thermally cycled lead-free solder joints (-15 ℃ ~ 150 ℃) and reported recrystallization/grain growth in the solder [Tel07, Ter04, Hen04]. Telang et. al compared different recrystallization and grain growth processes and identified maximum strain energy release as the driving force for the recrystallization of the soldered joints [Tel07].

2.6.4 Nucleation criteria for recrystallization

To successfully generate a recrystallization nucleus in a deformed microstructure, three instability criteria have to be met [Got04]:

1) Thermodynamic instability:
   As the driving force for recrystallization is very low, nucleation due to thermal fluctuation can not initiate recrystallization. Therefore, a pre-existing nucleus with a critical radius (e.g. dislocation cells or subgrains) has to be present in the deformed microstructure to start the recrystallization process.

2) Mechanical instability:
   A local imbalance of the driving forces is required to move the grain boundary of the nucleus into a defined direction, which can be realized by an inhomogeneous dislocation distribution or by a local imbalance of subgrain sizes.

3) Kinetic instability:
   A highly mobile grain boundary is needed for the growth of the nucleus. Usually only high angle grain boundaries have sufficiently high mobility.

Due to the three constraints stated above, nucleation of recrystallization usually starts at specific regions in a deformed microstructure, especially at deformation inhomogeneities

and at prior grain boundaries [Got04]. Besides that, secondary particles and twin formation can also promote nucleation of recrystallization processes [Got04].

3. Experimental

3.1 Materials

3.1.1 Braze

In this work, three different brazes for reactive air brazing were investigated, i.e. pure Ag, AgCu(O) and AgAl foils. The aim of this work is to study the basic principles and fundamentals of reactive air brazing. Therefore foils with less pore formation and more homogeneous distribution of the reactive elements compared to industrial braze pastes are preferred. The properties and production procedures of the three brazes are introduced below.

- **Pure Ag foil**

The pure Ag foils applied in this work were produced by Schlenk GmbH with a purity of 99.995 % and a thickness of 100 µm. As stated in chapter 2.5.1, the pure Ag braze exhibits poor wettability on the joining partners and is therefore not suitable for commercial application. Nevertheless, it is investigated in this work as a standard simplified braze system for comparative studies of Cu- and Al-addition. Without any reactions at the interfaces, it is easier to study the adhesion behavior of the Ag melt on the joining partners.

- **AgxCu(O) foils**

AgCu(O) foils were produced by galvanizing Cu on both surfaces of pure Ag foils. By controlling the thickness of the galvanized Cu(O) layer, the desired AgxCu(O) braze can be produced with x molar percent of Cu(O) within the Ag braze. In this work, Ag4%Cu(O) and Ag8%Cu(O) (mole-%) were produced and investigated.

- **Ag0.5Al foils**

In this work, two different production methods of AgAl foils were applied. One is the so-called Physical Vapor Deposition (PVD) method: 0.5 mol.-% of Al was PVD coated on the surface of the pure Ag foils (Ag0.5Al (PVD)). Ag0.5Al (IOT) braze foils were fabricated at the Institute of Surface Technology (IOT) of RWTH Aachen by arc melting of Ag and Al in

the desired ratio (0.5 mol-% Al). The casted block was then cold rolled to a final thickness of 100 µm and the resulting foils were finally soft annealed in high vacuum at 600 °C for 20 minutes at the Central Technology Division (ZEA-1) of Forschungszentrum Jülich.

3.1.2 Joining partners

- **Steel**

Crofer® 22 H ferritic steel was investigated in this work as the steel joining partner for SOFC interconnect application. Crofer® 22 H is an advanced version of the Crofer® 22 APU, which is specifically designed for SOFC application. Basic information of the two steels and their differences have been explained in chapter 2.4.2. Both steels have a thermal expansion coefficient of about 12 $\times 10^{-6}$ K^{-1} [Lin2], which corresponds well to that of the SOFC electrolytes TZ3Y and TZ8Y ($10.1 \times 10^{-6} K^{-1}$/$10.6 \times 10^{-6} K^{-1}$ [Bas11]).

Kuhn discovered [Kuh08], that the mechanical behavior of the joints differs when pre-oxidation was carried out at Crofer® 22 APU steel surfaces. As this thesis aims at investigating the underlying adhesion mechanism and interfacial reactions, joints brazed with bare steel and pre-oxidized Crofer® 22 H were both investigated and compared. For industrial application the brazing properties of pre-oxidized steel may also be of interest, because processing steps previous to brazing might induce pre-oxidation of the steel surface. Pre-oxidation was carried out at 800 °C for 100 hours to obtain a stable Cr/Mn-spinel duplex layer. These parameters were chosen with consideration of both, technical necessities and economic factors. On the one hand, the pre-oxidation process has to ensure an intact oxide layer of sufficient thickness. On the other hand, the costs for the process should also be taken into account. It is reported by Froitzheim et al. [Fro08] that the weight-gain of Crofer® 22 H after pre-oxidation (800 °C, 100 h) is about 0.05 mg/cm^2 on 2 mm sheet material. With the density of chromium oxide ($\rho_{Cr2O3} \approx 5.5$ g/cm^3 [Lin7]), the layer thickness after pre-oxidation is about 0.1 µm.

Besides, 1.4841 austenitic steel is also investigated in this thesis as another steel candidate. It has higher thermal expansion coefficient (18 $\times 10^{-6} K^{-1}$[Lin3]) compared to ferritic steels, which also means higher thermal mismatch to the ceramic joining partner. Nevertheless, as Ag-based brazes have a thermal expansion coefficient of about 20-22 $\times 10^{-6} K^{-1}$ [Kop06], the higher thermal expansion coefficient of 1.4841 austenitic steel means smaller thermal mismatch ($\Delta TEC_{Austenite\&Ag} \approx 5 \times 10^{-6} K^{-1}$ compared to $\Delta TEC_{Ferrite\&Ag} \approx 12 \times 10^{-6} K^{-1}$) against

the braze. Therefore, the brazing properties of this joining partner would also be very interesting for studying the applicability range of reactive air brazing.

- **Ceramic**

For ambient temperature four-point bending tests at model SOFC-joints, the cell part was identified previously as the weakest link in the brazed specimen with a fracture toughness of about 1-2 MPa$\sqrt{m}$ [Kuh08]. For this reason, phase transformation strengthened TZ3Y foils (zirconia with 3 mol % addition of Yttria [Bas11]) of higher fracture resistance (5-6 MPa$\sqrt{m}$ [Cla83, Sal07]) was employed as the ceramic joining partner material in order to avoid fracture of the ceramic. The surface roughness R_a of this material is in the range of 0.7-0.9 µm [Kuh08], which is comparable to the SOFC half-cells.

For high temperature double shear tests, symmetric electrolyte coated anode substrates (ESE: Electrolyte/Substrate/Electrolyte unit) were applied as the ceramic joining partner. The anode is composed of NiOx, with a thickness of about 1.5 mm. 8YSZ (zirconia doped with 8 mol % of Yttria) was coated on both sides of the anode surface as the electrolyte material. The surface roughness R_a of the half-cell is about 0.8-1.1 µm [Kuh08].

3.2 Brazing process

3.2.1 Temperature program

Brazing was conducted in air (p_{O_2} = 0.21 bar) in a KS-80S type furnace (Linn High Therm, Eschenfelden). The temperature program replicates real-life parameters of SOFC component manufacturing:

1. Heating to 300 °C by 5 K/min
2. Holding at 300 °C for 30 minutes for temperature homogenization
3. Heating from 300 °C to 500 °C by 5K/min
4. Holding at 500 °C for 30 minutes for oxidation of the Cu of the Cu-containing braze foils and for temperature homogenization
5. Heating from 500 °C to 1000 °C by 3K/min
6. Holding for 5 minutes
7. Furnace cooling

For all specimens, the temperature deviation was kept within ± 4 °C at brazing temperature (1000 °C).

3.2.2 Brazing tools

To braze multi-layered specimens for mechanical testing, a productive and reliable brazing tool is necessary. For four-point bending tests and double shear tests, specimens were brazed in specially designed brazing jigs shown in Fig. 3.1. Slots prevent the specimens from shifting or sliding during preparation and brazing. The top and bottom parts of the jigs were aligned by alumina pins at the jig corners to keep the displacement of the upper and lower specimen layers within a range of ± 0.3 mm. The top parts of the jigs are designed to put an average surface pressure of 50 g/cm^2 on the joints, to ensure a thickness of the braze comparable to that in prototype SOFC joints (60-80 μm).

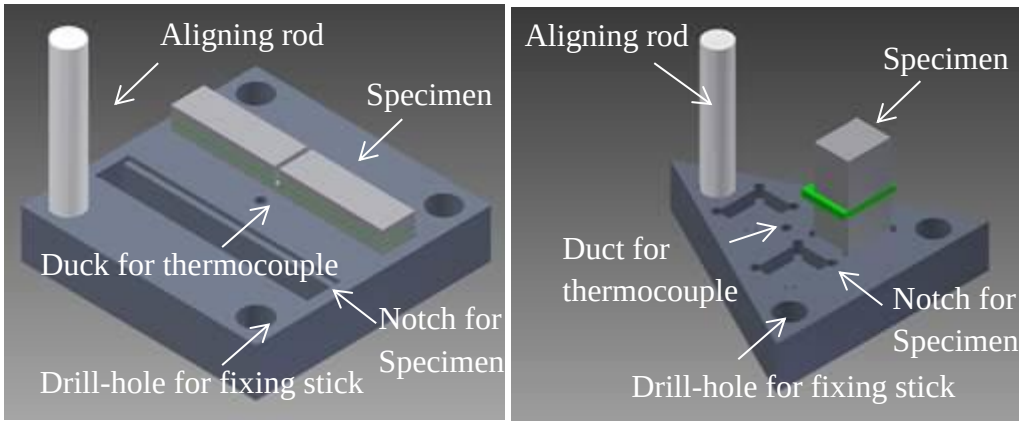


Fig. 3.1 Brazing jigs for ambient temperature delamination and high temperature double shear specimens

These brazing jigs were made from 1.4742 - X10CrAlSi18 (Thermax) steel, which contains about 17-19 wt.% of Cr. The oxidation resistance of the steel is enhanced by Si and Al addition through formation of an alumina layer on the steel surface. The thermal expansion coefficient of the brazing jigs is about $12.5 \times 10^{-6} K^{-1}$ [Lin4], which is comparable to the steel joining partner Crofer® 22APU/H.

3.3 Aging treatment

3.3.1 Isothermal annealing

Annealing in air at 800 ℃ was conducted in an M110-type furnace from Heraeus for 500, 1500 and 3000 hours.

Annealing in reducing atmosphere was conducted in an SR-type tube furnace produced by GERO Hochtemperaturöfen GmbH & Co.KG. During annealing, the alumina furnace tube was sealed at both ends and flushed with Ar4Vol%H_2 (flow rate of 4 l/h). The specimens were annealed at 800 ℃ for 1500 and 3000 hours.

After annealing, the specimens were mechanically tested by ambient temperature four-point bending and high temperature double shear tests to characterize the effect of isothermal aging in different atmospheres.

3.3.2 Thermal cycling

For automotive application, the SOFCs have to be frequently started up and shut down. During these periods, the stacks are subjected to rapid temperature changes. Because of the differing thermal expansion coefficients of the joining partners ($\alpha_{Crofer22H}$ = 12.5 × $10^{-6}K^{-1}$, α_{TZ3Y} = 10.1 × $10^{-6}K^{-1}$, α_{Ag} = 20-22 × $10^{-6}K^{-1}$[Lin2, Bas11, Kop06]) drastic temperature changes may be deleterious to the integrity of the joints. Thermal mismatch stresses are generated in all the joint components during operation, endanger the mechanical integrity of the brazed joints and may ultimately limit stack lifetime. Therefore, the ability of the joints to resist rapid thermal cycling is considered to be of highest priority.

To study the influence of fast heating and cooling processes, thermal cycling tests were conducted at all braze variants given in section 3.1. Fig. 3.2 shows the temperature of the specimens during cycling. The specimens were placed into a glass holder at the tip of a lance, equipped with a type K thermocouple for temperature measurement. The specimens were automatically introduced and redrawn into/from the furnace by the lance and heated/cooled up/down to 800 ℃/200 ℃. Once the temperature reached 800 ℃, the specimens were taken out of the furnace and cooled in ambient air down to about 200 ℃ and the cycle was repeated. In this work, the furnace temperature was set to 877 ℃. Starting from 200 ℃ the specimens reached 800 ℃ within about 6.5 minutes, which corresponds to a mean heating rate of about 100 K/min. Cooling from 800 ℃ to 200 ℃ took about 5 minutes. After the desired number of cycles, the mechanical strength of the specimens was examined by room temperature delamination tests.

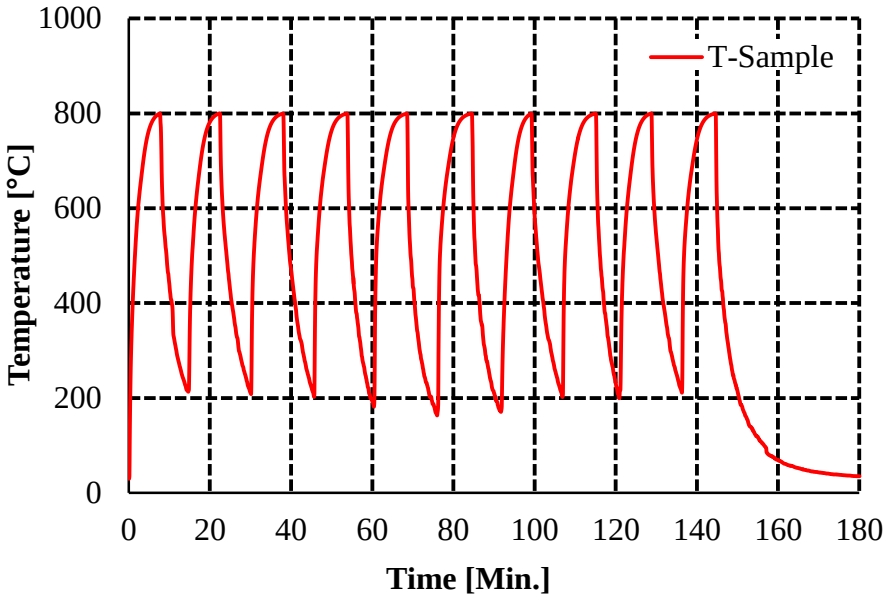


Fig. 3.2 Temperature of the specimens during thermal cycling [Kuh08]

3.4 Room temperature delamination testing

In SOFC technology, reactive air brazing is applied in two areas: First, the cell-to-manifold joint (Fig. 3.3a). And second, the manifold-to-manifold joint (Fig. 3.3b). This thesis concentrates on the properties of cell-to-manifold joints.

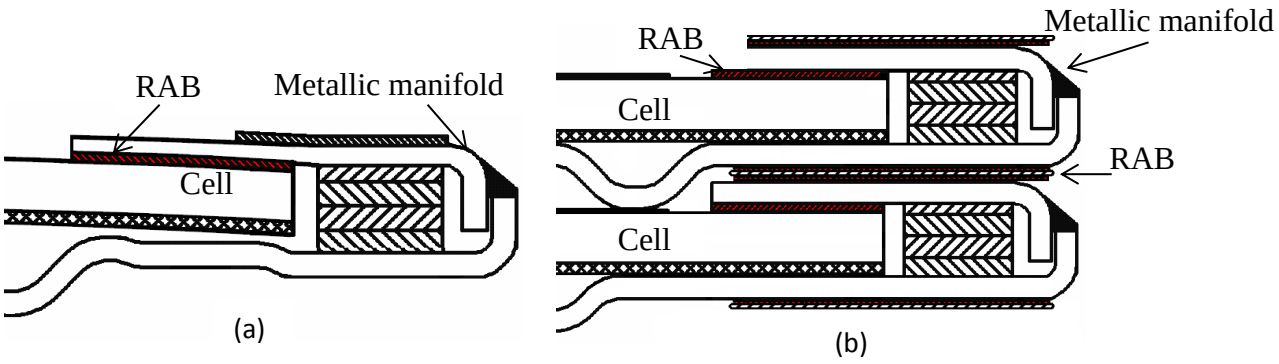


Fig. 3.3 Schematic cross-sectional view of the: a) manifold-to-manifold joint; b) cell-to-manifold joint in an SOFC-stack [Kuh08]

During operation of SOFCs, the anode of the cell is oxidized/reduced, which in turn changes the curvature of the entire cell, like it is depicted in Fig. 3.3. This change of curvature causes a bending moment in the joint, which may cause damage. Therefore, a close-to-reality testing method should imitate bending of the multi-layered joining system. In this work, room temperature delamination tests according to Charalambides [Cha89, Cha90] are applied to characterize the fracture resistance of the multi-layered system under bending load.

3.4.1 Sample geometry

To achieve testing results viable for practical application, the assembled specimens should stay as close as possible to the real SOFC stack-like layer arrangement. Fig. 3.4 shows the real stack design layout and the derived sample geometry. The specimens were assembled in sandwich-like geometry with five layers in total. Compared to the three-layer arrangement in a real stack, additional stiffening elements made of steel are applied in the specimens to prevent vertical cracking of the ceramic foils [Kuh09]. In the stack, the tips of the brazed joints are typically crack initiation sites because of the maximum bending moment and the stress concentration occurring at this position. Therefore, to imitate this condition, the specimens are assembled symmetrically with a notch (1 mm) in the middle of the specimen.

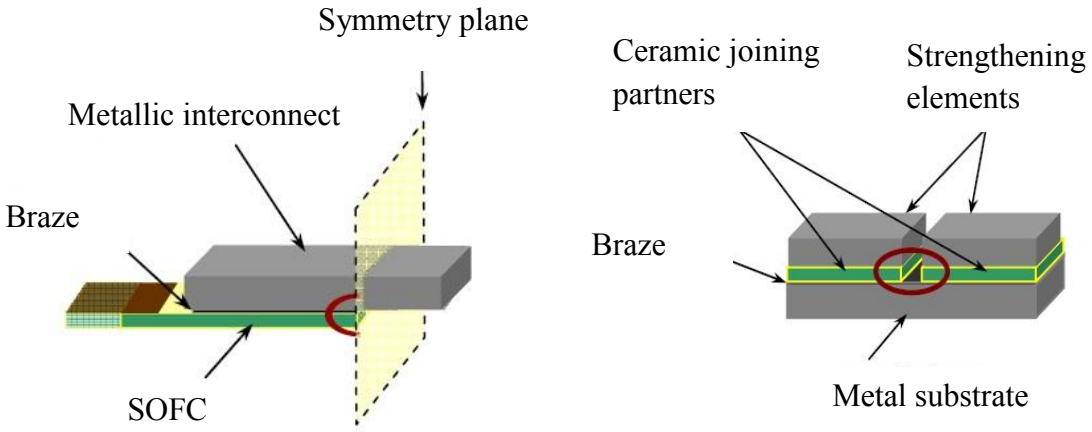


Fig. 3.4 From stack design to sample geometry [Kuh08]

The sample dimensions are shown in Tab. 3.1 according to Kuhn [Kuh08].

Tab. 3.1 Dimensions of the four-point bending specimens

Sample width b	**7 mm**
Thickness of the metal substrate h_2	2.5 mm
Length of the metal substrate	45 mm
Thickness of the TZ3Y foils h_d	0.1 mm
Thickness of stiffening elements $h_{d'}$	2.5 mm
Length of the stiffening elements	22 mm
Thickness of the braze foils	0.1 mm

3.4.2 Execution of tests

The ambient temperature delamination tests were performed using a TesT 113.5 kN electromechanical testing machine with ceramic four-point bending fixtures (40 mm /20 mm span ratio as shown in Fig. 3.5), applying a constant deflection rate of 0.33 μm/s.

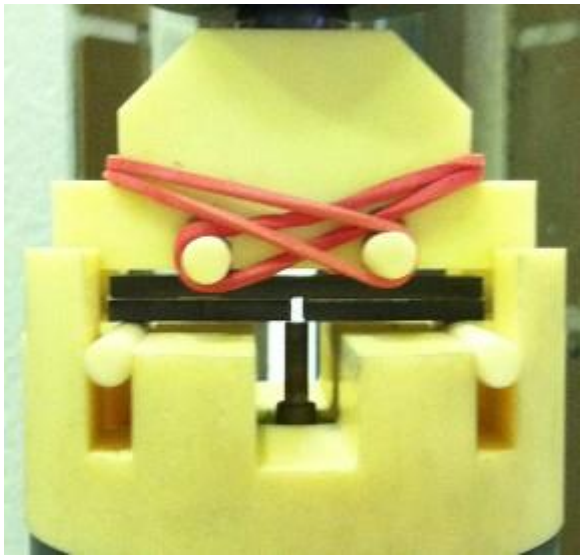


Fig. 3.5 Test setup for ambient temperature delamination test

The energy that is needed for interface delamination is normally denoted as fracture energy G_{ss} [Lan03]. During bending of the previously discussed sandwich-like specimens, elastic energy is stored in the multi-layer system during loading. When the stored elastic energy exceeds the fracture resistance of the multi-layered specimens, cracks initiate and release the stored elastic energy. Cracks normally (but not necessarily) initiate at the notch tip and propagate along the weakest path of the multi-layer specimens.

Fig. 3.6 shows a typical load-deflection curve of an ambient temperature delamination test. During testing, the load increases linearly with increasing deflection at the beginning, in which elastic energy builds up within the specimen. Cracks initiate when the load reaches F_{Peak}, where a sudden drop of the force to F_{Dip} occurs. This force drop releases part of the stored elastic energy till the driving force for cracking equals the fracture resistance of the specimen.

These two values (F_{Peak}, F_{Dip}) differ with respect to different brazes. For each braze variant, there are some fluctuations in F_{Peak} for individual specimens, which are caused by pore formation, defects, spilling of the braze into the notch and so on. Compared to F_{Peak}, the

fluctuation of F_{Dip} within the same braze is much smaller. For conservative evaluation, F_{Dip} is used to calculate the fracture energy in this thesis. By identifying F_{Dip} in the testing curve, the fracture energy of the respective joint can be calculated according to chapter 3.4.3. For each braze and aging condition, 5 specimens were tested. The results were averaged and taken as the representative fracture energy of the specimen set.

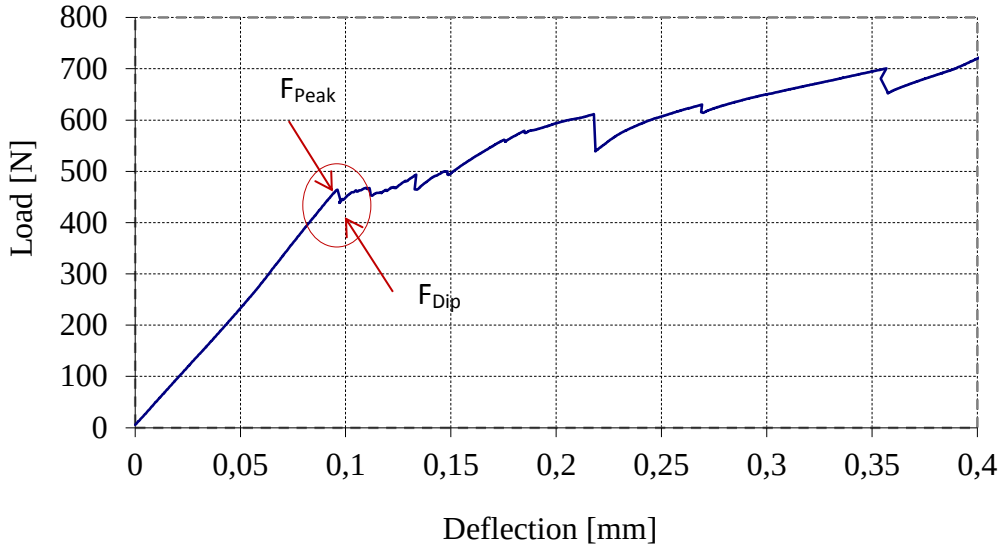


Fig. 3.6 Typical load-deflection curve in ambient temperature delamination testing

The above mentioned calculation method is only valid if F_{Peak} is reached within the elastic region of the specimen. Once F_{Peak} exceeds the elastic limit, plastic deformation of the substrate occurs and consumes part of the stored elastic energy. In this work, the elastic limit is defined by the yield strength of Crofer® 22 H, which is about 390 MPa at room temperature [Lin2]. Utilizing the outlined specimen geometry, the maximum value F_{Peak} (within the elastic range) is calculated to be 568 N, corresponding to a maximum measurable fracture energy of 253 Jm^{-2}. Specimens that yielded F_{peak} loads exceeding the elastic limit, will for that reason simply be denoted with a fracture energy of "$\geq$253 Jm^{-2}"

It should be noted, that this test is only conducted at ambient temperature for several reasons: First, the yield strength of multi-layered specimens is the highest at room temperature, which in turn gives the highest possible measuring limit considering fracture energies. Because of different thermal expansion coefficients of the layers, thermal mismatch stress is accumulated in the specimen during cooling after brazing and reaches the highest values towards low temperatures. Fracture toughness of the multi-layered system reduces with the presence of residual stress [Dre92]. Therefore, the fracture energy of the specimen drops towards low

temperature. Ambient temperature testing values are therefore more appropriate for conservative design. Last but not least, ambient temperature testing is relatively simple to perform, and can easily be applied as a standard screening method for comparing various braze systems.

3.4.3 Data evaluation

The fracture energy of each specimen is calculated according to Charalambides et al. [Cha89] and Hofinger et al. [Hof98]. According to the Euler-Bernoulli beam theory, the bending moment through the cross-section of the specimen can be calculated by the equation

$$M_b = \frac{F_{Dip} l}{2b} \qquad (3.1)$$

b denotes the width of the specimen, F_{Dip} indicates the measured crack inhibition force as mentioned in the previous chapter and l is the distance between the outer and inner loading pins. The fracture energy can thus be calculated by the following equation

$$G_{ss} = \frac{M_b^2 (1-v_2^2)}{2E_2} \left(\frac{1}{I_1} - \frac{1}{I_c}\right) \qquad (3.2)$$

Here the moments of inertia I_2 and I_c can be calculated by:

$$I_2 = \frac{h_2^3}{3} \qquad (3.3)$$

$$I_c = \frac{h_2^3}{3} + k\,\frac{h_1^3}{3} + \mu\left(\frac{h_d^3}{3} + h_d^2 h_1 + h_1^2 h_d\right) - \frac{[h_2^2 - k h_1^2 - \mu (h_d^2 + 2 h_1 h_d)]^2}{4 (h_2 + k h_1 + \mu h_d)} \qquad (3.3)$$

With:

$$k = \frac{E_1 (1 - v_2^2)}{E_2 (1 - v_1^2)} \qquad (3.4)$$

$$\mu = \frac{E_d (1 - v_2^2)}{E_2 (1 - v_d^2)} \qquad (3.5)$$

In these equations, h_1, h_2, h_d indicate the thicknesses of braze, the steel substrate and the ceramic joining partner (Tab. 3.1). E_1, E_2 and E_d are the elastic moduli of the respective layers, here: $E_1 = E_{CroFer22H} = 208$ GPa [Lin2], $E_2 = E_{braze} = 80$ GPa [Bin06], $E_d = E_{SOFC} \approx 100$ GPa [Mal03]. In this work, the Poisson ratios v_1, v_2 and v_d were chosen as 0.3 for all materials.

3.5 High temperature double shear testing

Due to the thermal mismatch of the ceramic and metallic materials in planar SOFC stacks, horizontal shear stress is generated within the multi-layered joining system upon temperature changes (Fig. 3.7). The braze joints are predominantly subjected to shear stresses [Mal07]. Therefore, shear deformation tests have high relevance in characterizing the mechanical behavior of the joints. Symmetric double shear specimens joined by the braze variants stated in section 3.1 were tested at different temperatures (550 ℃, 675 ℃, 800 ℃).

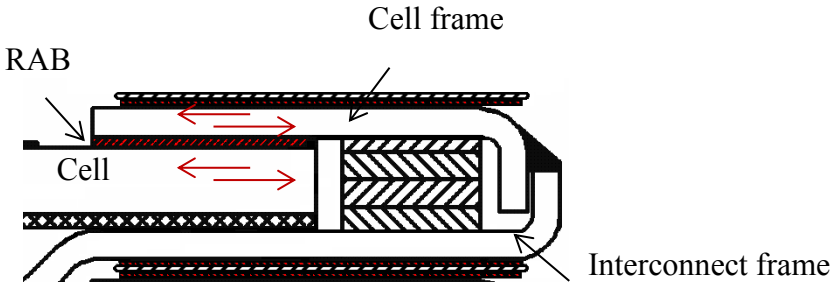


Fig. 3.7 Schematic drawing of a cell to cell-frame braze joint in light weight planar stack design. Shear stresses develop between the metallic cell frame and cell

3.5.1 Sample geometry

The double shear testing specimen is designed according to the ENV 658-6 [Din93] standard. The advantage of this testing method is its simple specimen geometry and loading setup, as shown in Fig. 3.8. Two steel blocks with the geometry of 10 mm × 12 mm × 8 mm are brazed symmetrically to both sides of the ESE (Electrolyte/Substrate/Electrolyte) unit. The SOFC half-cell is composed of the anode material NiOx coated with 8YSZ electrolyte on both sides (chapter 3.1.2). The geometry of the ESE unit is about 12 mm × 12 mm × 1.5 mm.

The specimens are placed on the machine table and the ESE-unit is centered above the notch of 2.5 mm width. During testing, the specimen is loaded by a semi-sphere placed onto the ESE-unit for homogeneous force distribution. Before testing, both the upper surface of the ESE-unit (loading surface) and the bottom surface of the specimen are parallelly aligned to each other by grinding to avoid torsion of the ESE.

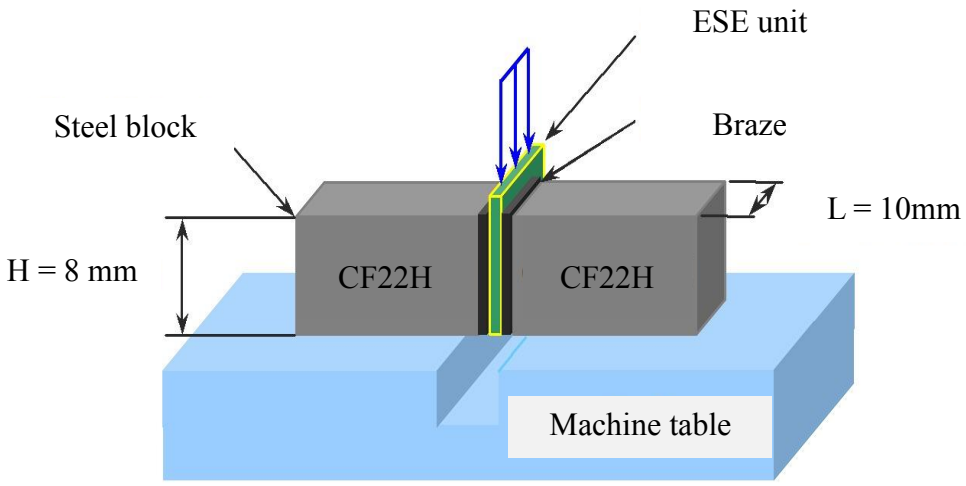


Fig. 3.8 Schematic view of the symmetric double shear testing set-up

Under compression loading, the ESE-unit is pushed into the notch of the table. Within the braze joint, both interfaces (braze/ceramic interface, braze/steel interface) are loaded causing shear deformation [Maj03].

For the ease of handling, the notch width in the table is a little wider than the thickness of the ESE plus the thickness of the two braze joints (notch width: 2.5 mm, $D_{ESE} + 2D_{Braze} \approx 1.7$ mm). This setup would inevitably introduce a slight bending moment into the specimen during shear testing. According to Mayr et. al [May95], the proportion of bending (v_b) and shear deformation (v_s) can be estimated by the equation:

$$\frac{v_s}{v_b} = \frac{2(1-v_2)H^2}{V^2} \qquad (3.6)$$

H denotes the height of the specimen, v_2 is the Poisson ratio and V is the distance between the braze/steel interface and the notch edge. In our case, with V = 0.45 mm, H = 8 mm, v_b = 0.3, shear deformation is estimated to be about 440 times higher than bending deformation.

3.5.2 Execution of tests

All double shear tests were conducted in an Instron Type 8862 testing machine. The testing setup is displayed in Fig. 3.9. During the experiment, the specimens are heated up to the designated testing temperature by a resistance furnace placed around the load jig. The heating rate was about 10 K/Min. Two different testing procedures were performed to characterize the shear strength and creep resistance of the joints, i.e. constant rate shear deformation and stress relaxation tests.

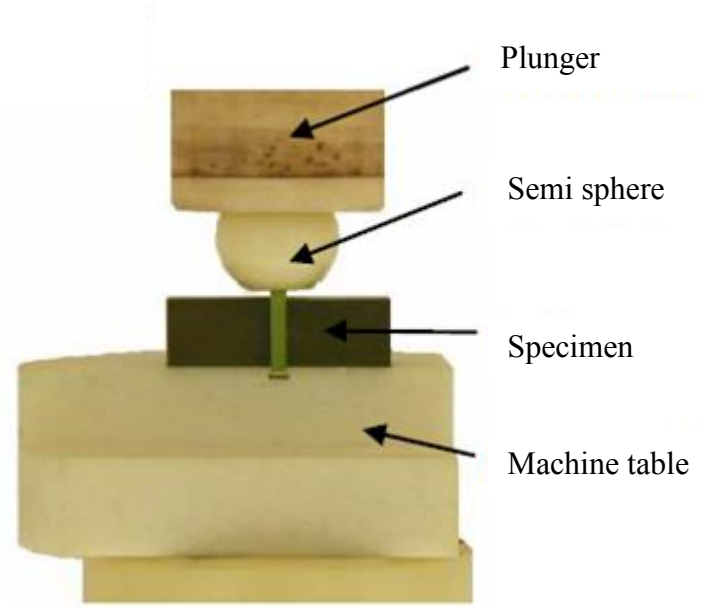


Fig. 3.9 Testing set-up for double shear testing

- Constant deformation rate testing

This testing procedure is performed to characterize the shear strength of the braze joint. The specimens are loaded with a constant deformation rate of 3 µm/Min at three different temperatures (550 ℃, 650 ℃, 800 ℃) up to a maximum shear deformation of about 0.2 mm.

- Stress relaxation testing

As stated in chapter 2.2.2, creep resistance of the braze joints can be characterized by stress relaxation testing. During the test, the specimen is loaded with constant deformation rate (in this case 3 µm/Min) up to the maximum shear stress (determined from the constant deformation rate tests). In deformation control mode, the deformation of the specimen reached after loading is then actively controlled and kept constant by adjusting the cross-head position during the relaxation phase. The end of the relaxation phase is reached at a 75% drop from the maximum load. With the equations stated in chapter 2.2.2, the creep rate of the specimen can thus be derived from the decrease of the applied stress.

3.5.3 Data evaluation

The shear stress τ can be calculated from the applied force F, the corrected specimen deformation δ_{corr} and the sample geometry. (corrected for machine deformation, cf. chapter 3.5.5) by the following equations [Maj03]:

$$\tau = \frac{F}{2L(H-\delta_{corr.})} \quad (3.7)$$

During deformation, the change of the braze cross-section should be taken into account and therefore the width H of the brazed area is reduced by $\delta_{corr.}$. Moreover, because the specimens are symmetric, a factor of 2 taken into account to acquire the effective brazing area. The shear strain is calculated by the corrected specimen deformation divided by the thickness $d_L$of the braze, as shown in Equation 3.8:

$$\gamma_{ges.} = \frac{\delta_{corr.}}{d_L} \quad (3.8)$$

3.5.4 Correction of machine deformation

Fig. 3.10a displays the principle of the strain measurement set up, utilized in high temperature double shear testing. Because of the machine configuration, the exact shear displacement between the ESE unit and the steel blocks can not be measured directly. Instead, the measured displacement contains the elastic deformation of the cell material and part of the load train, which can be expressed by the following equation:

$\delta_{corr} = \delta_t - \delta_m - \delta_e$ (3.9)

Here δ_{corr} is the corrected specimen displacement, δ_t denotes the total displacement (that is measured during the test), δ_m indicates machine deformation and δ_e the elastic deformation of the ESE.

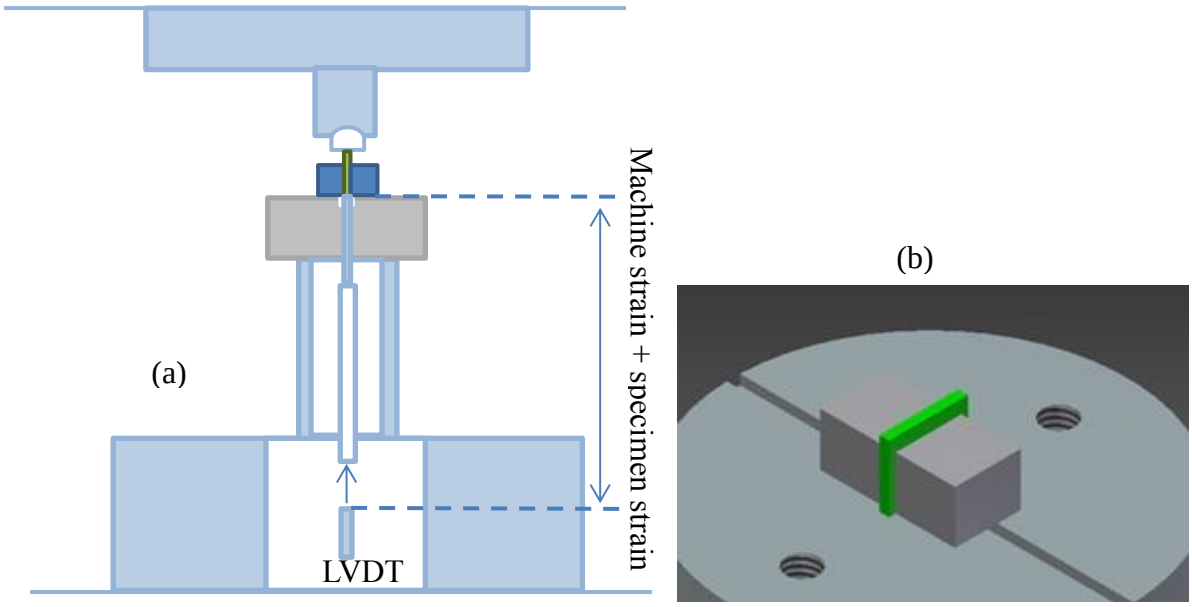


Fig. 3.10 Schematic view of the strain measurement setup in machine (a); positioning of the specimen for the evaluation of machine and elastic ESE deformation (b)

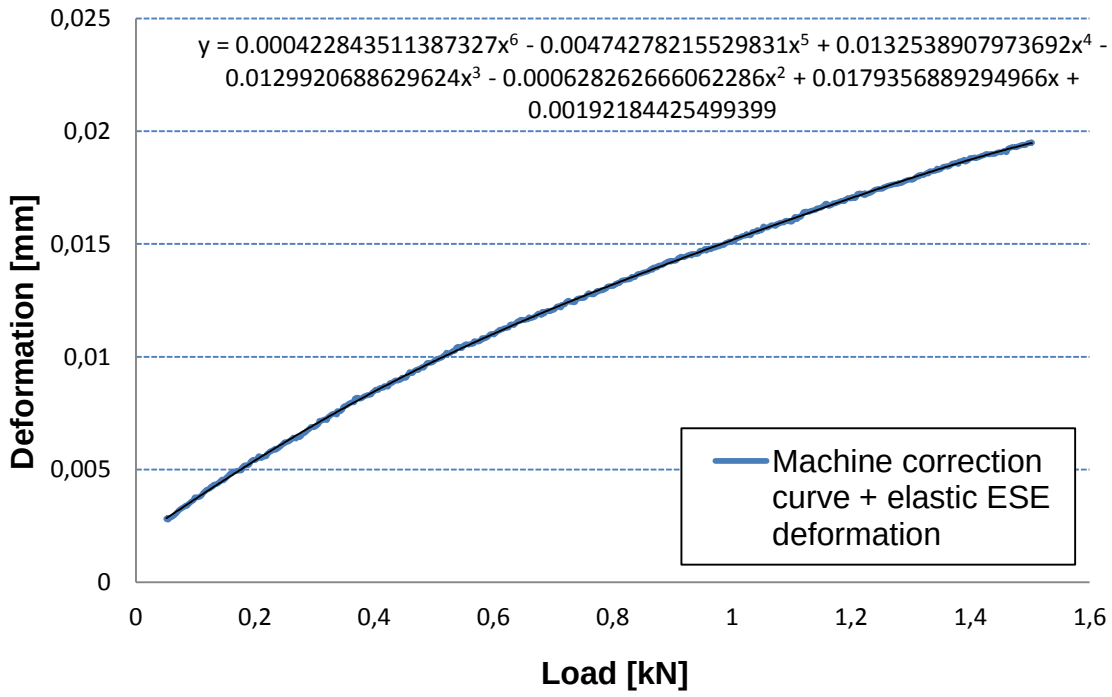


Fig. 3.11 Elastic ESE and machine deformation versus load at 800 ℃

To measure the elastic deformation of the ESE unit and the load train, a dummy sample was placed on the machine table with the ESE unit perpendicular to table notch, as displayed in Fig. 3.10b. Loading of the dummy sample was carried out in the same way like in ordinary double shear testing. In this setup, only elastic deformation of the ESE and the machine

corresponding to the loads occurs. A typical load/deformation curve is shown in Fig. 3.11. A 6^{th} order polynomial was chosen to fit the recorded load/deformation curve. With the obtained equation (Fig. 3.11), the elastic deformation of the specimen and the machine was calculated according to the applied load to obtain the corrected specimen deformation (Equation 3.10). The machine curves were obtained and fitted at the three testing temperatures of 550 ℃, 675 ℃, and 800 ℃. Tab. 3.3 contains the parameters of the 6^{th} order polynomial equations (3.10) obtained at the testing temperatures.

$$\delta_{corr.} = \delta_t - (\delta_m + \delta_e) = \delta_t - (aF^6 + bF^5 + cF^4 + dF^3 + eF^2 + fF + g) \quad (3.10)$$

Tab. 3.2 Temperature dependent parameters of the machine deformation correction curve

T (℃)	a	b	c	d	e	f	g
800	4.2×10^{-4}	-4.7×10^{-3}	1.3×10^{-2}	-1.3×10^{-2}	-6.3×10^{-4}	1.8×10^{-2}	1.9×10^{-3}
675	-3.5×10^{-4}	3.2×10^{-3}	-1.1×10^{-2}	1.9×10^{-2}	-1.9×10^{-2}	2.1×10^{-2}	3.1×10^{-3}
550	-1.8×10^{-5}	3.8×10^{-4}	-2.6×10^{-3}	7.8×10^{-3}	-1.3×10^{-2}	2.2×10^{-2}	1.1×10^{-2}

4. Results and discussion

4.1 Interfacial adhesion: As-brazed state

During the joining process, thermochemical reactions are expected at the interfaces, which promote adhesion between two different materials. Adhesion mechanism and resulting adhesion strength are very important aspects for characterization of joint properties. As discussed in chapter 3.4.2, the interfacial adhesion strength is investigated and characterized by notched multi-layer samples in four point bending tests at ambient temperature.

4.1.1 Steel/braze interface

For reactive air brazed joints, the steel/braze interfaces are usually the weakest link in four-point bending tests at ambient temperature, because of the pressure of brittle interfacial layers [Kuh08, Bra12].

- **Pure Ag braze**

Fig. 4.1 shows typical braze/steel interfacial microstructures of pure Ag brazed with bare (Crofer® 22 H) and pre-oxidized steel (Crofer® 22 H_v). Both joints exhibit excellent mechanical strength, with fracture energies higher than the measuring limit of the experimental setup ($\geq$ 253 J/m^2). Compared to Crofer® 22 H/Ag/TZ3Y joints, Crofer® 22 H_v/Ag/TZ3Y joints show thicker interfacial layers with more homogeneous thickness. For both joint types, the interfacial layers are composed of (Cr,Mn)O spinel, the chemical composition and crack propagation at the interface is schematically displayed in Fig. 4.2, which is proven by EDX mapping and line scan.

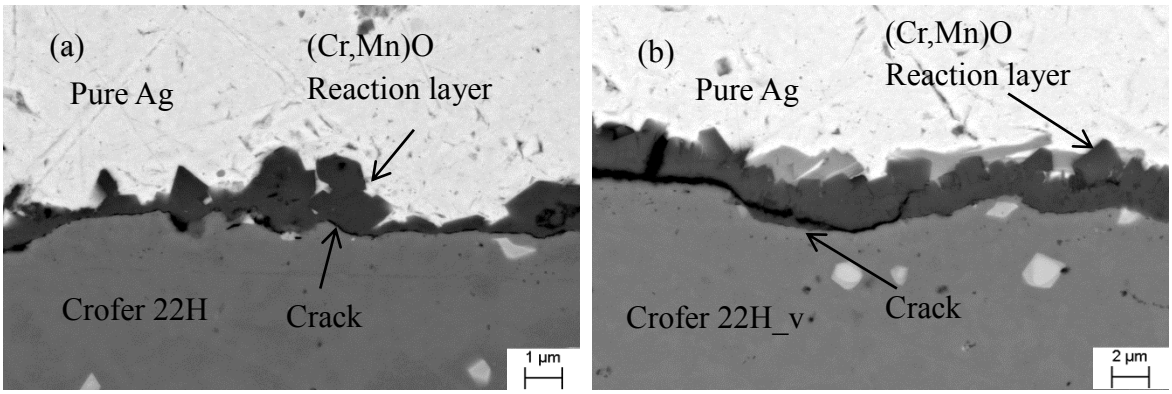


Fig. 4.1 Microstructure of the steel/braze interface a) Crofer 22H; b) Crofer 22H_v

Apart from the thickness difference of the reaction layer, distribution of the elements (Cr, Mn) is also slightly different for both types of joints. The Cr and Mn contents of the Crofer® 22 H/Ag/TZ3Y joints are relatively homogeneous throughout the interfacial reaction layer, while Crofer® 22 H_v/Ag/TZ3Y joints show a higher Cr content in the lower part of the reaction layer. Moreover, increased Mn content is observed in the upper part of the reaction layer in Crofer® 22 H_v/Ag/TZ3Y joints. The same phenomenon was observed for Crofer® 22 APU_v/Ag/TZ3Y joints in the as-brazed state [Kuh08]. This observation also corresponds to literature reports on Crofer® 22 steels with the formation of a duplex scale consisting of an outer $(Mn,Cr)_3O_4$ layer and an inner Cr_2O_3 layer on the steel surface after annealing at 900 ℃ in air [Fro08]. Obviously, diffusion of scale forming elements and thus oxidation of the steel surface is changed by the presence of Ag in the brazing process. For both joint types, cracks mainly initiate and propagate along the brittle interfacial oxide layer, specifically at the bottom of the reaction layer close to the steel surface.

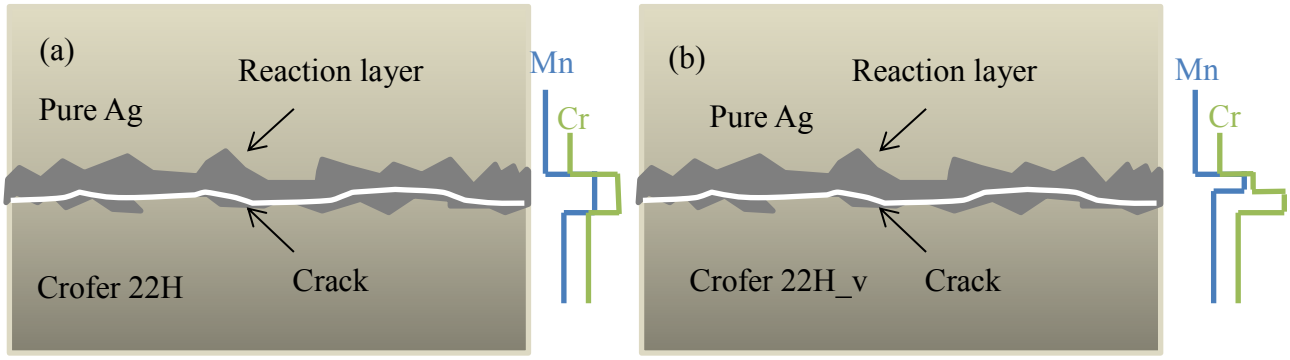


Fig. 4.2 Schematic drawing of typical crack progress layer and the elemental (Cr,Mn) distribution in the reaction layer: a) Crofer® 22 H/Ag/TZ3Y joints; b) Crofer® 22 H_v/Ag/TZ3Y

Former investigation [Kuh08, Bra12] and this thesis prove that ferritic Crofer® 22 steels exhibit satisfactory as-brazed joint properties when brazed with TZ3Y using Ag-based brazes. To further study the joint properties of joining partners with dissimilar thermal expansion coefficient by reactive air brazing, austenitic steel 1.4841 was chosen as an alternate steel joining partner with a thermal expansion coefficient of 19 ppm/ K. Brazing of 1.4841with TZ3Y by pure Ag failed, with specimens delaminating during cooling down from brazing. Delamination mainly occured at the braze/steel interface. Fig. 4.3 shows delaminated interfaces of the both sides. On the steel surface, only traces of (Cr,Mn)O spinel and pure Ag can be observed. Most of the interfacial layer ((Cr,Mn)O spinel), formed during brazing, delaminated from the steel surface and adheres to the Ag braze (Fig. 4.3b). According to literature [Qu06], the thermal expansion coefficient of $MnCr_2O_4$ spinel is about 7.2 ppm/K, which differs greatly from the bulk steel. During cooling down from brazing, high residual stress is induced at the interfaces, leading to delamination at the braze/steel interface.

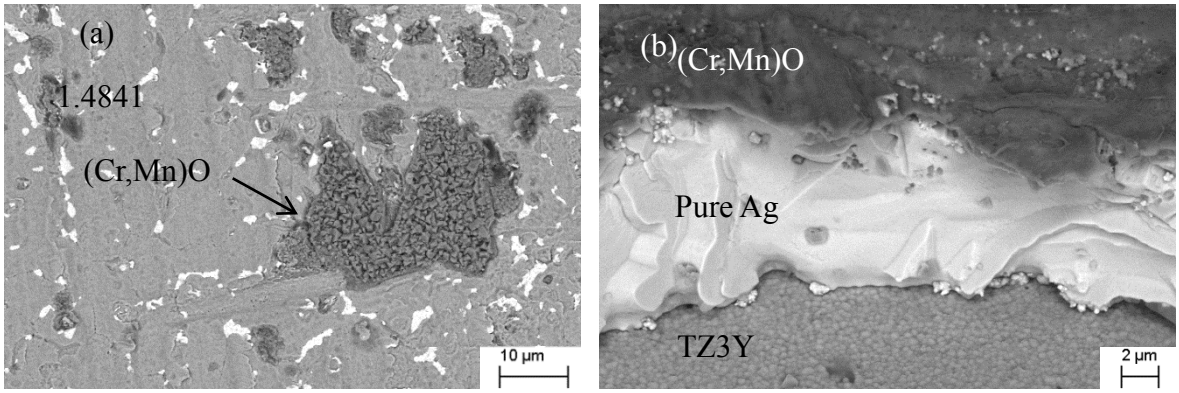


Fig. 4.3 Delaminated surface of the 1.4841/pure Ag/TZ3Y joint: (a) Steel surface; (b) ceramic/braze interface

- **AgCu brazes**

As stated in chapter 2.5.2, with the addition of Cu, the wetting behavior of Ag brazes is greatly improved. Cu reacts with oxygen and other elements from the steel substrate, forming mixed reaction layers at the braze/steel interface. Fig. 4.4 shows an overview of the cross-section of a Crofer® 22 H/Ag4Cu/TZ3Y joint. Lots of pores can be observed within the braze matrix.

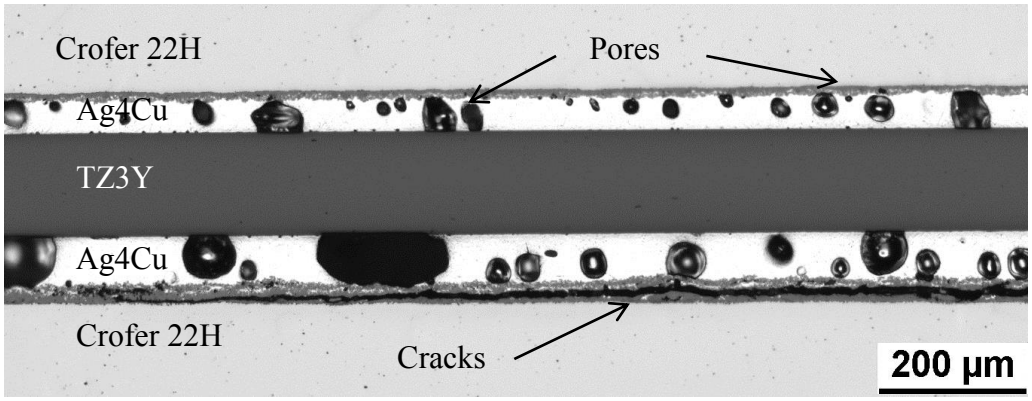


Fig. 4.4 Cross-sectional overview of a Crofer® 22 H/Ag4Cu/TZ3Y braze joint

Fig. 4.5 shows the morphologies of the reaction layers at steel/braze interfaces of Crofer® 22 H/Ag4Cu/TZ3Y and Crofer® 22 H/Ag8Cu/TZ3Y joints. The thickness of the reaction layer in the Ag4Cu joint is about 5 µm, and thus less than that of the Ag8Cu joint with a thickness of about 10 µm. Cracks initiate and propagate through the reaction layer in both joint types, which is schematically shown in Fig. 4.6, the chemical composition of which is proven by EDX mapping and line scan. The chemical composition of the reaction layers is similar in both types of joints. Mn, Fe and Cu are homogeneously distributed and Cr enriches at the bottom of the reaction layer (Fig. 4.6). The fracture energy of the Ag4Cu joints is ≥ 253 J/m^2 (exceeds the measuring limit of the experimental setup) and is thus higher than that of the Ag8Cu joint (129 ± 39 J/m^2). Both joints fail within the reaction layer at the braze/steel interface. The reduced strength of the Ag8Cu joints may be caused by two reasons: 1. Increased pore content in the braze matrix; 2. Increased volume of the brittle reaction zone. Therefore, despite of the enhanced wettability with increasing Cu content, the decreasing joint strength should also be taken into consideration when applying Cu-containing Ag brazes.

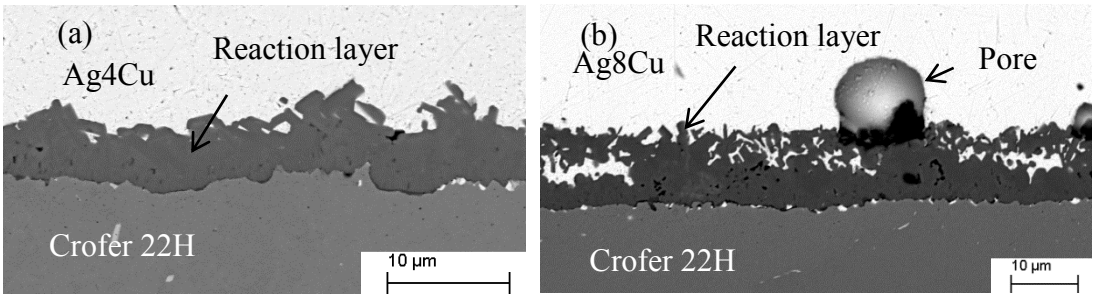


Fig. 4.5 Morphology of the reaction layer at braze/steel interface. a) Crofer® 22 H/Ag4Cu/TZ3Y; b) Crofer® 22 H/Ag8Cu/TZ3Y

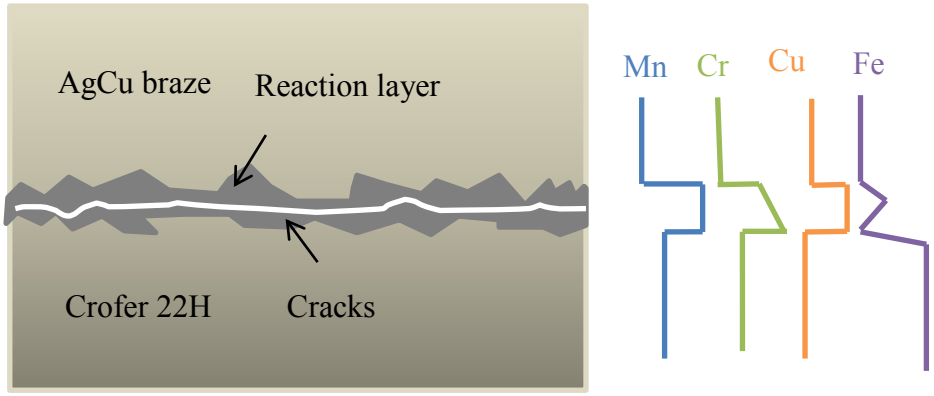


Fig. 4.6 Schematic illustration of the elemental distribution in the reaction layers of AgCu joints

As discussed previously, 1.4841/Ag/TZ3Y joints fail during cooling from brazing because of the great mismatch in thermal expansion coefficients of the (Cr,Mn)O reaction layer and the steel substrate. With addition of Cu to the Ag braze, the thermal and chemical properties of the resulting interfacial reaction layer changes. Ag4Cu was therefore also tried for brazing 1.4841 and TZ3Y. The resulting joints remain intact after brazing. Nevertheless, the low fracture energies (< 10 J/m^2) of the joints indicate poor adhesion strength at the braze/steel interface. Fig. 4.7 shows a cross-sectional overview of a delaminated 1.4841/Ag4Cu/TZ3Y joint after a four point bending test. It can be clearly seen, that delamination occurred between the reaction layer and the steel surface. In this case, although the 1.4841/Ag4Cu/TZ3Y joints did not delaminate after brazing, the interfacial residual stress is still very high after cooling from brazing. With high interfacial residual stress, small additional mechanical load can cause joint failure.

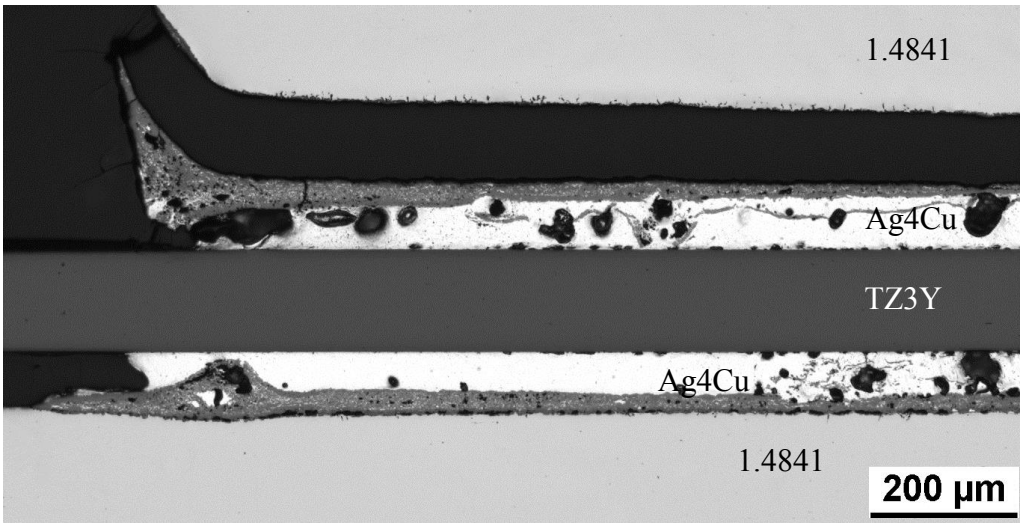
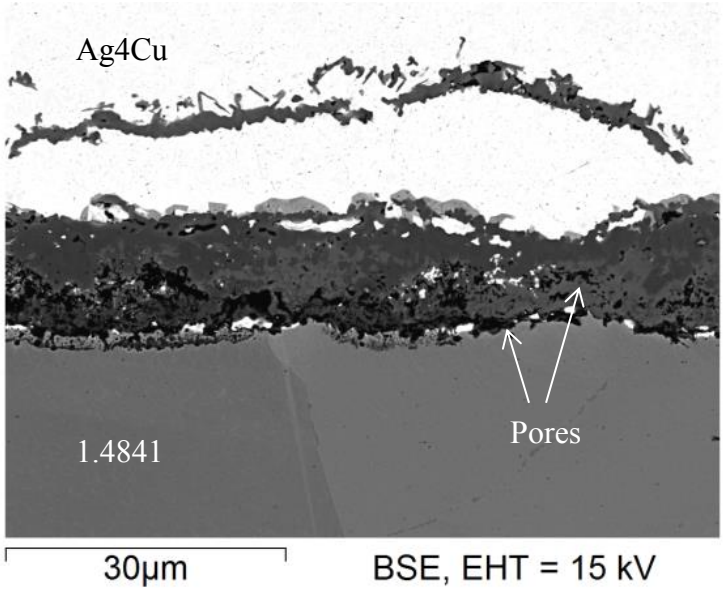


Fig. 4.7 Cross-sectional overview of the delaminated 1.4841/Ag4Cu/TZ3Y joint

Detailed microstructural analysis reveals the interfacial reaction layer to be porous, especially in close vicinity to the 1.4841 steel surface (Fig. 4.8). At the steel/reaction layer interface, lots of pores can be observed, what might indicate damage from residual stress. This is probably another reason for the low adhesion strength at the braze/steel interface. Therefore, for joining 1.4841, alloying of Cu to the Ag braze does not seem to greatly enhance the mechnical properties.



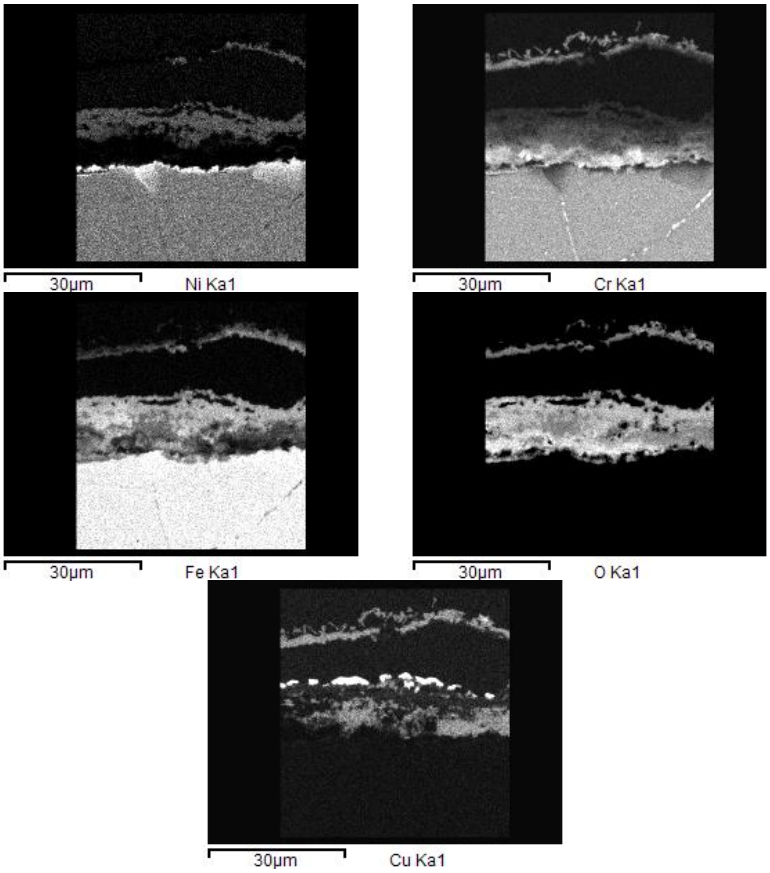


Fig. 4.8 Element mapping of the reaction layer at the braze/steel interface of a 1.4841/Ag4Cu/TZ3Y joint

- **Ag0.5Al brazes**

As discussed in Chapter 3.1.1, the first trial to produce Ag0.5Al braze foils was undertaken by PVD coating of Al on Ag foil. The joints brazed by PVD coated Ag0.5Al foils exhibit low joint strength (G_{ss} < 10 J/m^2), because the PVD coated side neither adheres to the ceramic nor to the steel surface (Fig. 4.9). EDX analysis of the delaminated braze/steel interface (Fig. 4.10) uncovers that only few spots of the steel surface are wetted by the Ag braze. An intact alumina interface layer is found on top of the Ag braze. This alumina layer acts as a diffusion barrier at the interface, keeping the Ag melt away from wetting the steel surface, thus causing bad adhesion between braze and steel. On the other hand, Brandenberg [Bra12] investigated Al-PVD (0.5 mol%) coated Crofer® 22 APU/Ag/TZ3Y joints with PVD coating of Al on the steel surface. Unlike the Crofer® 22 H/Ag0.5Al(PVD)/TZ3Y joints in the present study, the Al-PVD coated Ag foils on Crofer® 22 APU adhere well and the joints exhibit comparatively high strength (Gss = 127 ± 22 J/m^2) [Bra12]. Microstructure analysis shows that a (Al, Cr, Mn)O reaction layer formed at the braze/steel interface, which adheres well to the steel

surface and is fully wetted by pure Ag during brazing. The reason for this differences in adhesion behavior will be discussed later in chapter 4.1.3.

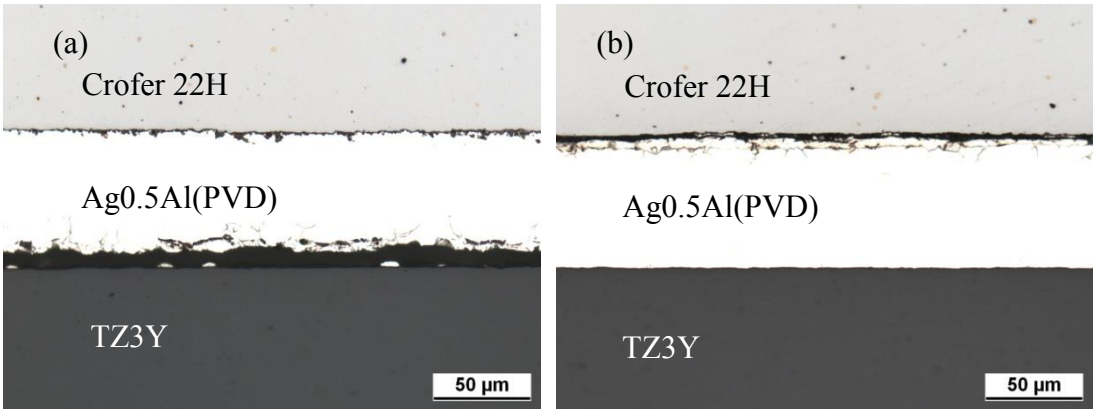


Fig. 4.9 Cross-section of a Crofer® 22 H/Ag0.5Al (PVD)/TZ3Y joint: a) PVD layer towards TZ3Y; b) PVD layer towards steel

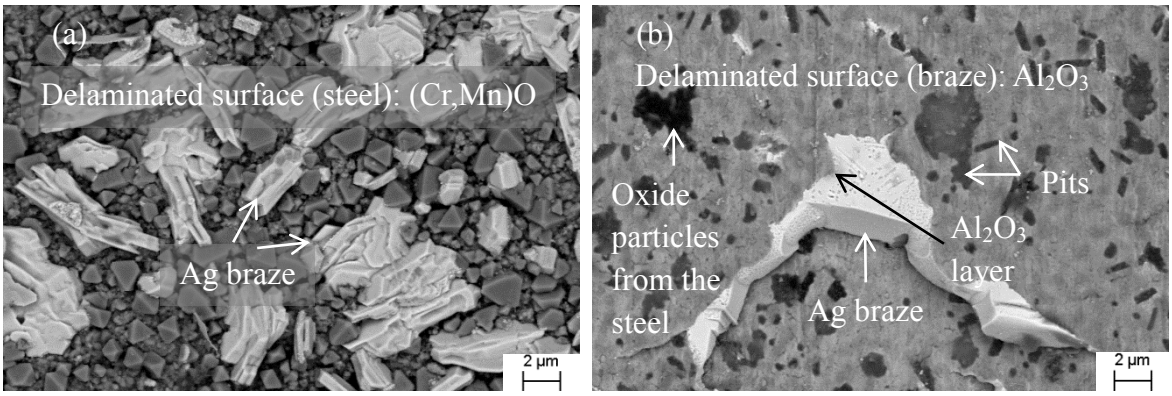


Fig. 4.10 Surface morphology of a delaminated Ag0.5Al(PVD)/steel interface, a) delaminated surface at the steel interface; b) delaminated surface on the braze interface

Another option tested are the Crofer® 22 H/Ag0.5Al(IOT)/TZ3Y joints. The microstructure of a representative cross-section is shown in Fig. 4.11a. Instead of forming a continuous alumina layer, a tenuous (Cr, Mn, Al)O-reaction layer with a thickness of about 1.5 µm forms at the braze/steel interface. Moreover, lots of precipitates are found throughout the braze matrix. Mainly two types of precipitates are found: Acicular (Cr, Al)O and globular Al_2O_3. From the delaminated Ag0.5Al(IOT) joint, it can be observed that (Cr,Al)O precipitates actually have a plate-like morphology (Fig. 4.12). Besides, not only do these joints exhibit optimized microstructure, but also excellent strength, with fracture energies higher than the measuring limit of the experimental setup ($\geq 253 Jm^{-2}$). Cracks initiate and propagate through the reaction layer at the braze/steel interface in ambient temperature delamination testing.

In an attempt to study the influence of pre-treatment to the brazing properties of the Ag0.5Al(IOT) foils and its precipitation behavior, Crofer® 22 H/Ag0.5Al(IOT)_annealed / TZ3Y joints were investigated with Ag0.5Al(IOT) foils annealed at 900 ℃ for 100 h in air. The resulting joints show relatively low strength with a fracture energy of 75 ± 15 J/m^2. Microstructure analysis (Fig. 4.11b) also reveals bad adhesion at the interfaces and less precipitates are found inside the braze matrix. A possible explanation for this would be, that during pretreatment most of the Al diffused to the braze surface and reacted with oxygen, forming Al_2O_3 on the surface of the braze foils. Similar like for the PVD coated braze foils, the formed alumina prevents adhesion at the interfaces and causes a degradation of joint strength.

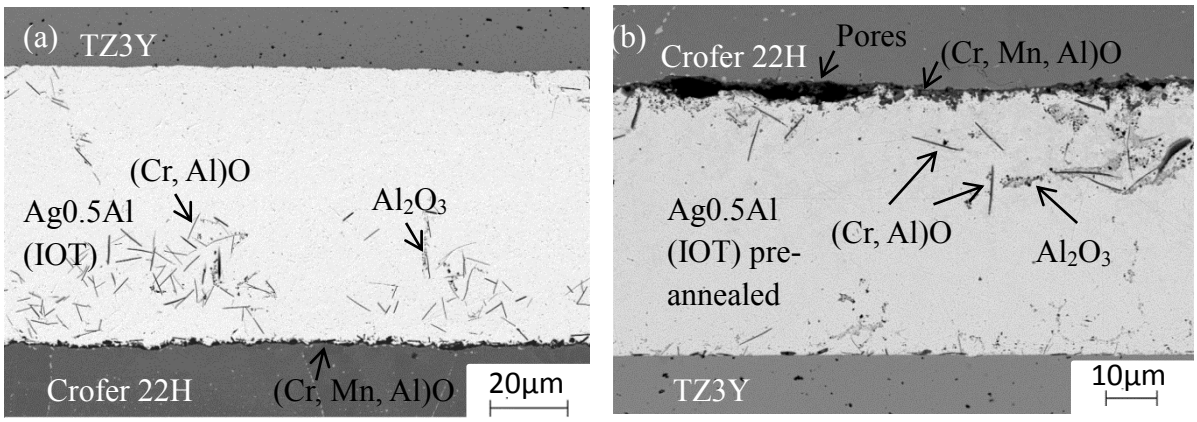


Fig. 4.11 Microstructure of Crofer® 22 H/Ag0.5Al (IOT)/TZ3Y joints: (a) Braze foil in as-received condition; (b) Braze foil annealed in air at 900 ℃ for 100 h prior to brazing

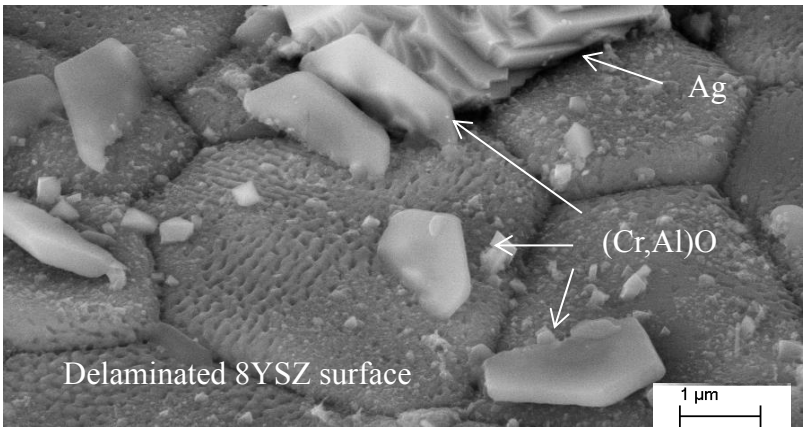


Fig. 4.12 8YSZ surface delaminated in double shear testing

4.1.2 Ceramic/braze interface

For SOFC application, yttria-doped-zirconia is normally used as the electrolyte material and brazed to metallic interconnects to form a so-called repeating unit (chapter 2.1). In our experiments, TZ3Y is applied as the ceramic joining partner in four point bending tests and SOFC half cells (NiOx+8YSZ) are applied in high temperature double shear tests. To study the interfacial morphologies of the braze/ceramic interfaces, SOFC half-cell/pure Ag/TZ3Y joints were brazed for EBSD analysis (Fig. 4.13). No obvious chemical reaction products are found at both ceramic/braze interfaces. The same is encountered for brazing these ceramics with Cu- or Al-containing silver brazes.

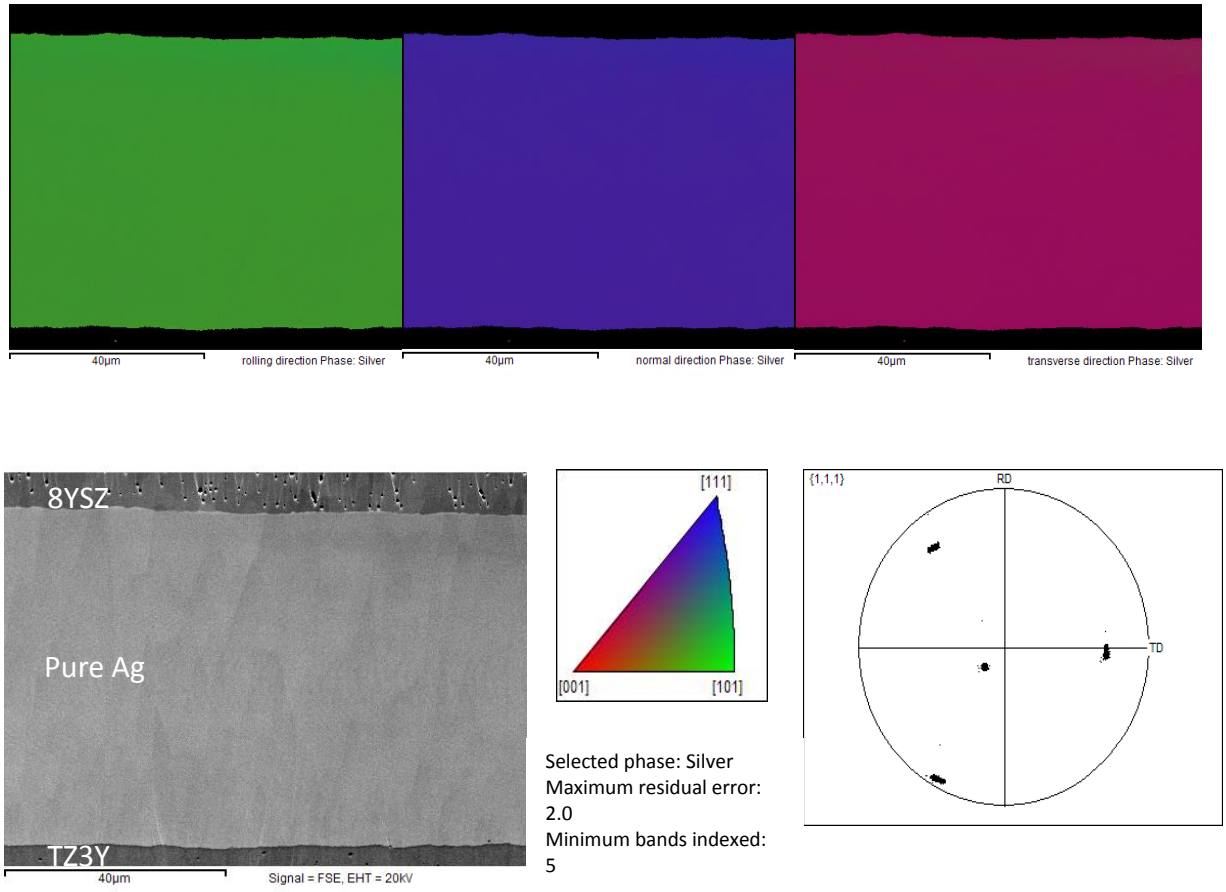


Fig. 4.13 EBSD analysis of the cross-section of an SOFC half-cell/Ag/TZ3Y joint

Nevertheless, at the delaminated braze/ceramic interfaces, a so-called “pitting” phenomenon is found for all braze variants (pure Ag, Ag4Cu, Ag0.5Al) on the ceramic surfaces (Fig. 4.14). The surface of a TZ3Y foil prior to brazing is shown in Fig. 4.14a. Fig. 4.14b displays a TZ3Y surface after thermal cycling of a pure Ag joint. It is important to note that the surface

displayed in Fig. 4.14b was once covered by pure Ag (i. e. the braze matrix). During the thermal cycling test the braze matrix was delaminated, leaving behind some silver residues still attached to the TZ3Y surface. Clearly, the surface that was covered by the silver matrix shows an altered surface morphology: While prior to brazing the grain interiors appeared smooth, some kind of "pitted surface" was formed after the braze matrix was delaminated in the thermal cycling test. The same phenomenon is also discovered for the SOFC half-cell (8YSZ) electrolyte surface in high temperature shear tests (Fig. 4.14c, d). In addition to the "pitted" surface of the grain interior, grain boundaries seem to be "eroded". EDX analysis indicates that the chemical composition of the surface around these pit-like structures is merely zirconia, without any other elements or chemical reaction products.

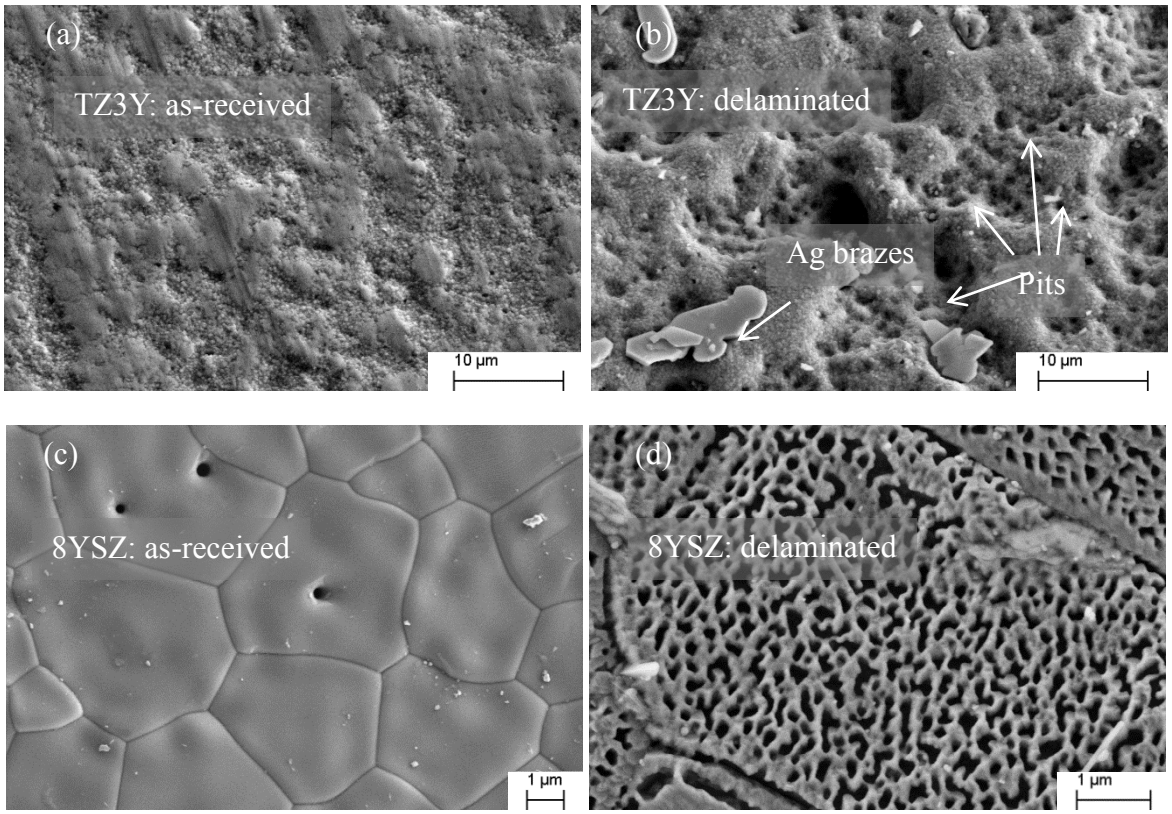


Fig. 4.14 Surface morphologies of TZ3Yand SOFC half-cell electrolyte (NiOx+8YSZ): a) TZ3Y surface: as received; b) TZ3Y surface: delaminated by thermal cycling; c) 8YSZ surface: as received; d) 8YSZ surface: delaminated in high temperature shear testing

Fig. 4.15a clearly reveals the hole-like morphology of the "pits", with sizes of about 200 nm - 500 nm. On the other hand, TEM analysis (Fig. 4.15b) of an intact braze/ceramic interface reveals no signs of chemical interaction between braze and ceramic surface. Considering all the other research results stated in chapter 2.5.1, it is believed that oxygen plays an

important role in the interfacial adhesion. Nevertheless, even with TEM, this thin atomic interfacial monolayer [Muo08, Nai81] is hardly detectable.

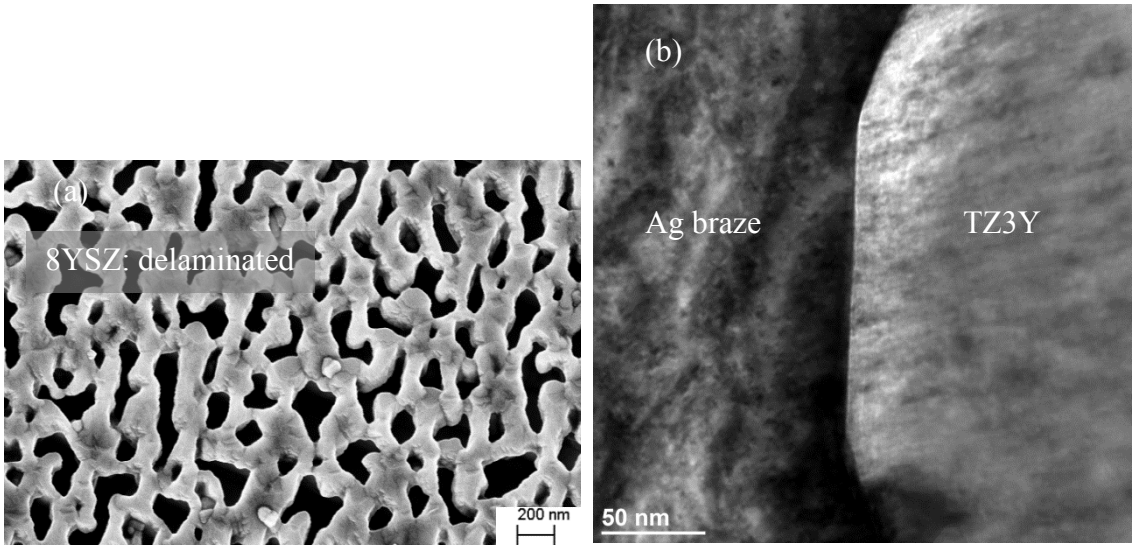


Fig. 4.15 SEM and TEM micro-graphs of (a) delaminated SOFC half-cell surface after double shear testing at 800 ℃; (b) the braze/ceramic interface in the as-brazed state

4.1.3 Discussion and conclusions

The results discussed above show that, with optimization, reactive air brazing is qualified for joining materials used in SOFC applications. For successful joining, there are certain requirements that need to be met at the joining interfaces.

At the braze/ceramic interface, Ag as a braze exhibits excellent adhesion behavior to yttria-doped zirconia in air brazing. No obvious interfacial reaction products were found after brazing. Only traces of "pitting" holes were found on the delaminated zirconia surface. The strong interfacial adhesion at the braze/ceramic interface indicate the existence of strong atomic bonds. Considering the above stated evidence and corresponding literature (cf. chapter 2.5.1), it is believed that oxygen is an indispensable bonding agent at the braze/ceramic interfaces.

On the other hand, even when Ag is brazed to steel in air, it is essentially brazed to the oxide scale formed on the steel surface. As the braze foils and the steel surface do not tightly adhere to each other, the steel surface gets oxidized in air during the heating phase of the brazing process. During brazing, the Ag melt bonds with the oxide scale formed at the steel surface. When other reactive elements are added to the Ag braze, these react with the oxides,

chemically reduce the oxide surface in a way that the wetting behavior is enhanced. It should be kept in mind that the thermal expansion coefficients of the reaction layer and the steel have to correspond well to ensure successful joining. Till now, braze materials or alloying elements for a successful reactive-air-brazing of 1.4841 steel to TZ3Y, are still under research.

It should be noted that different doping methods can be utilized to alloy reactive elements into Ag-based brazes. Coating of Cu by galvanization on the surface of pure Ag foil proves to be successful in producing proper AgCu brazes. Cu seems to have sufficient reactivity with the oxide scale of the steel, forming a thick reaction zone at the braze/steel interface. At the braze/ceramic interface, the Cu galvanized on the braze foil does not exhibit any interaction with the ceramic surface. Instead, the Cu was oxidized and most of the CuO diffused from the braze/ceramic interface into the braze matrix or even to the reaction zone at the braze/steel interface. On the other hand, PVD coating of Al on the pure Ag foil does not enable proper AgAl brazes because of its bad adhesion behavior towards steel and/or ceramic surfaces. During the brazing process Al is oxidized and forms an intact alumina layer on the surface of the Ag melts, preventing the wetting of the steel and ceramic surfaces by molten Ag (see Fig. 4.10b). Because this alumina layer has low reactivity with the (Cr, Mn)O scale formed on the steel surface, it is the cause of the bad adhesion strength of the joints (see Fig. 4.10a).

The reason for the different behavior of Cu and Al probably are the differing oxidation activities of the two elements. The oxidation activities of the elements dealt with in this thesis are in the order: Al > Mn > Cr > Fe > Ni > (H) > Cu > Ag. As Al has higher oxygen affinity, it gets oxidized first and forms continuous alumina layers during the brazing process. When other oxide scale forming elements such as Cr and Mn diffuse from the steel surface, they are not able to reduce the alumina scale, thus causing bad adhesion between the two oxide layers. On the contrary, when CuO forms on the braze surface, it can be reduced by Cr and Mn diffusing from the steel surface and later on be reoxidized by oxygen from the atmosphere or diffusing in the silver melt. This reduction and reoxidation processes promote the interaction between the braze and the steel surface, thus enhancing the adhesion behavior at the interface.

By microstructure analysis, the braze/steel interfacial reaction layer was detected to be the mechanically weakest link in reactive-air-brazed Crofer® 22 H/Braze/TZ3Y joints in ambient temperature delamination tests. Nevertheless, this reaction layer is inevitable in air brazing, because oxygen is indispensable for interfacial adhesion: Ag proved to be able to strongly

adhere to the ceramic without any addition of reactive elements just in presence of oxygen (cf. chapter 2.5.1).

4.2 Interfacial adhesion: Aged

During the operation of SOFCs, the brazed stack components operate under so-called "dual atmosphere conditions" (air on the cathode side, p_{O2}: 10^{-13} Pa) and fuel gas on the anode side (p_{O2}: 21 kPa) in the temperature range from 650 ℃ to 900 ℃. Therefore, high temperature isothermal aging resistance of the brazed joints under oxidizing and reducing atmosphere is one of the important issues. To study possible aging, specimens for four point bending tests were prepared and isothermally annealed in two different atmospheres (air and Ar4vol%H_2). The mechanical behavior and microstructures of the aged specimens were then investigated and characterized by room temperature delamination tests and subsequent SEM examination. In this chapter, pure Ag, Ag4Cu and Ag0.5Al(IOT) joints are investigated, because of their relatively good mechanical strength and microstructure in the as-brazed state.

4.2.1 Aging in air

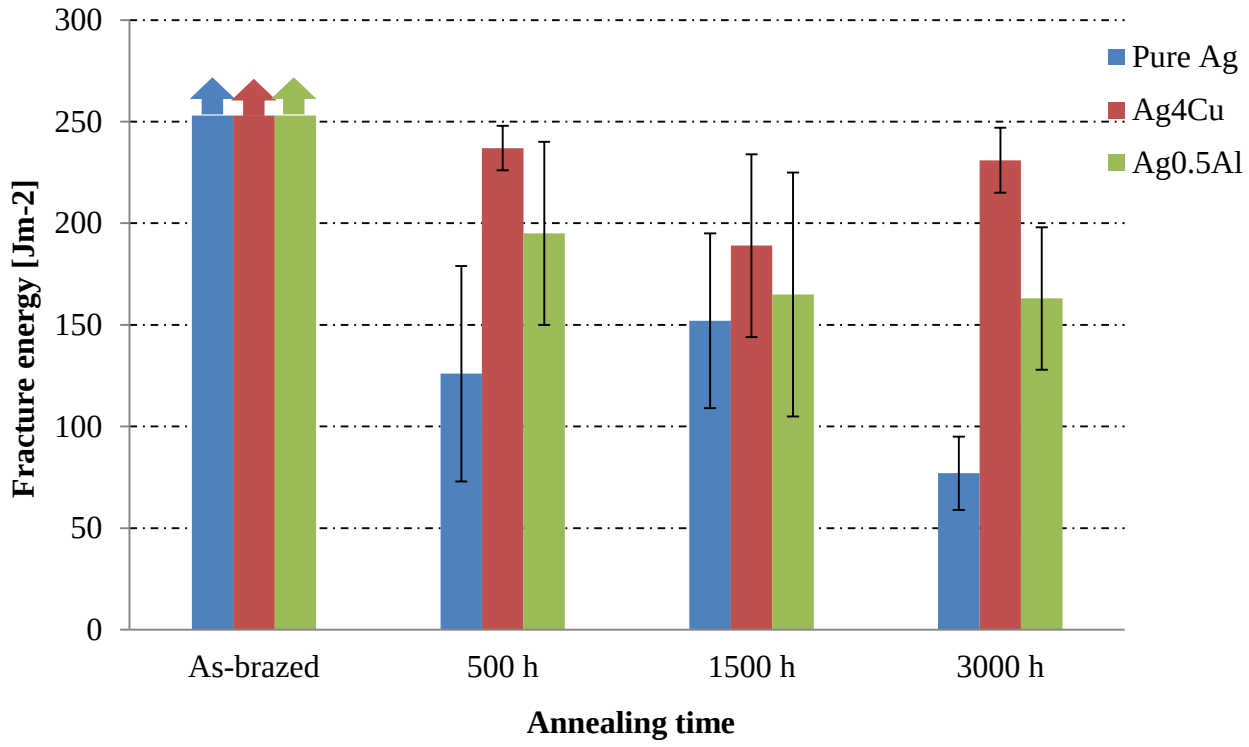


Fig. 4.16 Fracture energies of the joints (pure Ag, Ag4Cu, Ag0.5Al) after air annealing at 800 ℃ with differing annealing time

For all the three braze variants, the fracture energies of the joints decrease with increasing annealing time (Fig. 4.16). Ag4Cu seems to have the highest aging resistance in air of the three variants, while pure Ag joints have the lowest aging resistance. For all three joints, the decrease of the fracture energy per time seems to be more pronounced during the first 500 hours of annealing than afterwards. The microstructure of each variant was analyzed by SEM separately and will be discussed in detail in the following.

- **Pure Ag joints**

Fig. 4.17a shows the morphology of the reaction layer at the braze/steel interface of a pure Ag joint after 1500 hours of annealing in air at 800 ℃. Compared to the as-brazed state, not only the thickness of the reaction layer grew during air annealing, but also the chemical composition of the layer differs from the original one. Two layers of different chemical compositions are observed at the braze/steel interface in all air annealed specimens regardless of different annealing time. The lower part of the reaction layer in Crofer® 22 H/Ag/TZ3Y joints with darker color shown in Fig. 4.17a is composed of (Cr, Mn)O, which has the same chemical composition as the original oxide layer in the as-brazed state (see Fig. 4.1a). The upper layer with lighter color is composed of (Cr, Ag, Mn)O, which newly formed during annealing. Cracks are observed propagating through the upper layer of the reaction zone. Until now there is no literature published on the detailed chemical reactions of Ag with Cr-oxides at 800 ℃. Nevertheless, it is reported that the reactions of Ag(s) and Cr-oxides at 500 ℃ are as follows: $2(2Ag + Cr_2O_3) + O_2 = 2Ag_2Cr_2O_4$ (formation of chromite). However in the presence of Ag, the reaction proceeds according to $2Ag + Ag_2Cr_2O_4 + 2O_2 \leftrightharpoons 2Ag_2CrO_4$ (chromate). The latter reacts with Cr_2O_3 according to $Ag_2CrO_4 + Cr_2O_3 \rightarrow Ag_2Cr_2O_4 + CrO_3$ [Sch42]. With these equations, it can be speculated that Ag can react with Cr-oxides to form a stable phase at 800 ℃ in the presence of oxygen.

On the other hand, it was reported previously by Kuhn [Kuh08] that by pre-oxidation (800 ℃, 100 h) of the steel surface, the aging resistance of Crofer® 22 APU/Ag/TZ3Y joints in air can be greatly improved. Therefore, Crofer® 22 H_v/Ag/TZ3Y joints were annealed in air at 800 ℃ for 500 hours for a direct comparison to Crofer® 22 H/Ag/TZ3Y joints. The fracture energy of the preoxidized Crofer® 22 H_v/Ag/TZ3Y joints after 500 hours annealing in air is about 77 ± 17 J/m^2. Compared to Crofer® 22 H/Ag/TZ3Y (126 ± 53 J/m^2) this is much lower. Microstructural analysis indicates that, although Crofer® 22 H_v/Ag/TZ3Y joints present a similar double-layer morphology of the reaction zone, the chemical composition is slightly

different from that of the Crofer® 22 H/Ag/TZ3Y joints, Fig. 4.17b. The reaction layer of Crofer® 22 H_v/Ag/TZ3Y is composed of Cr_2O_3 and (Cr, Ag)O, without any detection of Mn. Instead, (Cr, Mn)O spinel distributes as particles within the upper layer of the reaction zone. In contrast to Crofer® 22 H/Ag/TZ3Y joints, cracks propagate within the lower part of the reaction zone (Cr_2O_3 layer) in Crofer® 22 H_v/Ag/TZ3Y joints. From the above discussed phenomena, two conclusions can be drawn: 1. Although the Mn content is very low in the reaction layer, it has great influence on the fracture strength of the reaction layer; 2. Pre-oxidation of Crofer® 22 H degrades the aging resistance of the joint.

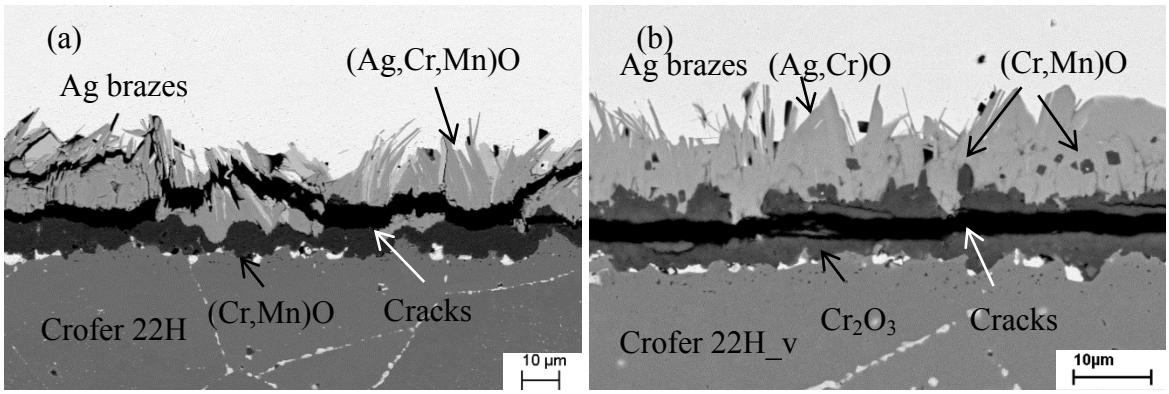


Fig. 4.17 Microstructure of the braze/steel interface after 500 h of air annealing (a) Crofer® 22 H/Ag/TZ3Y; (b) Crofer® 22 H_v/Ag/TZ3Y

- **Ag4Cu joints**

In Ag4Cu joints after air annealing, delamination occurs along the reaction layer at the braze/steel interface in ambient temperature bending tests (Fig. 4.18). Similar to pure Ag joints, the reaction layer of Ag4Cu joints exhibits duplex morphology after air annealing.

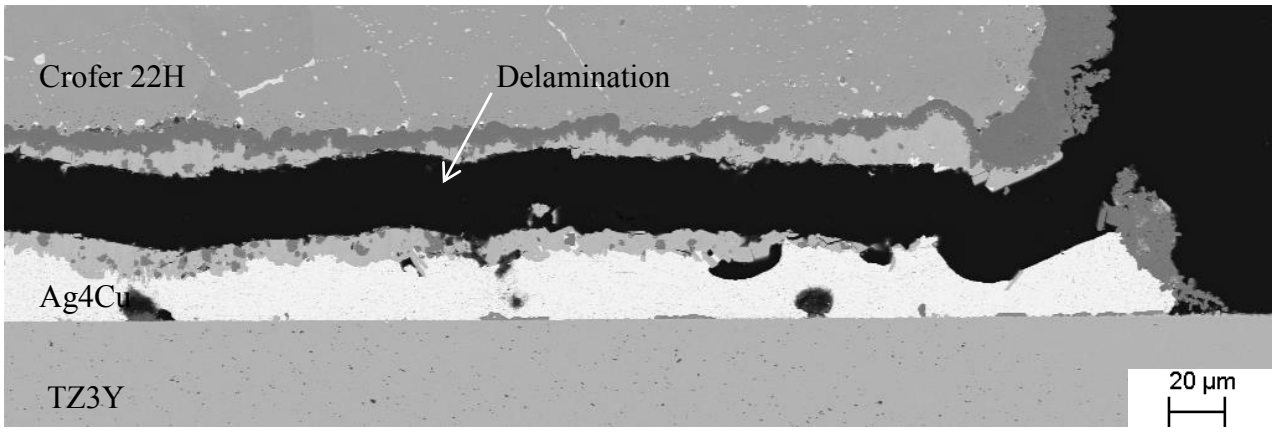
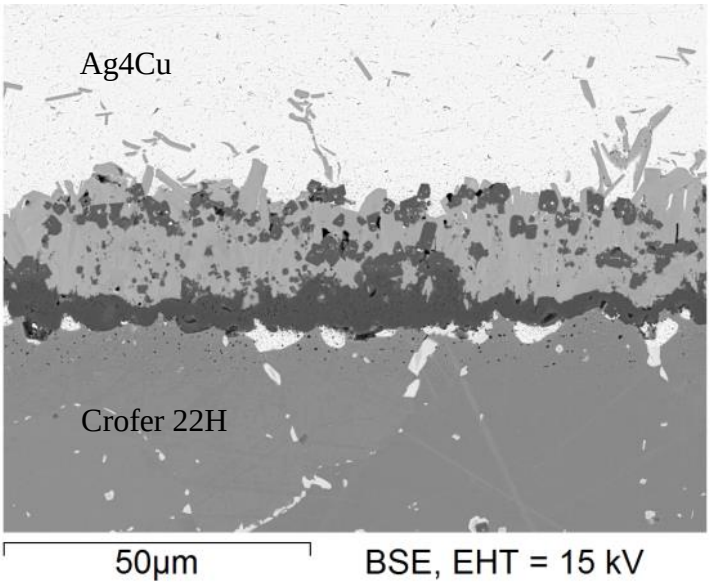


Fig. 4.18 Microstructure of Crofer® 22 H/Ag4Cu/TZ3Y joints after 3000 hours of annealing in air at 800 ℃

Fig. 4.19 shows the chemical composition of the reaction layer after 3000 hours of annealing. The bottom layer of the reaction zone is composed of (Cr, Mn)O, while the upper layer is composed of (Cr, Mn, Ag)O with distributed (Cr, Mn, Cu)O particles. As discussed in chapter 4.1, the reaction layer is composed of (Cr, Mn, Cu)O in the Crofer® 22 H/Ag4Cu/TZ3Y joints in the as-brazed state. This microstructural change of the reaction layer might be explained by the following diffusion process: During annealing, Cr and Mn keep diffusing from the bulk steel to the interface, where reduction of the CuOx by Cr and Mn occurs. The reduced elemental Cu then diffuses into the braze matrix and is oxidized again by dissolved oxygen, forming the (Cr,Mn,Cu)O precipitates observed within the upper layer of the reaction zone. It should be noticed, that Ag diffuses through the (Cr,Mn)O reaction layer to the steel surface without any chemical reaction with Cr or Mn. This observation suggests, that the reaction between Ag and (Cr,Mn)O might only be possible in the presence of free oxygen, what corresponds to the reaction equations described previously (chapter 4.2.1: pure Ag joints section) for the reaction between Ag and Cr-oxides.



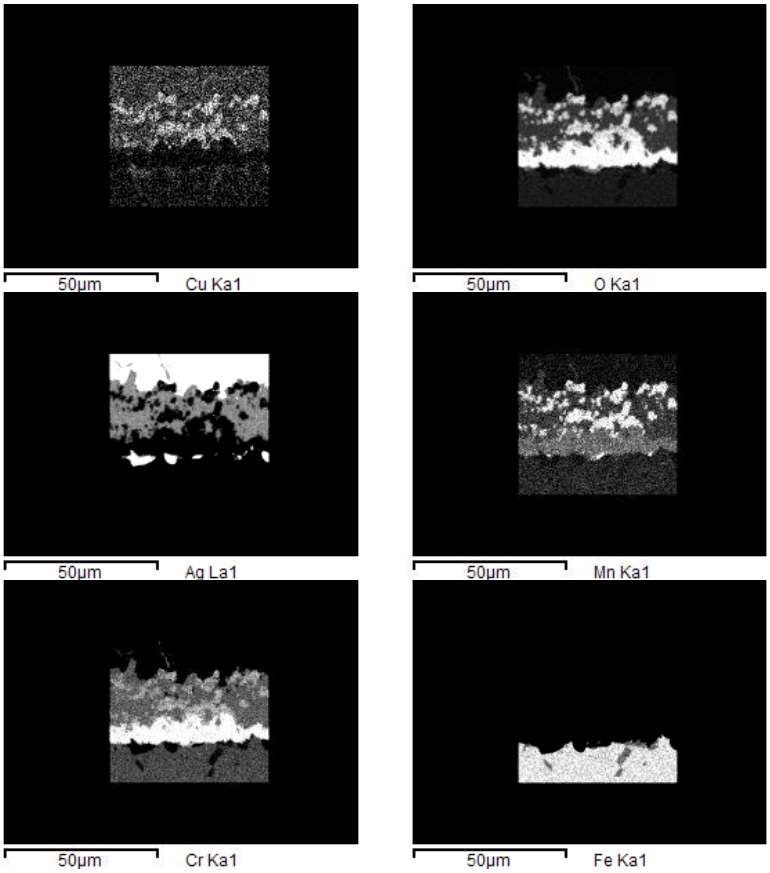


Fig. 4.19 Element mappings of the reaction layer at the braze/steel interface of Crofer® 22 H/Ag4Cu/TZ3Y joints after 3000 hours of annealing in air at 800 ℃

- **Ag0.5Al joints**

Corresponding to pure Ag and Ag4Cu joints, the braze/steel interface remained the weakest link in Ag0.5Al joints after air annealing. The "needle" shaped precipitates, observed in the braze matrix of the Ag0.5Al in the as-brazed state, remain unchanged after annealing. Microstructural analysis reveals the chemical composition of the reaction layer to be similar to that of pure Ag joints (Fig. 4.20). No Al is found in the reaction layer.

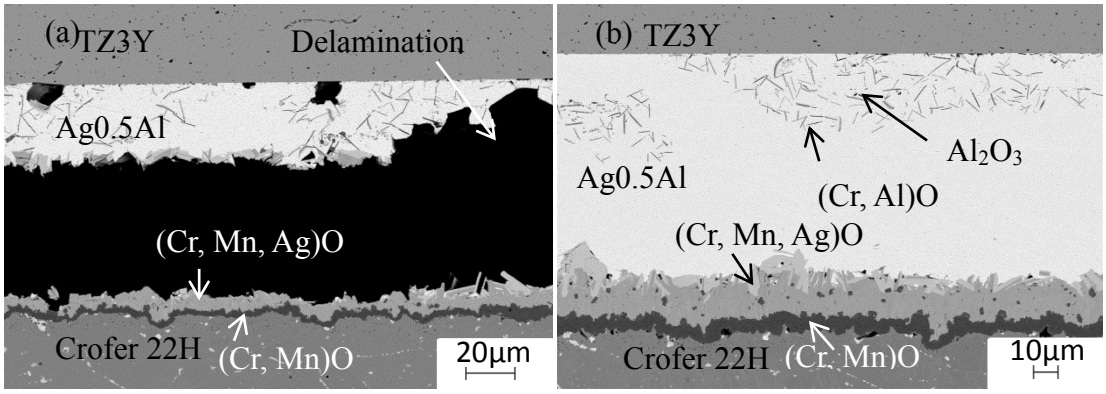


Fig. 4.20 Delamination crack and microstructure of Ag0.5Al joints after annealing in air for (a) 1500 hours and (b) 3000 hours

For all brazes, the thickness of the reaction layer grows with increasing annealing time in air, as shown in Tab. 4.1. Since delamination mainly propagates through the brittle reaction layer for all air annealed joints and in the as-brazed state, the increase of brittle reaction layer volume is considered to be one of the main factors for the decrease in joint strength. On the other hand, considering the fracture energy changes of the three brazes with annealing time, it can be concluded, that the volume of the reaction layer is not the only determining factor for joint strength. The fracture toughness of the chemically differing reaction layers would be another important factor for joint strength and needs detailed investigation.

Tab. 4.1 Thickness of the reaction layer after annealing in air

Thickness of the reaction layer	**As-brazed**	**500 h**	**1500 h**	**3000 h**
Pure Ag	1.5µm	15µm	25µm	25µm
Ag4Cu	5µm	15µm	20µm	25µm
Ag0.5Al	1.5µm	5µm	20µm	25µm

4.2.2 Aging in reducing atmosphere (Ar4Vol%H_2)

Fig. 4.21 shows the change of fracture energies of the three brazes after annealing in reducing atmosphere. Opposite to aging in air, pure Ag joints exhibit the highest aging resistance of the three brazes. With alloying of Cu or Al to the pure Ag braze, the aging resistance in reducing atmosphere drops. Cu-containing joints are sensitive to reducing atmosphere, because of its easy reducibility by hydrogen (oxygen activity: H > Cu). During annealing, the CuOx species are reduced by hydrogen, with elemental Cu dissolving into the braze matrix

and forming pores filled with H_2O (g). As Al has higher oxygen affinity than hydrogen, the drastic decrease in fracture energy of Ag0.5Al joints is unexpected and the underlying mechanism is still under investigation. Microstructures of the brazes after aging in reducing atmosphere are shown and discussed below.

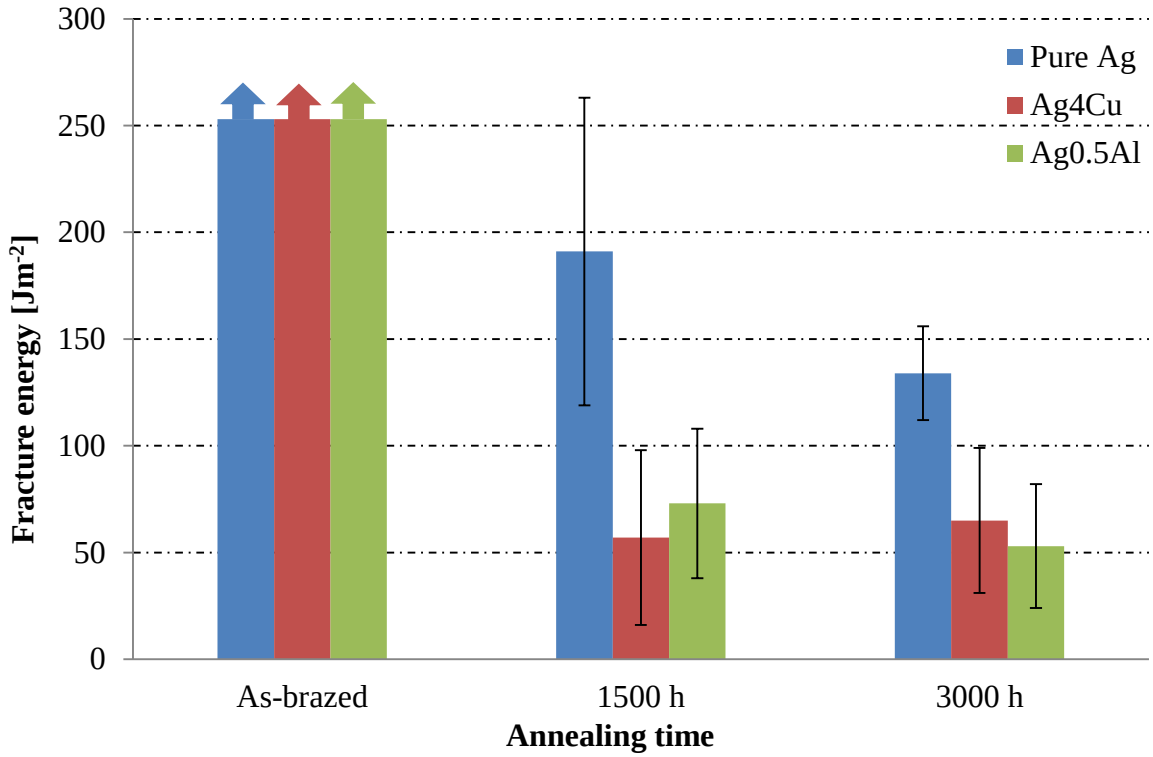


Fig. 4.21 Fracture energies of the three brazes (pure Ag, Ag4Cu, Ag0.5Al) after annealing in reducing atmosphere (Ar4Vol%H_2) at 800 ℃

- **Pure Ag joints**

The cross-sectional view of a pure Ag joint after 3000 hours of annealing in reducing atmosphere (Ar4Vol%H_2) is shown in Fig. 4.22. Unlike for joints in the as-brazed state or after air annealing, delamination is observed at the braze/ceramic interfaces after annealing in reducing atmosphere.

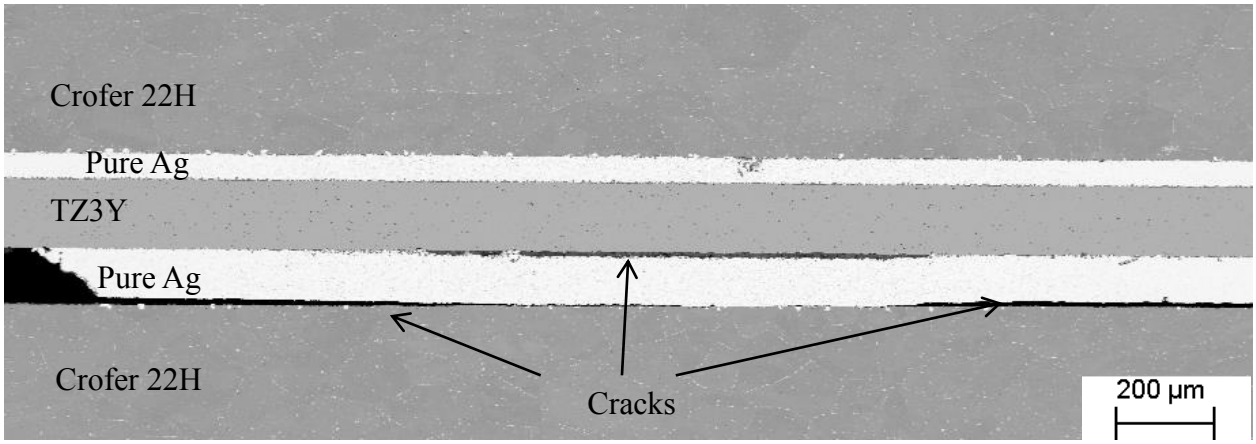


Fig. 4.22 Microstructure of a pure Ag joint after 3000 h of annealing in reducing atmosphere at 800 ℃

Fig. 4.23 shows elemental distributions in the cross-section of a pure Ag joint after 3000 hours of annealing in reducing atmosphere. The reaction layer at the braze/steel interface is still composed of (Cr, Mn)O oxides with a thickness of about 2 µm, which is a little thicker than in the as-brazed state (~1.5µm). Unlike in the air aged state, no (Ag, Cr, Mn)O oxides are found, which further proves the theory discussed in chapter 4.2.1, that sufficient oxygen is necessary for the reaction of Ag with chromium oxides.

On the other hand, (Cr, Mn)O oxides are observed at the braze/ceramic interface and the braze matrix. This phenomenon is probably related to the diffusion of Cr and Mn from the bulk steel into the Ag matrix as well as the redox reaction of the Cr and Mn under reducing atmosphere. During annealing in reducing atmosphere, the interfacial (Cr, Mn)O layer can not be reduced by hydrogen because Cr and Mn have higher oxygen affinity. With increasing amount of Cr and Mn diffusing from the bulk steel to the interface, the free oxygen at the braze/steel interface was consumed by Cr and Mn. Therefore, the Cr and Mn diffused through the matrix and reacted with oxygen at the braze/ceramic interface. As discussed in chapter 2.5.1 and chapter 4.1, oxygen is a very important bonding element at the braze/ceramic interface. With the depletion of free oxygen, the strength of the braze/ceramic interface was degraded. This explains why delamination was observed at both interfaces. Furthermore, lots of Ag-isles can be observed in the steel, beneath the reaction layer. This phenomenon corresponds to the increased formation of (Cr,Mn)O at the braze/ceramic interface, where Cr and Mn diffuse from the steel and Ag diffuses into the voids.

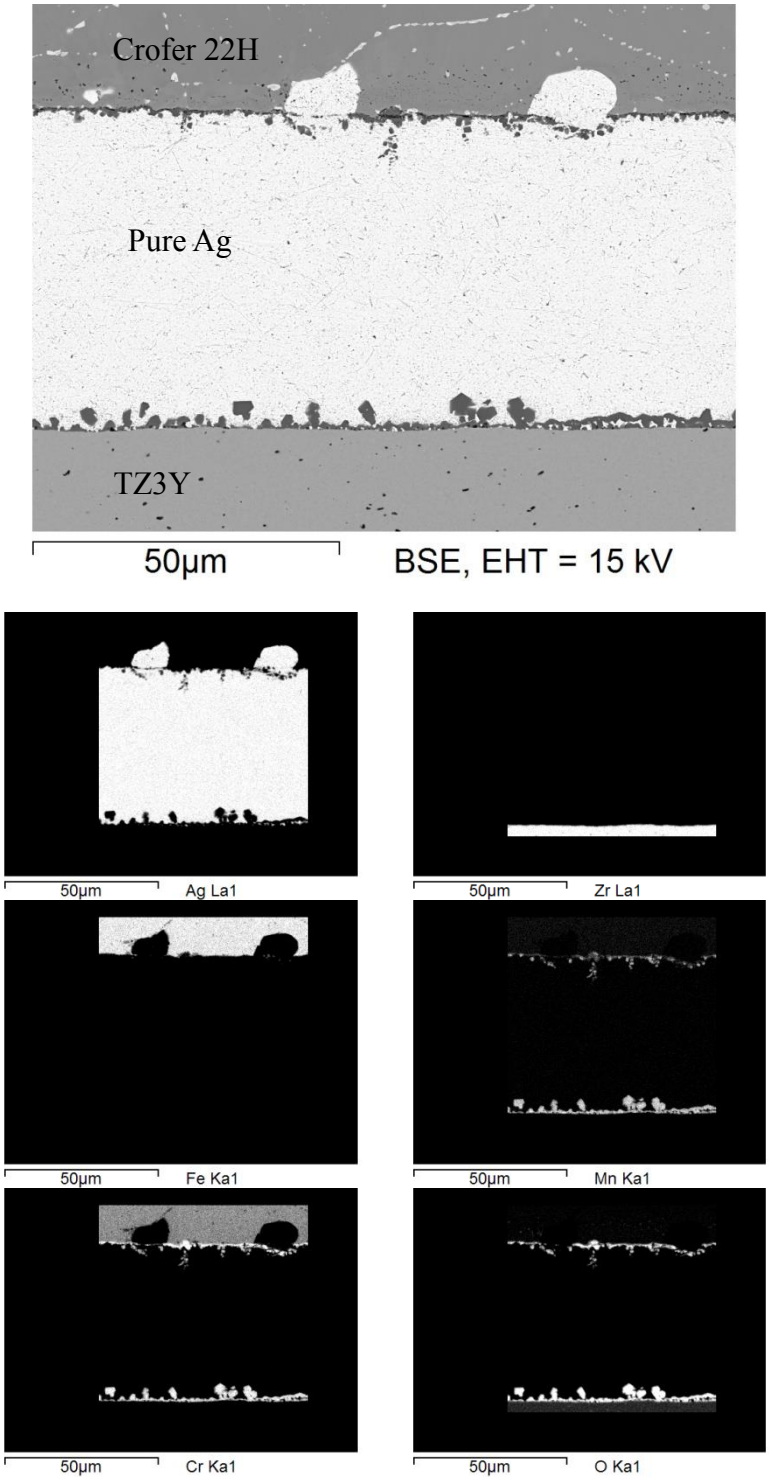


Fig. 4.23 Element mapping of the cross-section of a pure Ag joint after 3000 h of annealing in reducing atmosphere at 800 ℃

- **Ag4Cu joints**

Like in pure Ag joints, a single (Cr, Mn)O layer is observed at both interfaces of the Ag4Cu joints after annealing in reducing atmosphere (Fig. 4.24). Cu- or Cu-mixed oxides are neither detected throughout the braze matrix, nor at the interfaces. In contrast, elemental Cu was

observed to be dissolved all over the Ag matrix, which indicates a complete reduction of CuO_x and Cu-mixed oxides (reaction products from the brazing process).

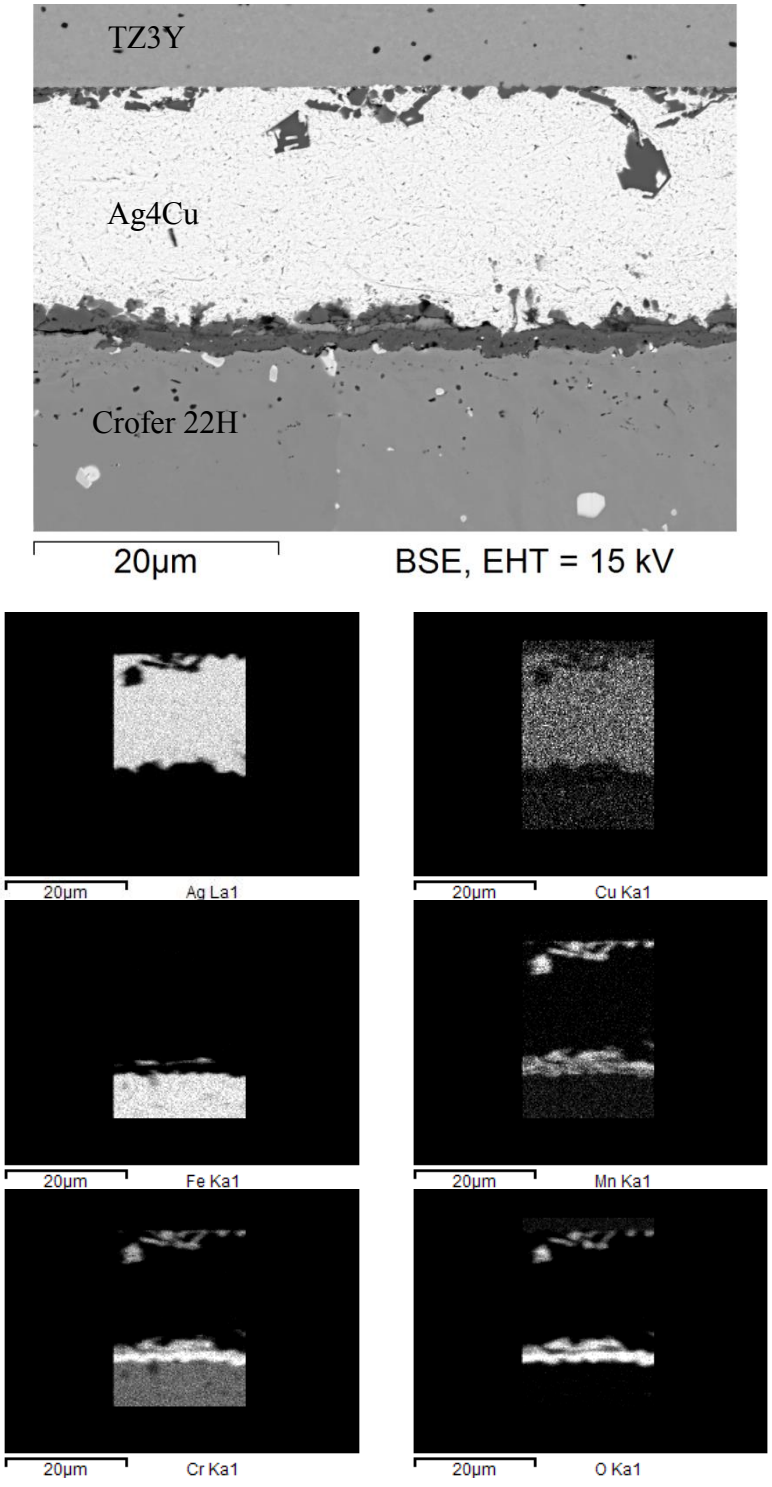


Fig. 4.24 Element mapping of the cross-section of a Ag4Cu joint after 3000 h of annealing in reducing atmosphere at 800 ℃

A comparison of the braze/steel interfaces of Ag4Cu and pure Ag joints unveils, that the (Cr, Mn)O layer formed in Ag4Cu joints is thicker than the one formed in pure Ag joints (Fig. 4.25). Moreover, the interfacial layer seems to display higher porosity in the case of Ag4Cu joints. By comparing with the as-brazed state, it becomes obvious that the porous structure of the Ag4Cu joints is induced by reduction of the Cu oxides, that formed in the original (Cr, Mn, Cu)O layer during brazing. During annealing, CuO_x was reduced and elemental Cu diffused into the braze matrix, leaving pores in the reaction layer. This thicker and more porous reaction layer is believed to be the main reason for the lower aging resistance of Ag4Cu joints in reducing atmosphere.

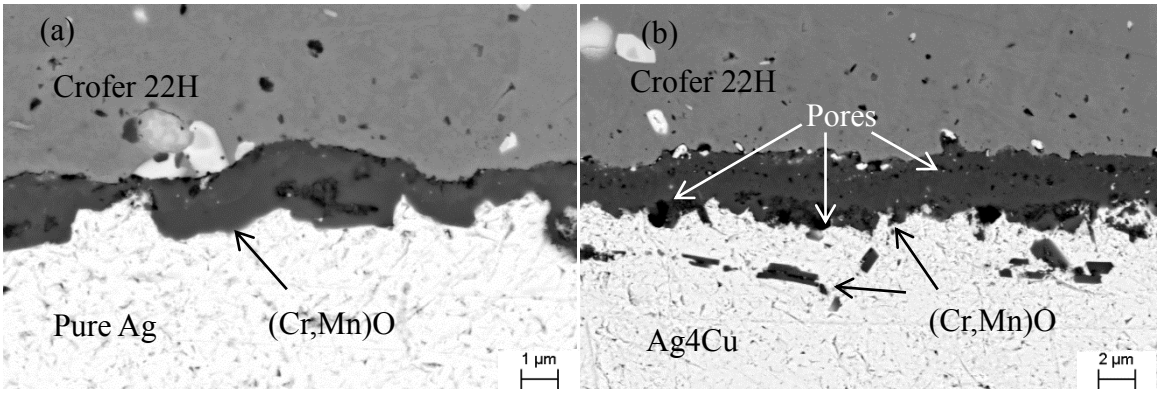


Fig. 4.25 Comparison of the reaction layer at the braze/steel interface after 1500 h of annealing in reducing atmosphere at 800 ℃: a) pure Ag braze; b) Ag4Cu braze

- **Ag0.5Al joints**

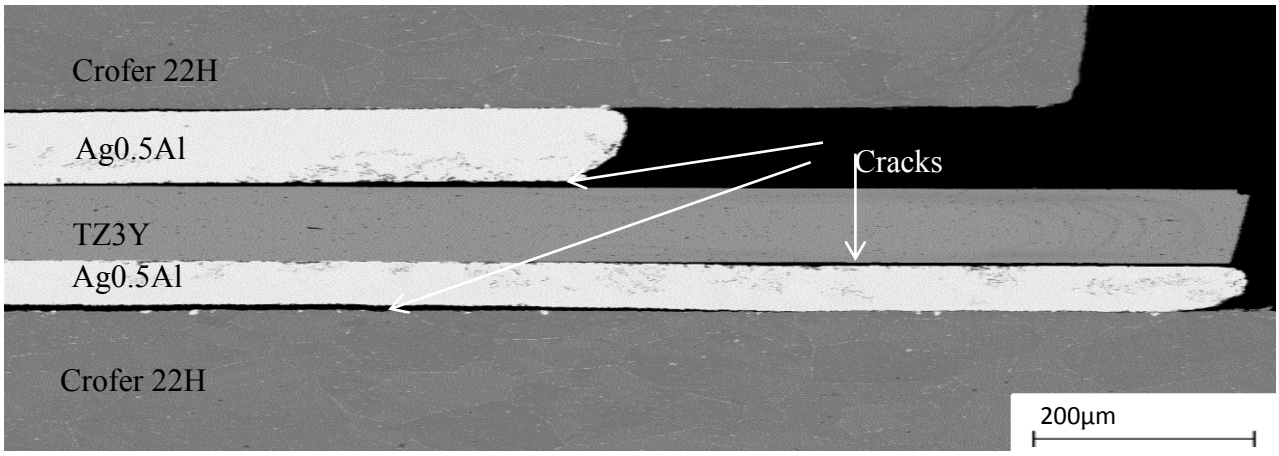
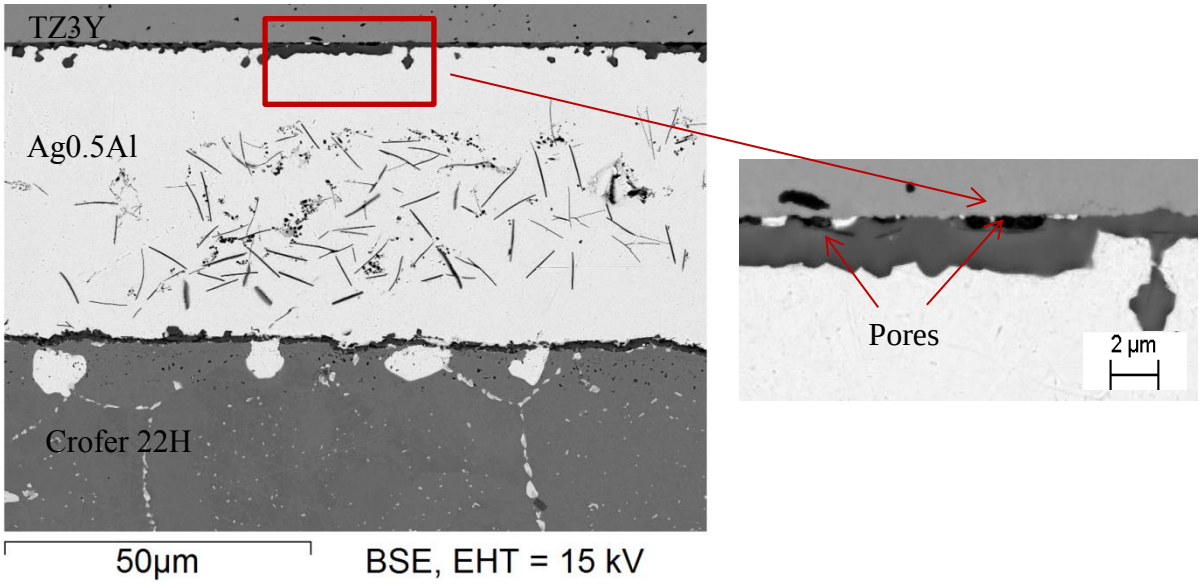


Fig. 4.26 Cross-sectional view of an Ag0.5Al joint after 1500 hours annealing in reducing atmosphere at 800 ℃ (fractured during ambient temperature delamination testing)

Fig. 4.26 shows the fracture morphology of an Ag0.5Al joint after 1500 hours of annealing in reducing atmosphere. Similar to the other braze variants, both the braze/steel interface and the braze/ceramic interface changed during high temperature annealing. Microstructural analysis shows that Ag0.5Al joints exhibit aging effects similar to the other two braze formulations. A (Cr, Mn)O layer forms at the ceramic interfaces (Fig. 4.27). The (Cr, Al)O precipitates observed in the as-brazed state remain unchanged during annealing. In Fig. 4.26, it can be observed, that the braze/ceramic interface is no longer intact. Lots of pores can be observed at the braze/ceramic interface, indicating degraded adhesion at the interface. From the microstructure analysis, the reasons for the lower aging resistance of Ag0.5Al joints in direct comparison to pure Ag joints remain undiscovered. Further investigation is needed to understand the underlying mechanism.



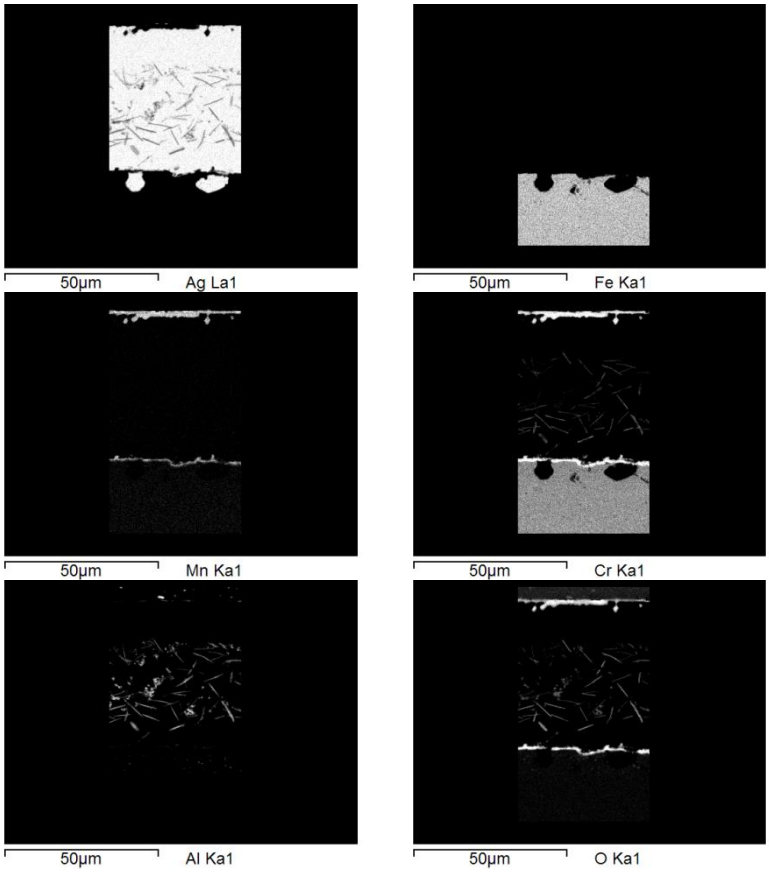


Fig. 4.27 Element mapping of a Ag0.5Al joint after 3000 hours of annealing in reducing atmosphere (Ar4Vol%H_2) at 800 ℃

4.2.3 Discussion and conclusions

Aging in air causes degradation of the joint strength, because of microstructural changes (including volume and chemical composition change) of the reaction zone at the braze/steel interface. A duplex reaction layer was observed after air annealing, which represents the mechanically weakest link of all brazed joints. Air aging mainly induces degradation of the braze/steel interface. With alloying of Cu/Al into the pure Ag braze, the aging resistance of the joints in air is enhanced.

On the other hand, both braze/ceramic and braze/steel interfaces degrade during aging in reducing atmosphere for all the joining variants. Degradation of the braze/ceramic interface could be probably explained by the depletion of the bonding medium (oxygen) at the interface by the formation of reaction products ((Cr, Mn)O) at the interface. Opposite to air aging, alloying of Cu/Al into the pure Ag braze further diminishes aging resistance in reducing atmosphere, regardless of the element's oxidation activity.

For a detailed model of the degradation mechanisms the various interactions of the elements (Cr, Mn, Fe, Ag, Cu, Al, Y, Zr,..) in the presence/absence of oxygen have to be studied.

4.3 High temperature mechanical behavior

The shear strength and creep resistance of the brazed joints were tested in the double shear configuration (cf. chapter 3.5). The mechanical experiments were followed by SEM investigation of the deformed specimens to characterize the influence of microstructure on the mechanical behavior. Furthermore, the properties of the joints after simulated operation were characterized after annealing for 500 h at 800 ℃ in air. The mechanical behavior at high temperature and microstructural features of the as-brazed and the annealed specimens were compared with the focus on operation related changes.

4.3.1 Constant deformation rate tests (CDRT)

- **As-brazed state**

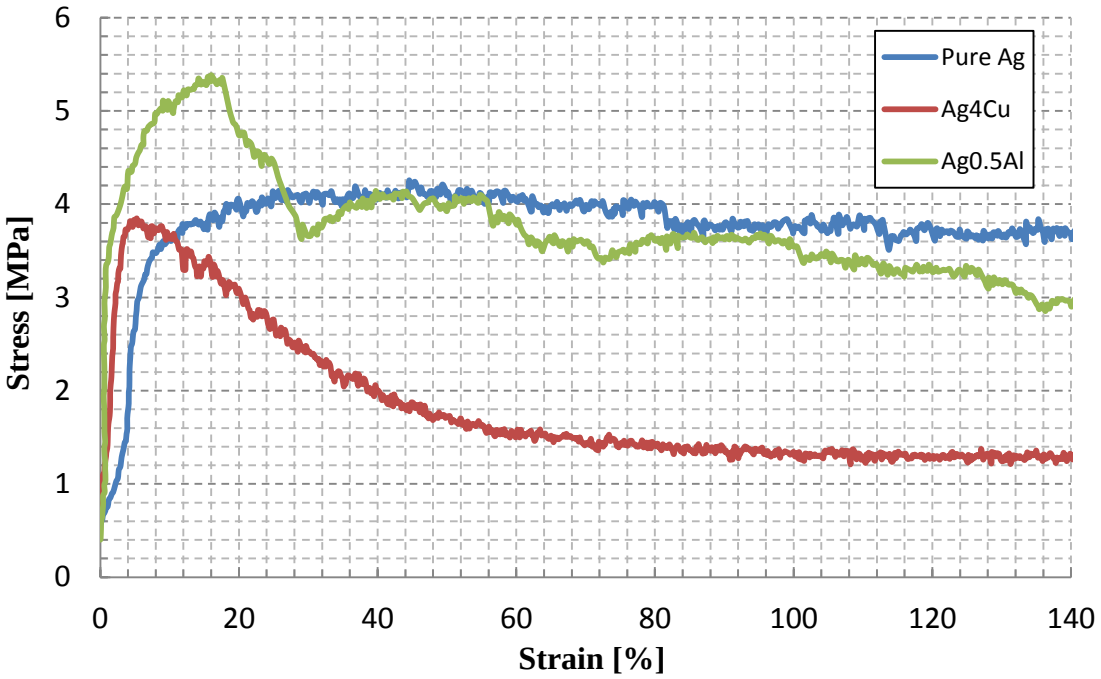


Fig. 4.28 Stress-strain curves of as-brazed pure Ag-, Ag4Cu- and Ag0.5Al-joints at 800 ℃ (air)

Fig. 4.28 shows the stress-strain curves of as-brazed pure Ag-, Ag4Cu- and Ag0.5Al-joints recorded in constant deformation rate tests at 800 ℃. The Ag0.5Al joint displays the highest shear strength, while pure Ag and Ag4Cu joints exhibit lower - but comparable – maximum

shear resistance. Interestingly, pure Ag exhibits a distinctly different curve shape than the other two joining variants: After reaching the maximum shear strength, the stress of the pure Ag joint remains more or less constant for a wide range of strain (up to ~ 80 %), while both the Ag0.5Al and the Ag4Cu joints exhibit a comparatively rapid decrease after reaching the maximum strength level. The curve shapes, differing from each other, indicate deviating deformation and failure behavior.

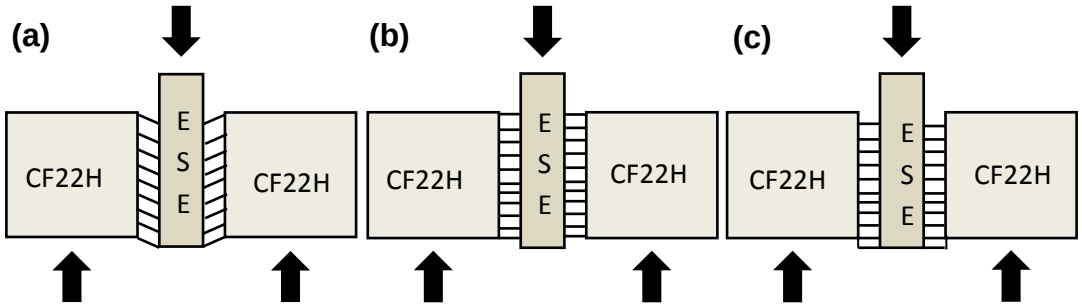


Fig. 4.29 Schematic sketch of possible mechanisms of shear deformation of the joints in double shear specimens: a) braze deformation, b) delamination at the braze/ceramic interfaces, and c) delamination at the braze/steel interfaces

Fig. 4.29 shows cross-sectional schematic views of double shear specimens to illustrate the three main mechanisms of deformation: Deformation of the braze matrix (Fig. 4.29a), delamination at the braze/ceramic interface (Fig. 4.29b) and delamination at the braze/steel interface (Fig. 4.29c). Ideally, only one of the three mechanisms would be effective. In reality the outlined mechanisms do compete to different extents, correlating to the strength level of the respective deformation site.

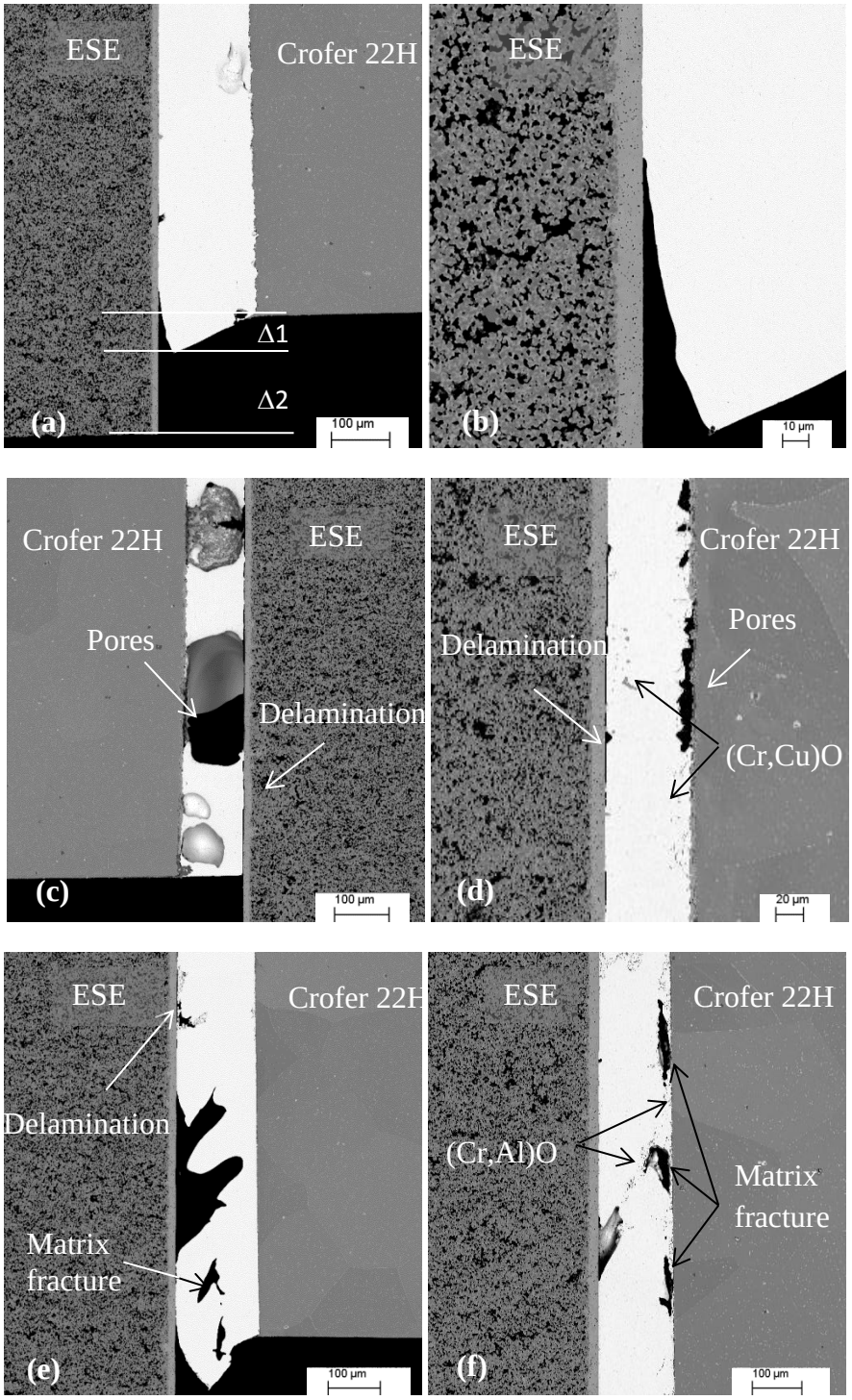


Fig. 4.30 Cross-sectional views of a pure Ag joint (a, b), an Ag4Cu joint (c, d) and an Ag0.5Al joint (e, f) after shear testing at 800 ℃

Fig. 4.30 shows the microstructures of pure Ag, Ag4Cu, Ag0.5Al joints after constant deformation rate tests at 800 ℃. By comparing the cross-sectional views to the previously discussed idealized deformation mechanisms, it may be stated that the braze/ceramic interface and the braze matrix are the weakest links of pure Ag and Ag0.5Al joints, while the

braze/ceramic interface represents the weakest link in case of Ag4Cu joints. There are notable differences in the deformation and failure patterns of the joints: In case of the pure Ag joint (cf. Fig. 4.30a) Δ1 approximately represents the plastic shear deformation of the matrix and correlates to about 50 % of the joint height. Consequently the braze/ceramic interface remained intact up to approximately 50 % of bulk matrix deformation, which correlates well with the strain at maximum strength (at ~ 50 % strain, cf. Fig. 4.28). Most likely peeling of the matrix from the ceramic at the bottom face of the joint, leading to the bulged shape of the Δ1 proportion (cf. Fig. 4.30b: volume constraint of the braze in between the steel block and the ESE was lost, because of interface slip), was induced during plastic deformation of the matrix. After reaching the maximum stress the matrix obviously delaminated from the ceramic faying surface and further deformation (represented by Δ2, cf. Fig. 4.30a) was mostly accomplished by slip at the braze/ceramic interface. Δ1+Δ2 correlate well with the maximum amount of deformation reached in the experiment, which underlines the validity of the proposed mechanisms. Note that the highly deformation tolerant behavior of the pure Ag joint is visible in the shear curve, too: While stress increases quite steeply in case of the Ag4Cu joint (deformation up to delamination: ~ 5 %), the pure Ag joint exhibits a rather smooth transition up to delamination (at ~ 50 % strain). Contrary to pure Ag, the Ag4Cu joints do not show visible plastic deformation of the matrix (Fig. 4.30c). A possible reason for this might be, that small copper and chromium containing mixed oxide particles stiffen the matrix of the Ag4Cu joint (cf. Fig. 4.30d). A stiffer matrix dissipates less energy by plastic deformation. Therefore energy is directly transferred to the interface and thus the interface might crack prematurely in terms of deformation (delamination of the braze/ceramic interface is visible in Fig. 4.30c, d), but at nearly the same fracture stress.

The Ag0.5Al joint again yields a differing deformation / fracture mechanism: It constitutes the stiffest and strongest joint (Fig. 4.28) and exhibits plastic deformability similar to pure Ag joints. It displays pronounced deformation and even partly fracture of the braze matrix during shearing. Presumably the oxide particle morphology, number, distribution and location within the matrix and at the interfaces result in a preferable combination of stiffness and plasticity of the matrix and strength of both the matrix and the interfaces. Like for the other brazes, delamination occurs at the ESE/braze interface (cf. Fig. 4.30e), but additionally delamination of the braze matrix from precipitates ((Cr,Al)O, Al_2O_3) accompanied by matrix fracture also occurs (Fig. 4.30f).

The shear performance of the brazes was also examined at lower temperatures (675 ℃ and 550 ℃). The obtained maximum shear stresses are listed in Tab. 4.2. With decreasing temperature all joints display increasing strength. Opposite to 800 ℃, the Ag4Cu joints are the strongest at 675 ℃ and 550 ℃.

Tab. 4.2 Shear strength in the as-brazed state at different temperatures

Temperature [℃]	Pure Ag	Ag4Cu	Ag0.5Al
800 ℃	4.1 MPa	3.8 MPa	5.3 MPa
675 ℃	8.5 MPa	9.1 MPa	7.1 MPa
550 ℃	13 MPa	14.6 MPa	11.5 MPa

With competing deformation at the braze/steel interface (Fig. 4.31a: Δ1) deformation is not restricted to the braze matrix and the braze/ceramic interface (Fig. 4.31a: Δ2) anymore at lower testing temperatures in case of the Ag0.5Al and the pure Ag joints. Delamination of the braze/steel interface was not observed in Ag4Cu joints. According to chapter 4.1.1, the reaction layers formed at the braze/steel interface have different chemical composition and morphology, according to the braze composition. The differences in interfacial reaction layer chemistry and morphology are plausible reasons for the different change in shear strength with lower testing temperatures. Interestingly, formation of "needle" shaped precipitates close to the reaction layer at the braze/steel interface is found in Ag4Cu joints (Fig. 4.31b), too. These oxide particles are composed of chromium and copper. Compared to 800 ℃ shear samples and air-annealed bending specimens (cf. chapter 4.2.1), the oxide formation seems to be more pronounced in case of the low temperature (675 and 550 ℃) shear specimens. Oxide formation of a comparable extent was exclusively observed in the thermal cycling specimens, discussed in chapter 4.4.1. Preferable formation of these particles at lower temperature might be considered to be another possible reason for the enhanced shear resistance of the Ag4Cu joints. Possibly the (Cu, Cr)O are not stable in long term 800 ℃ operation condition. Detailed examination of microstructural change and correlation to enhanced strength should be one focus of future work.

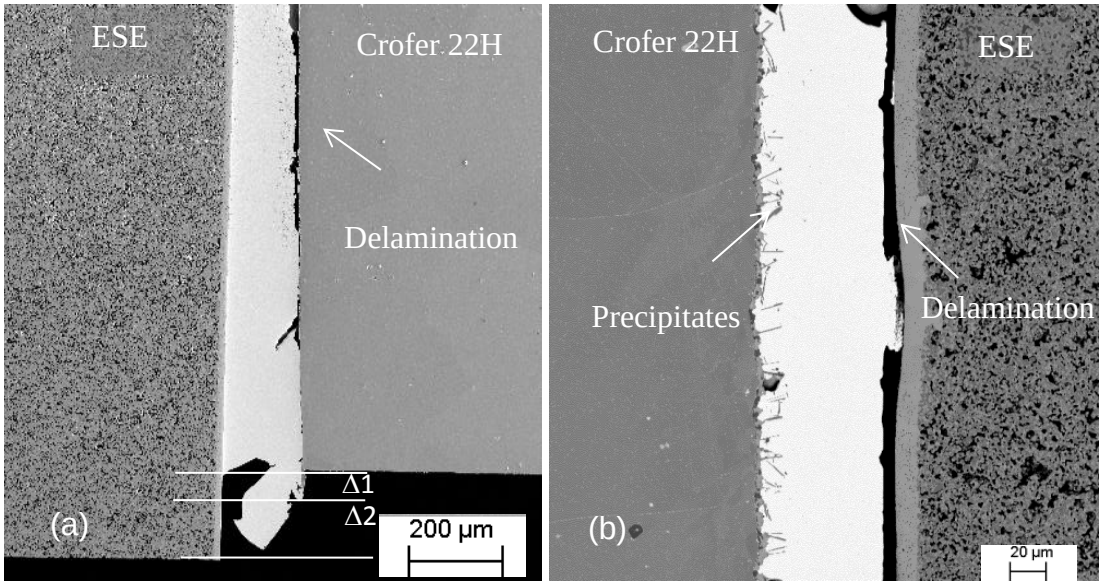


Fig. 4.31 Cross-sectional views of a Ag0.5Al (a) and a Ag4Cu joint (b) after shear testing at 550 ℃

- **Influence of aging**

To study the shear behavior of the joints after long term operation, aging experiments (800 ℃, 500 h, air) were conducted prior to shear testing. The shear strength values in the as-brazed and the aged state are summarized in Tab. 4.3. Compared to the as-brazed state, aging in air increases the shear strength of all the braze variants and equals out the differences in the maximum obtainable values. Unlike in the as-brazed state, fracture of the braze matrix - accompanied by delamination at the braze/ceramic interface - is observed for all investigated brazes. Fig. 4.32 exemplarily shows the failure pattern of an Ag4Cu joint.

Tab. 4.3 Shear strength in the as-brazed state and after aging

Specimen state	Pure Ag	Ag4Cu	Ag0.5Al
as-brazed	4.1 MPa	3.8 MPa	5.3 MPa
aged (800 ℃, 500 h, air)	7.09 MPa	7.2 MPa	7.29 MPa

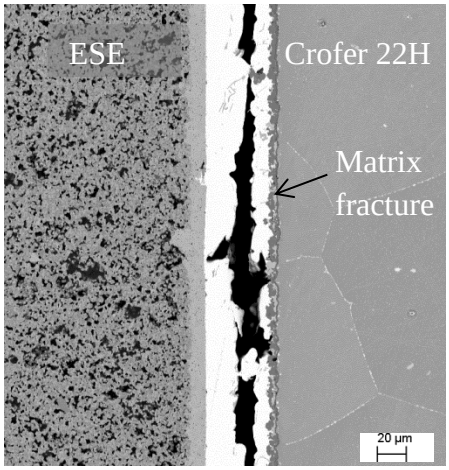


Fig. 4.32 Failure pattern of an aged (800 ℃, 500 h, air) Ag4Cu joint after 800 ℃ shear testing: Fracture of the braze matrix

Combining the changes in mechanical strength and failure mechanisms it can be concluded, that aging in air enhances the delamination resistance of the braze/ceramic interface and the resistance to shear deformation of the braze matrix. Strengthening of the braze/ceramic interface may be attributed to an increase and homogenization of the oxygen bonds at the interface (cf. chapter 2.5.1). Strengthening of the matrix could be obtained by solid solution hardening by oxygen (discussed in chapter 2.6.1) or elements diffusing into the braze matrix from the metallic joining partner.

4.3.2 Stress relaxation

- **As-brazed state**

Fig. 4.33 displays a Norton plot of the three braze variants at 800 ℃. The dashed trend-lines represent the creep rates calculated from the stress relaxation tests, while the closed points (▲, ■, ♦) represent the maximum shear stress and the strain rate obtained from constant deformation rate tests.

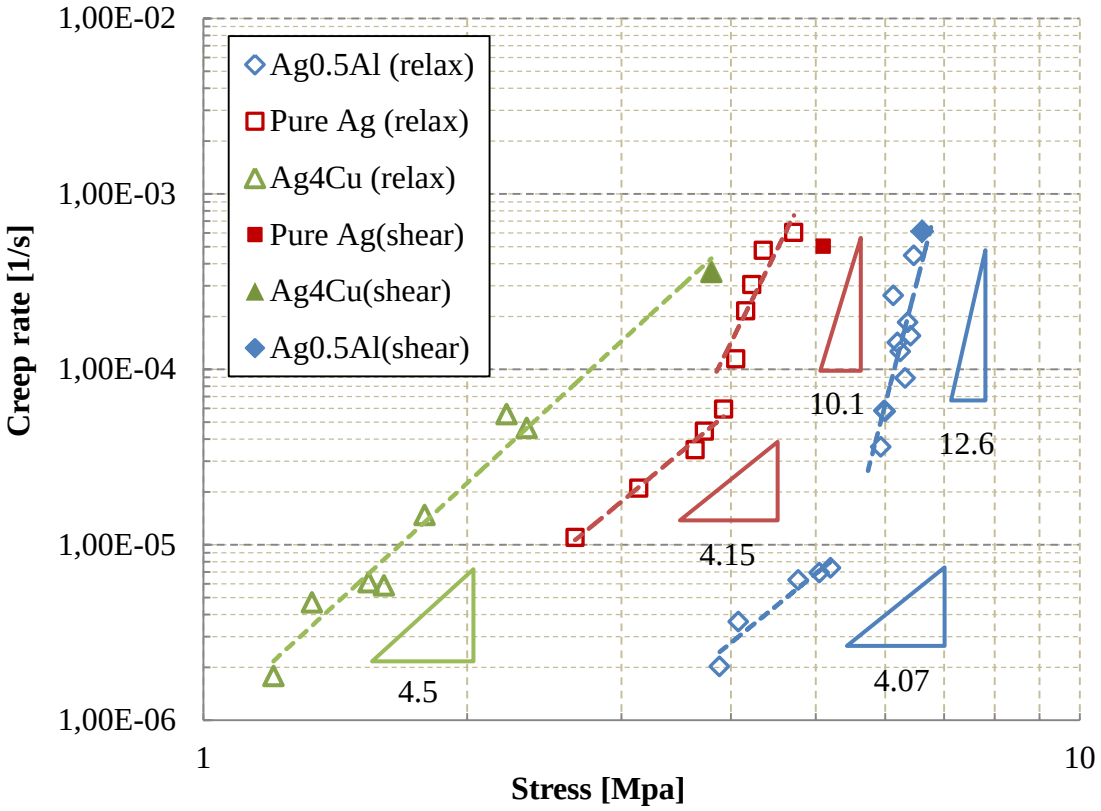


Fig. 4.33 Creep rate vs. stress of the three braze variants (800 ℃)

According to the deformation mechanism map of pure Ag in chapter 2.6.1 (Fig. 2.13), the pure Ag joints range in the power law creep regime. Ag4Cu and Ag0.5Al joints differ slightly from the values given in the map, which is apparently due to alloying. It should be noted, that in case of the pure Ag and the Ag0.5Al joints, the stress dependency of the creep rate (e.g. the slope of the trend lines) splits up into a high and a low stress regime. In the low stress regime both brazes present similar stress exponents ($n \approx 4$). This corresponds well to the value given by Frost and Ashby [Fro82], where a stress exponent of 4.3 is stated for power law creep of pure Ag. At higher stress the pure Ag and the Ag0.5Al joints exhibit a stress exponent around 11. Keeping the testing procedure in mind, a plausible explanation for this result is: The joint is initially loaded with a constant deformation rate of 3 µm/min up to the maximum shear stress level, where the strain was held constant for the stress relaxation process. Therefore no stabilization period was provided between constant rate deformation and stress relaxation and thus the joint still exhibited plastic behavior during relaxation in the initial high stress regime. Consequently, the deformation rates derived in the high stress regime represent plastic behavior rather than creep. Ag0.5Al joints exhibit the highest shear strength and the creep

rates are almost two orders of magnitude lower than that of pure Ag joints in the whole tested stress range.

- **After aging in air**

The same stress relaxation procedure was applied after annealing in air (800 ℃, 500 h). In the as-brazed state Ag0.5Al joint exhibited the highest shear strength and resistance to creep. Apparently the pure Ag and the Ag4Cu joints strengthened during high temperature annealing in air, because they exhibit shear strengths and creep rates similar to that of the Ag0.5Al joints. The Ag0.5Al joints maintain similar shear strength like in the as-brazed state. In the plastic regime (high stress levels, n ≈ 10.7) all three brazes exhibit almost similar stress/deformation rate relations. Interestingly, the pure Ag joints exhibit lower creep rates than the Ag4Cu and Ag0.5Al brazes in the creep regime (low stress levels, n ≈ 4.8).

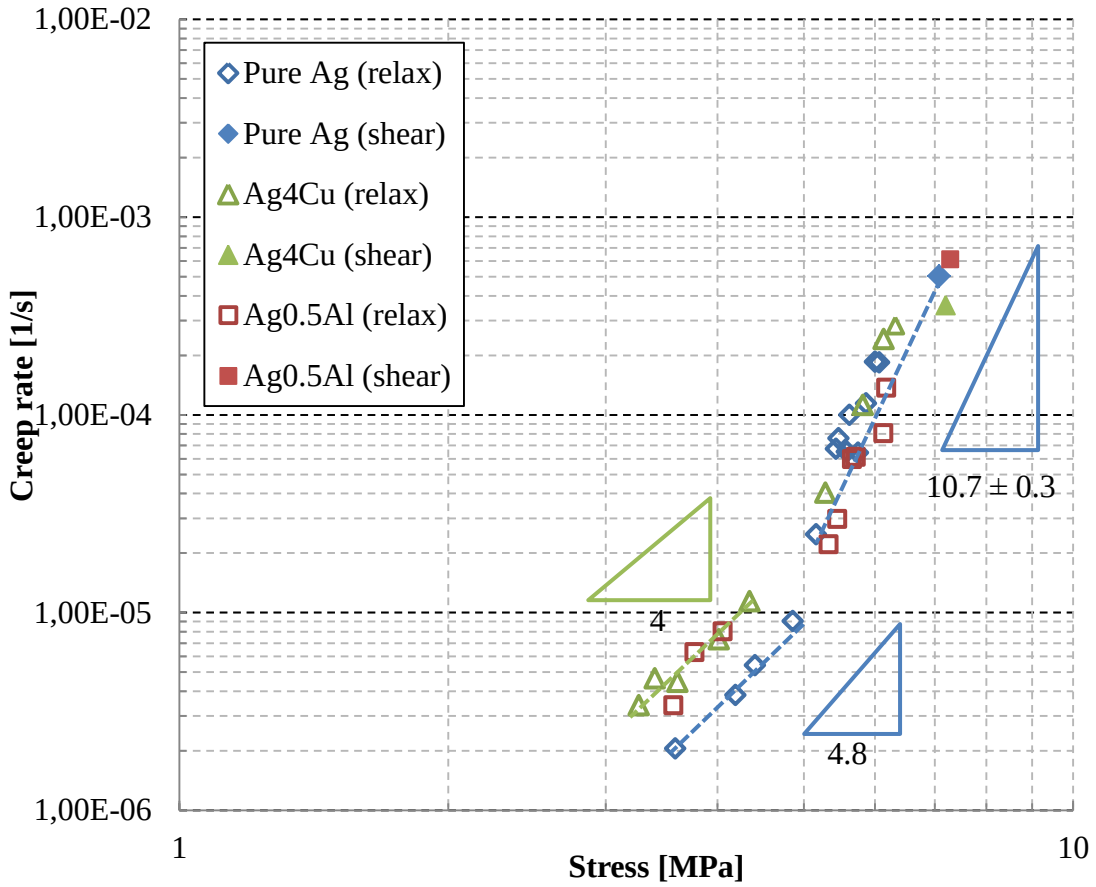


Fig. 4.34 Norton plot of the three brazes after annealing in air for 500 h at 800 ℃

Annealing in air obviously enhances the maximum shear strength by diffusion of oxygen into the braze matrix, leading to strengthening of the interfaces (cf. chapter 2.5.1) and of the

matrix in solid solution. Like the air annealing related change of the stress/creep rate relations demonstrate, the solute effect of oxygen obviously strengthens the matrix against creep deformation, too. Nevertheless, the three braze variants seem to benefit to different extents from this effect. This may be explained by different distribution of oxygen. The Ag0.5Al and the Ag4Cu joints contain oxygen affine elements, which might consume oxygen during annealing in air to form and/or grow oxide precipitates and thereby diminish the amount of dissolute oxygen (solute drag effect). Furthermore, creep at low stress is more sensitive to insufficient/inhomogeneous (in terms of precipitates, which consume oxygen from - and thus leaving solute depleted zones in - the matrix) solute content than to plastic deformation, because diffusion and solute-dislocation interaction are the dominating factors. Because the pure Ag joints are merely free from any precipitates and thus present the highest solute content with the most uniform distribution, the creep strengthening effect of soluted atoms may be more pronounced than in the other brazes.

4.3.3 Conclusions

Unlike the room temperature delamination test, high temperature shear testing involves both interface and matrix performance. The braze matrix governs the plastic deformation behavior at all the tested temperatures, while the maximum strength is determined by the braze/ceramic interface at 800 °C and by both interfaces at lower temperature (≤ 675 °C).

The Ag0.5Al joints exhibited the highest shear and creep resistance at 800 ℃, but with aging in air and decreasing testing temperature its superiority disappears. In contrast to the ambient temperature delamination tests, aging in air increased the high temperature shear resistance of all investigated brazes.

4.4 Interface and matrix performance after thermal cycling

Thermal expansion mismatch is an important issue in multi-layer systems during thermal cycling operation. The temperature profiles during start-up and shut down as well as local heat concentrations induce thermal mismatch stresses into the braze system, which may cause failure of the joint. The resistance of the reactive-air-brazed joints to rapid temperature changes is examined in a benchmark fast thermal cycling test (the testing procedure is outlined in chapter 3.3.2). Assuming a single phase braze matrix (without inclusions like e. g. oxide particles), the thermal mismatch stresses reach the highest values at the interfaces,

where in the special case of reactive-air-brazed joints, brittle oxide layers may be located (at the steel/braze interface in the as-brazed state, at both interfaces after high temperature operation). Therefore, these interfaces are especially prone to fracture during thermal cycling. For the characterization of thermal cycling capability, the joints were tested by ambient temperature delamination test (cf. chapter 3.4) after thermal cycling. With delamination of the interfaces in case of the pure Ag and the Ag4Cu joints and fracture of the braze matrix two differing damage and failure mechanisms are encountered.

4.4.1 Strength degradation caused by interfacial delamination

- **Pure Ag joint**

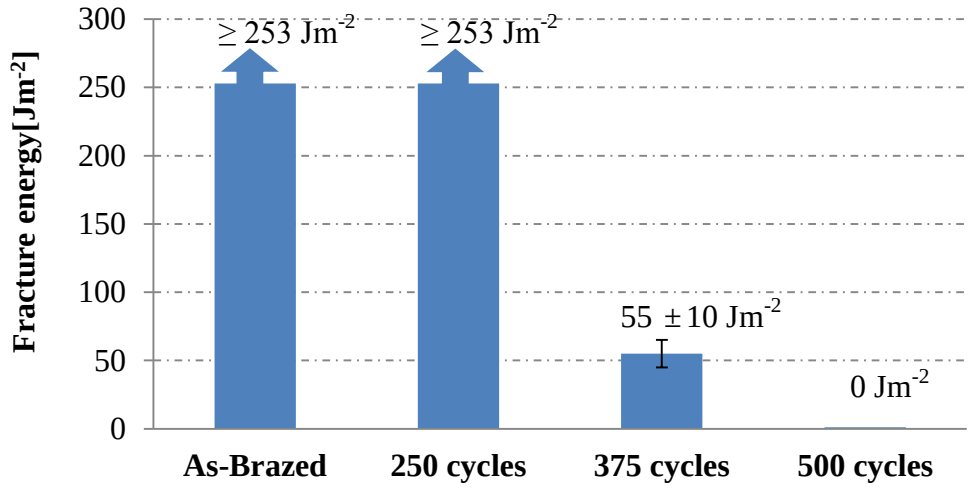


Fig. 4.35 Fracture energy of pure Ag joints with increasing number of thermal cycles

Fig. 4.35 shows the fracture energy of pure Ag joints with increasing number of thermal cycles. The joint strength remains high until 250 cycles. Afterwards the fracture energy starts to decrease from ≥ 253 Jm^{-2} to around 50 Jm^{-2} within the upcoming 125 cycles, adhesion becomes completely lost. After 500 thermal cycles delamination occurs at the braze/ceramic interface (Fig. 4.36). The silver braze entirely detached from the ceramic joining partner during thermal cycling without any additional mechanical loading, leaving a macroscopically clean, braze-free ceramic surface. However, in the SEM small pits can be found in the ceramic surface (cf. chapter 4.1.2), which are probably caused by interaction of the braze and the ceramic during brazing.



Fig. 4.36 Detached specimen after 500 thermal cycles (without additional delamination testing)

Degradation of the braze/ceramic interface can already be observed after 250 thermal cycles (from cross-sectional views of the joints, cf. Fig. 4.37). The microstructure reveals, that delamination in ambient temperature delamination testing occurred at both interfaces after 250 thermal cycles. A serrated braze surface morphology can be observed at the delaminated braze/ceramic interface (red circle, Fig. 4.37(a)). Even at intact sites of the braze/ceramic interface (Fig. 4.37b) discontinuous adhesion is observed, which is probably caused by cyclic plasticization of the braze matrix. A microscopic explanation for this phenomenon might be the breakup of oxygen bonds at the braze/ceramic interface to compensate for the displacement between braze matrix and joining partner during cycling. The distance between the braze and the ceramic surface, induced by plastic deformation prevents the recombination of the oxygen bond, leaving discontinuous adhesion at the braze/ceramic interface. With accumulated thermo-cyclic deformation adherence is finally lost at the braze/ceramic interface after 500 thermal cycles.

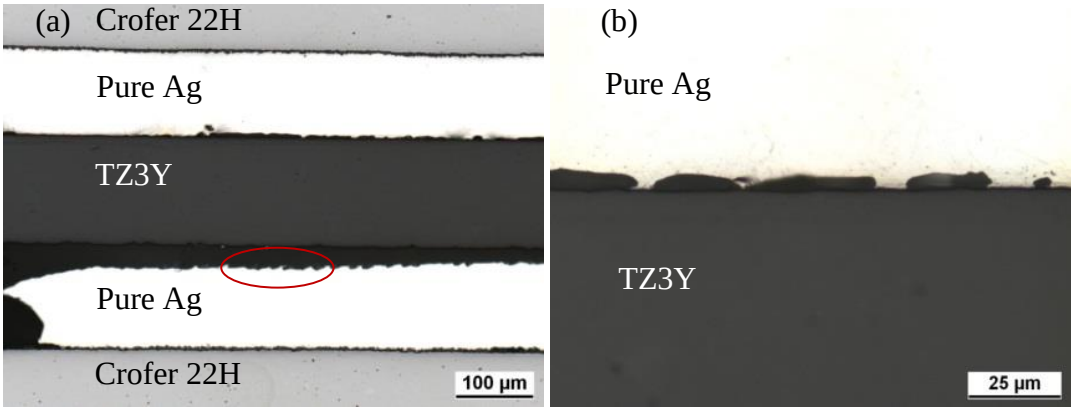


Fig. 4.37 Delamination of pure Ag joints after 250 rapid thermal cycles

- **Ag4Cu joints**

Compared to pure Ag joints, Ag4Cu joints exhibit less thermal cycling resistance (Fig. 4.38). The fracture energy of the joints starts to decrease after 50 thermal cycles and all the joints fail within 250 cycles. Like in the case of the pure Ag joints, all the Ag4Cu joints delaminate at the braze/ceramic interface.

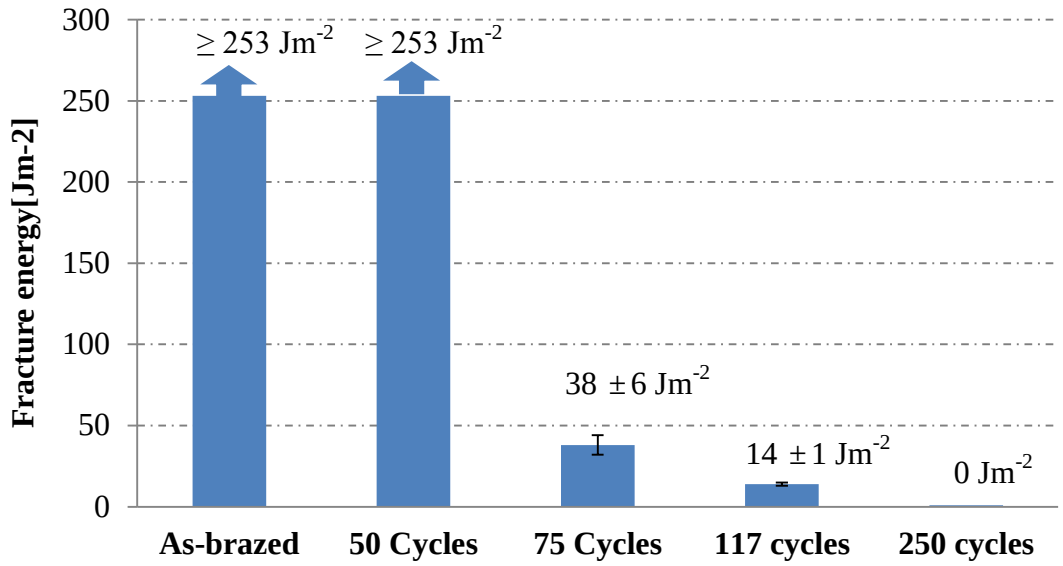


Fig. 4.38 Fracture energy of Ag4Cu joints with increasing number of thermal cycles

The braze matrix reveals the same serrated surface morphology after delamination from the ceramic joining partner as the pure Ag joints (Fig. 4.39). Furthermore strip-like (Cr,Cu)O precipitates are observed within the braze matrix, which formed during thermal cycling (cf. Fig. 4.4 where the as-brazed microstructure free of such particles). Solely assessed by comparing the damage patterns, no big differences are observed between the Ag4Cu and the pure Ag braze. For this reason the difference in thermal cycling performance cannot be explained by interfacial properties alone and must be linked to the mechanisms of stress accommodation and redistribution in the braze matrix during rapid thermal cycling (cf. chapters 4.4.3 and 4.4.4).

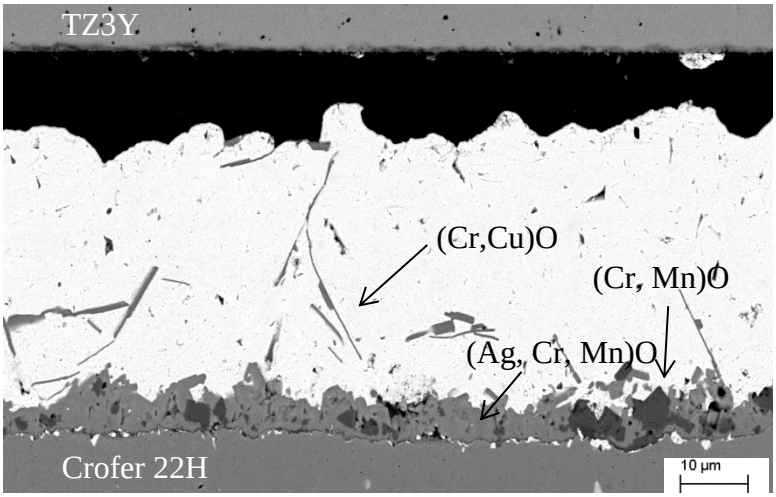


Fig. 4.39 Delaminated Ag4Cu joint after 50 thermal cycles (after ambient temperature delamination testing)

4.4.2 Strength degradation caused by braze matrix deformation

Ag0.5Al joints behave in a different way: This braze variant reached 4825 cycles without obvious peeling from the ceramic joining partner and thus exhibits by far the highest thermal cycling resistance. Nevertheless, the joint hardly maintains any strength after 4825 cycles and can easily be broken by hand, when taken from the thermal cycling set-up. Interestingly fracture occurs within the braze matrix and residues of the Ag matrix can still be observed adhering to both the ceramic and the metallic joining partners after delamination. Fig. 4.40 displays the cross-sectional microstructure after 4825 cycles. Ambient temperature delamination tests indicate, that the fracture energy of the Ag0.5Al joint is still higher than the measuring limit ($\geqslant$ 253 Jm^{-2}) after 2000 cycles. During thermal cycling discharge of the braze matrix out of the joining regime was observed (Fig. 4.41) and the overlapping braze exhibits a wavy curvature (marked by the red line). This phenomenon may be attributed to the accumulation of cyclic plastic deformation during thermal cycling.

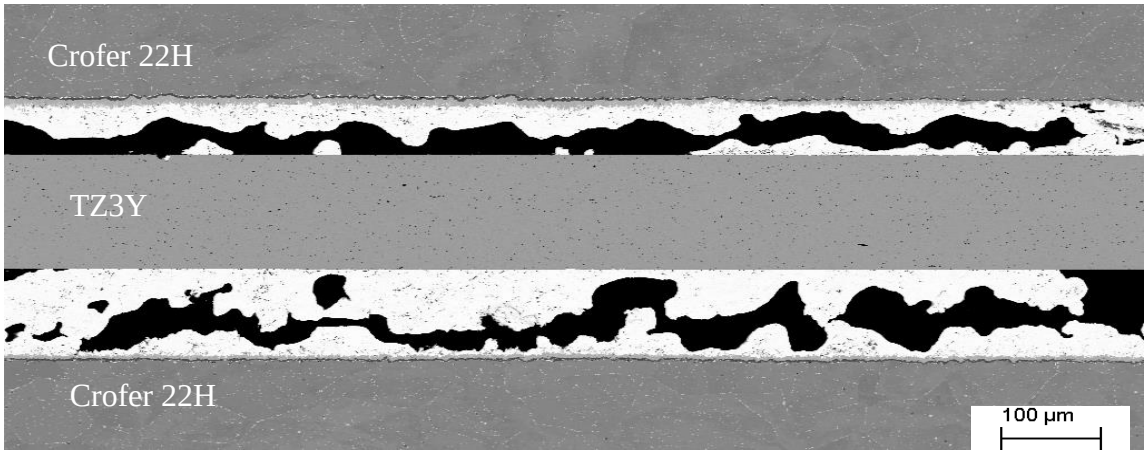


Fig. 4.40 Cross-sectional view of an Ag0.5Al joint after 4825 thermal cycles

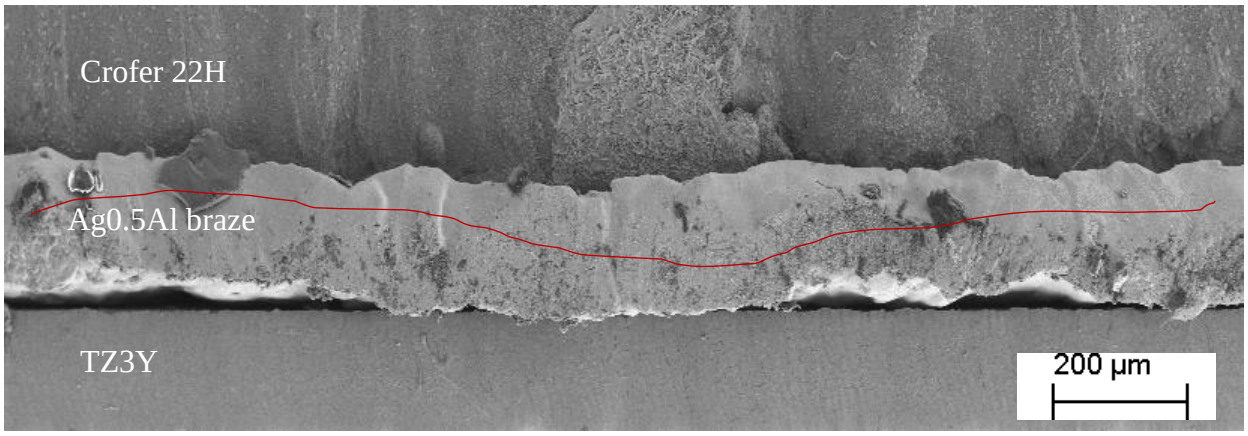


Fig. 4.41 Curved braze matrix overlapping the joining partners after 1000 thermal cycles

4.4.3 Stress accommodation and redistribution during thermal cycling

According to the thermal expansion coefficients (TEC: α) of the braze matrix and the joining partners, the relative deformation strain rate at the respective interface can be calculated according to the temperature change during thermal cycling by:

$$\dot{\gamma} = \left[\left(\alpha_{Ag}(T(t)) - \alpha_{ceramic/steel}(T(t))\right) \times (T(t) - T_0)\right]/dt$$

$\alpha_{Ag}(T(t))$ and $\alpha_{ceramic/steel}(T(t))$ denote the thermal expansion coefficients of the braze and the respective joining partners at the temperature T(t). T_0 is the temperature at which the thermal mismatch stress at the braze interfaces equals to 0 (in the as-brazed state the solidification temperature of the braze, in long-term isothermal high temperature operation

the operation temperature). T(t) is the temperature of the joint at which the deformation rate is calculated. In this work, the solidification temperature of the pure Ag in air (951 ℃) during brazing is taken for T_0 where the interfacial stress free state is assumed to occur. The temperature history of the specimen was recorded during thermal cycling (temperature-time) and thus the strain rates the braze matrix at the interfaces can be derived. Fig. 4.42 and Fig. 4.43 display the strain rates in the braze matrix at both interfaces (braze/ceramic and braze/steel interface) as a function of the specimen temperature.

During heating, the maximum strain rate is in the order of magnitude of $10^{-3}s^{-1}$ at around 220 ℃. Towards increasing temperature the strain rate decreases and reaches the lowest value in the $10^{-7}s^{-1}$ range at the maximum temperature of the cycle (800 ℃). During cooling, the maximum strain rate in the range of $10^{-4}s^{-1}$ appears at around 750 ℃, while the lowest value of $10^{-8}s^{-1}$ is reached between 130 ℃ and 150 ℃. It has to be noted, that during the thermal cycling tests, the specimen temperature varies from 200 ℃ to 800 ℃ and only the first and the last cycle of the given interruption interval (250, 375, 500 cycles in case of the pure Ag joints; 50, 75, 117, 250 cycles in case of the Ag4Cu joints; 1000, 2000, 4825 cycles in case of the Ag0.5Al joints) were ambient temperature cycles. In the calculated temperature regime, the strain rate at the braze/ceramic interface is mostly lower than that at the braze/steel interface, either during heating or cooling. This means that also the thermal mismatch stress at the braze/ceramic interface is lower than that at the braze/steel interface.

Supposing the interfaces are mechanically stable (without interface sliding) during thermal cycling, the braze matrix at the ceramic interface has to deform by an absolute strain of about 0.006 ($\left(\alpha_{Ag}(T(t)) - \alpha_{ceramic/steel}(T(t))\right) \times (T(t) - T_0)$) to compensate for the thermal mismatches in the temperature range of 200 – 800 ℃. This value exceeds the elastic limit of pure silver (0.2 %), which means that plastic deformation has to take place during thermal cycling. Usually plastic deformation can appear in three different ways: Crystallographic slip, mechanical twinning and diffusion [Got04]. In case of slow temperature change during thermal cycling (i.e. up to several hours or even days for one cycle) the thermal mismatch stresses are mainly to be compensated by diffusion controlled creep of the braze matrix. However, in case of rapid thermal cycling (like shown in Fig. 4.42) the deformation rate at certain temperatures may reach values of $10^{-3}s^{-1}$, which is far beyond the creep regime. Diffusion controlled creep may barely meet the required deformation under such conditions. This is further proved by the strain rate vs. stress relations obtained from stress relaxation

tests (Fig. 4.33), where the strain rates are mainly below $10^{-4}s^{-1}$ for creep processes. Therefore, only the other two plastic deformation mechanisms seem to compensate the high thermal mismatch stresses arising during fast thermal cycling. To determine the dominating deformation mechanism a detailed investigation of the crystallographic microstructure evolution of the braze matrix during thermal cycling was conducted.

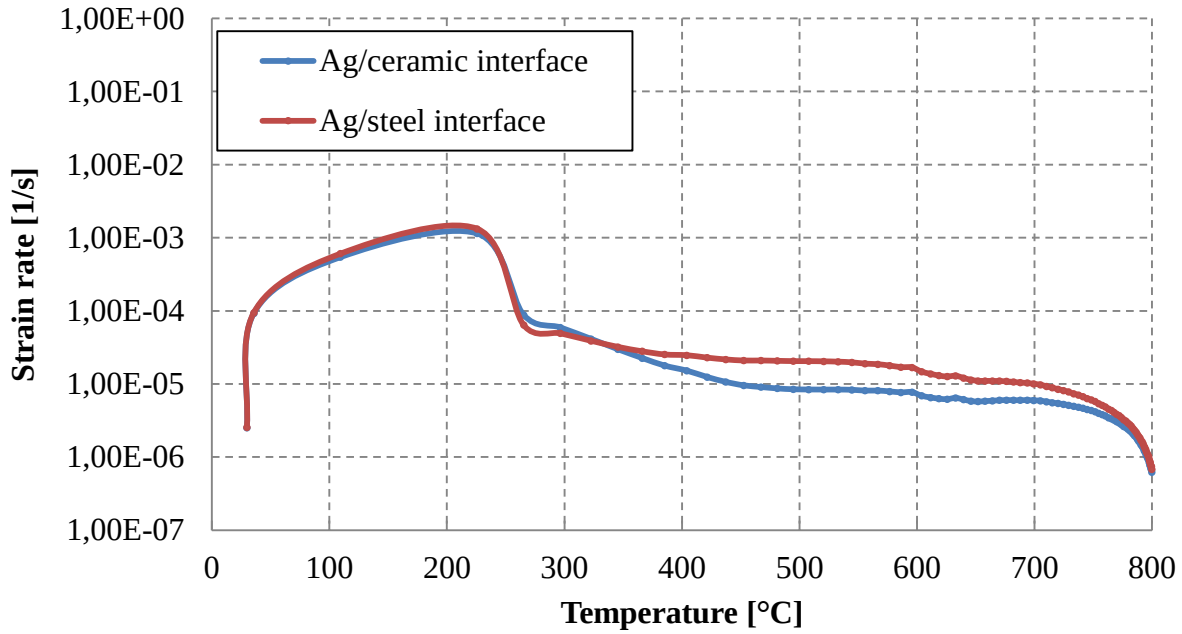


Fig. 4.42 Deformation rate of the braze matrix at the ceramic and steel interface during heating

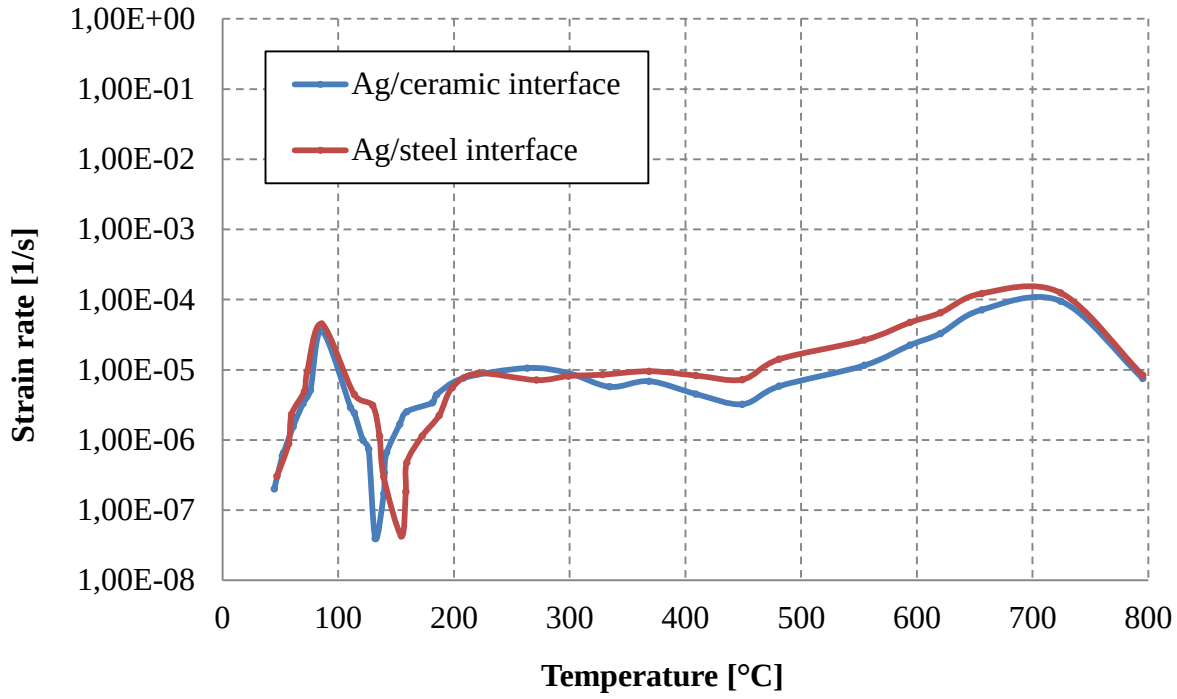


Fig. 4.43 Deformation rate of the braze matrix at the ceramic and steel interface during cooling

4.4.4 Twinning and recrystallization

Ag has an fcc crystal structure, low stacking fault energy [Lev66] and low twin boundary energy [Got04]. Because of its low stacking fault energy, twinning is likely to appear in pure Ag. During thermal cycling, shear load dominates in the braze matrix, which promotes mechanical twinning. For this reason twinning is considered to be an important deformation mechanism for Ag based brazes. Furthermore twin formation may generate mobile high angle grain boundaries [Got04] and may thus facilitate the nucleation of recrystallization sites and maybe even dynamic recrystallization during thermal cycling could occur. By twining and recrystallization most of the thermal mismatch stresses could be compensated, enabling the braze joint to withstand even severe thermal cycling.

- Pure Ag joints

Pure Ag joints exhibit a single crystal microstructure in the as-brazed state [Bra12] (Fig. 4.44). Twinning of the braze matrix is already observable after only 250 thermal cycles (Fig. 4.45). The newly created twin boundaries have an angle of approximately 60 °, which corresponds well to the twin boundary angle calculated for fcc metals (~ 55 °).

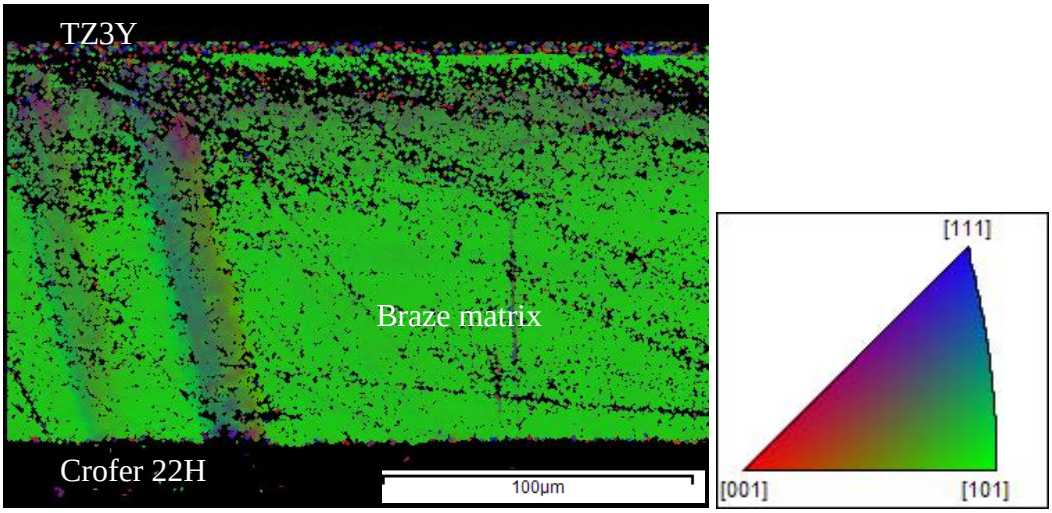


Fig. 4.44 Single crystal matrix microstructure of a pure Ag joint in the as-brazed state [Bra12]

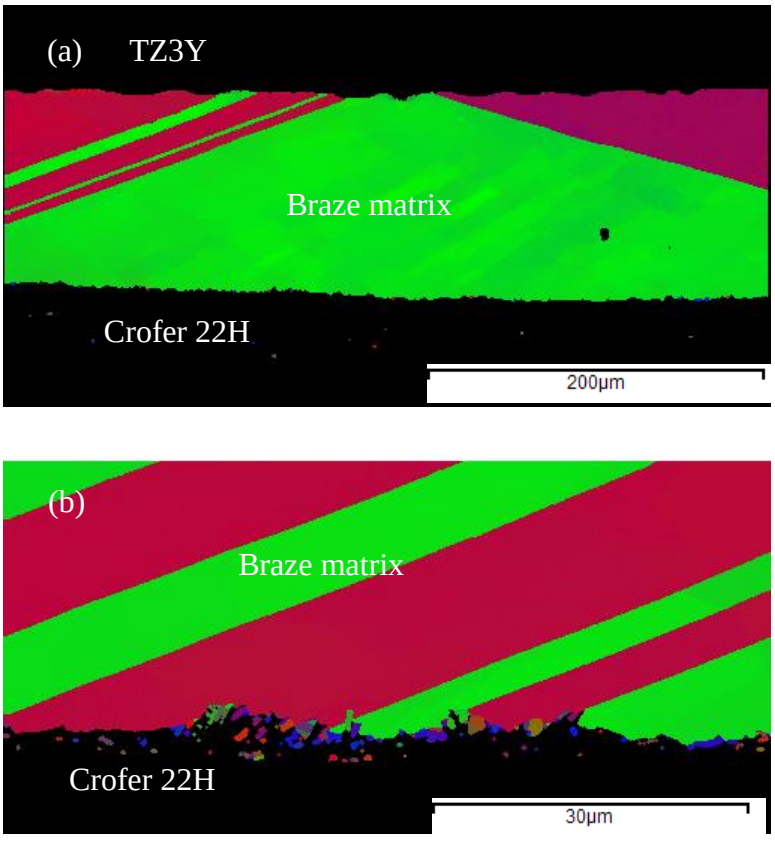


Fig. 4.45 Twinned matrix crystal structure of a pure Ag braze after 250 thermal cycles

The crystal structure of the braze matrix after delamination from the ceramic joining partner (after 500 thermal cycles) is shown in Fig. 4.46. Obviously not only twinning, but also recrystallization takes place in the braze matrix with increasing number of thermal cycles. Grain boundary migration, based on the original twin boundaries can clearly be observed.

Interestingly, lots of small grains with various crystal orientations can be observed at the braze/steel interface (Fig. 4.45b, 4.46). The formation of these small grains may be induced by the growth of the reaction layer (cf. reaction layer in the as-brazed state: Fig. 4.1). Ag may adopt different crystallographic orientations in order to accommodate to the growing (Ag,Cr,Mn)O-reaction products (cf. red circles in Fig. 4.47). These small crystals may provide an additional nuclei for recrystallization, which can be observed after 500 cycles, too (Fig. 4.46: white circles). In contrast to that, recrystallization at the braze/ceramic interface seems to be almost solely related to the movement of twin boundaries. Reaction products at the braze/ceramic interface were neither observed in the as-brazed state, nor after annealing in air (cf. chapters 4.1, 4.2). With adhesion at this interface most probably being related to atomic bonds, such recrystallization nuclei may difficult to be generated (cf. chapter 2.6.3). Missing recrystallization at the interface to the ceramic may cause accumulation of thermal mismatch stresses, which may cause the preferential failure at the braze/ceramic interface in thermal cycling operation.

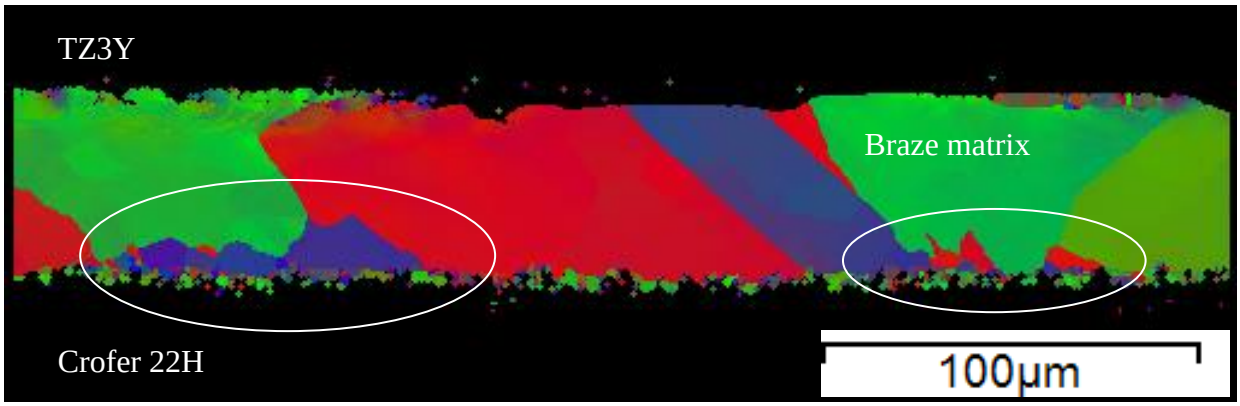


Fig. 4.46 Crystallographic orientation of the matrix of a pure Ag joint after 500 rapid thermal cycles

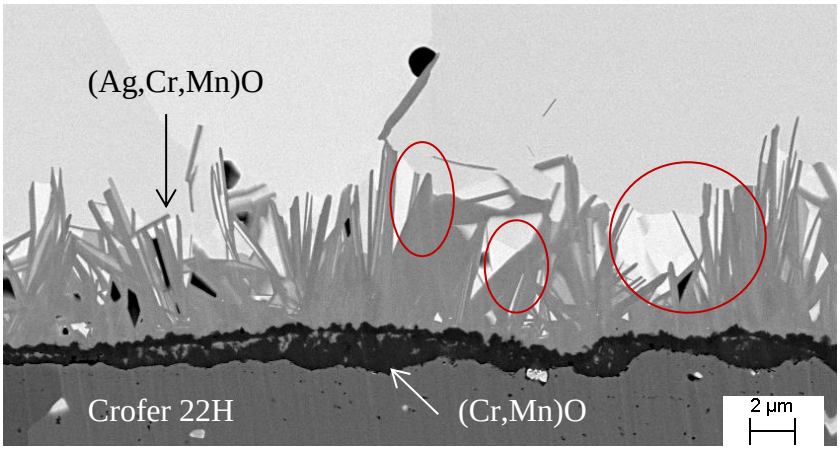


Fig. 4.47 Morphology of the reaction layer in a pure Ag joint after 500 rapid thermal cycles

- **Ag4Cu joint**

Like pure Ag, the Ag4Cu braze exhibits a single crystal microstructure in the as-brazed state (Fig. 4.48a). The braze delaminated from the ceramic joining partner and exhibited a polycrystalline microstructure after 220 cycles (Fig. 4.48b) already. In comparison to the pure Ag braze, twinning is less distinct in case of the Ag4Cu braze. The copper mixed oxides, formed at the braze/steel interface during brazing, are unstable during high temperature operation (cf. chapter 4.2.1) and might be reduced by Cr and/or Mn diffusing from the steel. The resulting Cu then might dissolve in the braze matrix. During prolonged operation in air dissolved Cu may again react with chromium and oxygen to form the strip-like (Cr,Cu)O precipitates within the braze matrix (cf. Fig. 4.39). Copper in solid solution might change the stacking fault energy of the silver matrix and the twin boundaries, resulting in retarded twinning. Formation of the (Cr,Cu)O precipitates may preferentially occur at crystal defects, like grain boundaries or twin boundaries, where they pin the boundary movement during thermal cycling. Consequently formation of these precipitates would retard the recrystallization process of the braze matrix. With both, retarded twinning and recrystallization, the thermal mismatch stresses may not be sufficiently compensated, resulting in a continuous stress accumulation in the braze matrix, finally leading to premature joint failure in thermal cycling.

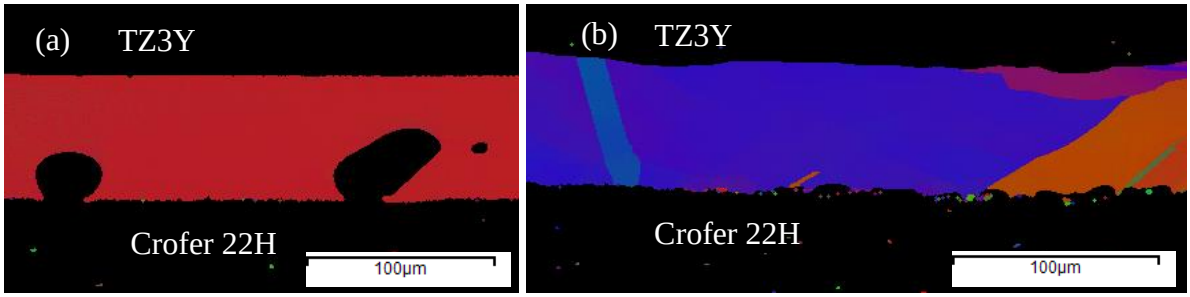


Fig. 4.48 Crystallographic orientation of the matrix of an Ag4Cu braze joint in a) the as-brazed state and b) after 220 rapid thermal cycles

- **Ag0.5Al joints**

Because of a remarkable difference in crystal structure in the as-brazed state (Fig. 4.49a) the Ag0.5Al joints present enhanced thermal cycling resistance. After brazing the braze matrix exhibits a polycrystalline structure with a texture (Fig. 4.49b), indicating that the crystals have similar orientations. The formation of this polycrystalline microstructure is due to the formation of (Ag,Cr)O precipitates during brazing, which have a plate-like morphology (Fig. 4.12) and act as grain nuclei during solidification. During solidification, the temperature gradient is dominated by the cooling of the joining partners, thus "directional solidification" leads to quite similar crystallographic orientation of the matrix grains.

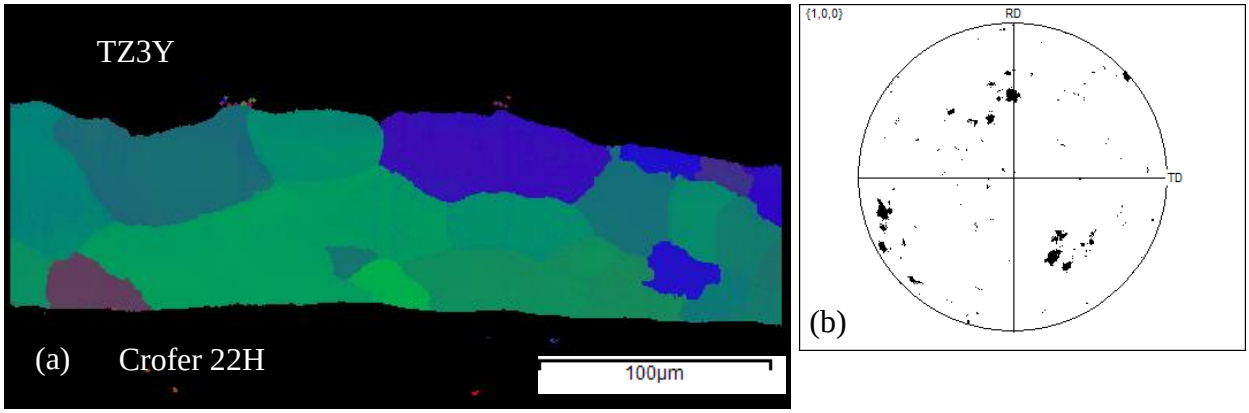


Fig. 4.49 Grain structure of a Ag0.5Al joint in the as-brazed state: a) EBSD mapping and b) crystal orientation of the braze matrix in a {100} stereographic projection

Twinning is the dominating deformation mechanism of Ag0.5Al joints. Several twins and twin boundaries (straight grain boundaries) can be observed in the braze matrix after 463 thermal cycles (Fig. 4.50a). Interestingly, grains with orientations greatly differing from that of the neighboring grains, emerge at grain boundaries (white circles in Fig. 4.50a) during cycling. The original grain boundaries obviously provide preferential sites for the nucleation

of the recrystallization process. The stored thermal mismatch energy kinetically promotes recrystallization. That recrystallization is promoted in Ag0.5Al joints is further proved by Fig. 4.50c, showing a distinct recrystallized matrix structure, which was observed after 1000 fast thermal cycles. The grain size distribution apparently refers to the mechanical stress distribution in the joint: While the grain size is comparatively high in the middle of the joint, recrystallization seems to be more pronounced near the interfaces with grains becoming smaller at both the braze/steel and the braze/ceramic interface, where higher thermal mismatch stresses are generated.

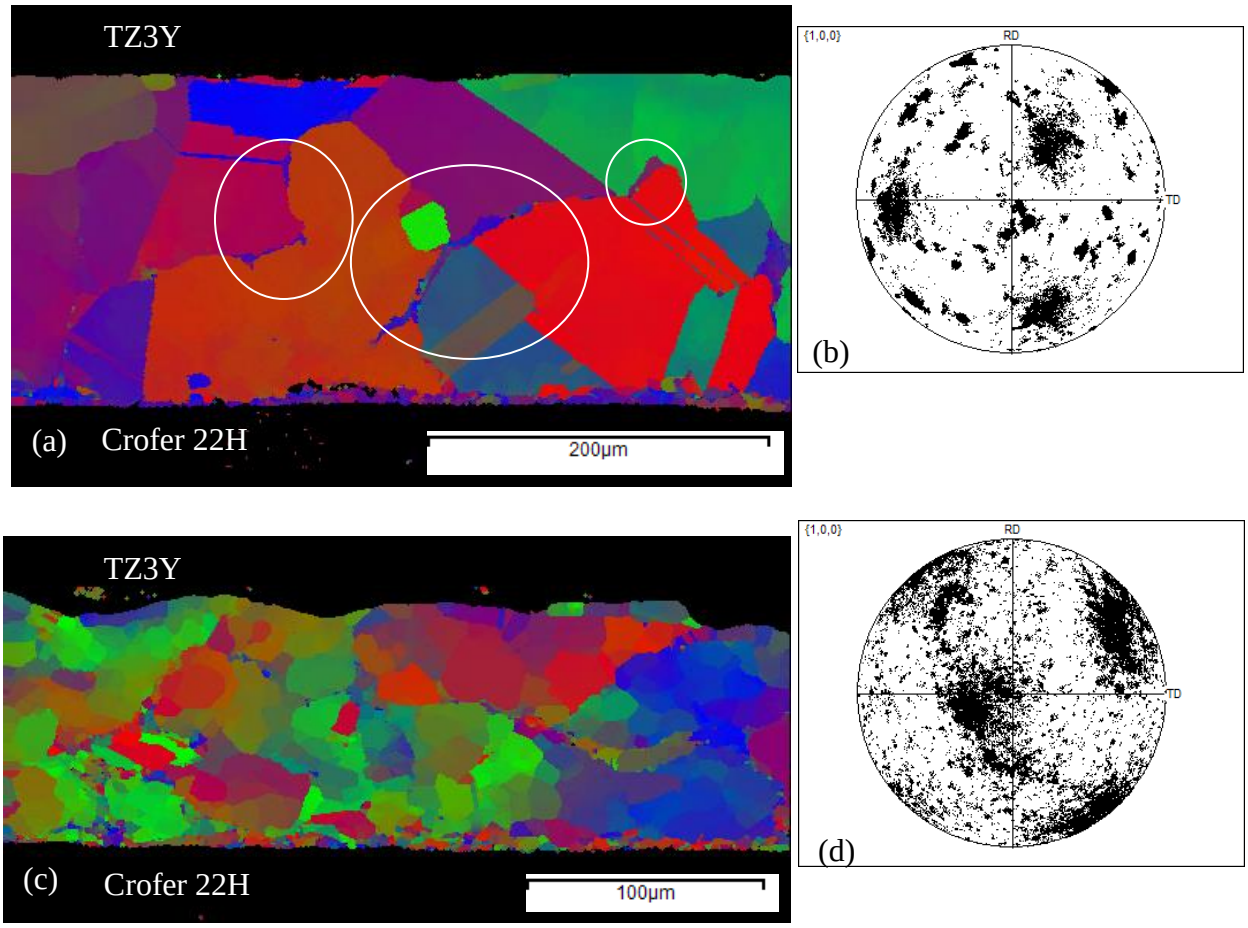


Fig. 4.50 Grain structures of Ag0.5Al joints: a) Crystal structure after 463 thermal cycles, b) crystal orientation of the braze matrix in {100} stereographic projection after 463 thermal cycles, c) crystal structure after 1000 thermal cycles and d) crystal orientation of the braze matrix in {100} stereographic projection after 1000 thermal cycles

The overall texture after 463 thermal cycles indicates that grains with differing orientations started to emerge in the highly directional original braze texture. After 1000 cycles the grains still show a preferential orientation, proven by the stereographic projection in Fig. 4.50d, but

obviously the crystal structure tends towards unidirectionality with increasing cycle number. With the increased number of mobile high angle grain boundaries (twin and recrystallized grain boundaries) and continuing recrystallization, the thermal mismatch stresses are better accommodated in case of the Ag0.5Al braze. For this reason, the thermal cycling performance of this braze variant is by far superior to pure Ag and Ag4Cu joints. Because thermal stresses are better compensated, the braze/ceramic interface does not remain the weakest link of the joint in thermal cycling. In contrast, the braze matrix starts to be degraded under cyclic plasticization. Defects nucleate and enlarge and pores form, which finally lead to joint failure by rupture of the matrix.

4.4.5 Discussion and conclusions

Mechanical twinning is a low temperature deformation mechanism, while recrystallization is a high temperature phenomenon [Got04]. Both mechanisms are able to strongly accommodate stresses when occurring. The microstructural evidence proofs that both phenomena effect stress compensation during rapid thermal cycling of braze joints.

In case of the pure Ag braze, the initial crystal structure of the braze matrix renders the easy occurrence of twinning. Furthermore the occurrence of twinning provides high angle mobile grain boundaries, which promote recrystallization. Alloying of the Ag braze can positively or negatively influence the kinetics of both processes like it is demonstrated for the Ag4Cu and the Ag0.5Al braze variants. As a result, the thermal cycling performance of the resulting braze joints can be tailored in wide range: In case of the Ag4Cu joints the cycling capability decreases, because of microstructural evolution. The polycrystalline matrix structure of the Ag0.5Al joints promotes recrystallization. In this case microstructural evolution increases the resistance to thermal cycling.

The combination of twinning and recrystallization provides an effective way to compensate thermal mismatch stresses during fast temperature changes and thus is an important combination of mechanisms for improving the thermal cycling resistance of the joints. Proper utilization of the unveiled mechanisms (i.e. by tailored chemical composition of the braze, tuned initial microstructure and preferable operation parameters) provides increased persistence of Ag-based braze joints even under demanding thermo-mechanical loading conditions.

5. Conclusions and outlook

The properties of Crofer® 22 H steel / zirconia ceramic joints produced by utilizing three reactive air brazes (pure Ag, Ag4Cu, Ag0.5Al) were characterized in three different aspects: Interfacial strength in the as-brazed and aged state at ambient temperature and interface and matrix strength at operating temperature as well as thermal cycling resistance.

The three brazes exhibit satisfactory as-brazed joint properties. In ambient temperature delamination testing the braze/steel interface limits joint strength, because of the brittle reaction layer which forms during brazing. Aging in air promotes the growth of the reaction layer, thus decreasing the fracture resistance of all the braze variants. Competing delamination at the braze/ceramic interface is induced during aging in reducing atmosphere, because diffusion of elements (Cr,Mn) from the steel causes formation of a brittle (Cr,Mn)O reaction layer at the braze/ceramic interface. The three brazes exhibit comparable strength in the as-brazed state and after aging in air at 800 °C, while alloying by Cu and Al increases degradation during long-term operation in reducing atmosphere.

In high temperature operation, the shear resistance of the three brazes varies according to the different operating temperatures (800 °C, 675 °C, 550 °C). At 800 °C the braze/ceramic interface and/or the braze matrix constitute the weakest links of all the three brazes, both in the as-brazed state and after aging in air. At lower temperature, competing delamination occurs at the braze/steel interface as well. Contrary to the ambient temperature delamination tests, aging in air increases the shear strength of all the joining variants. At 800 °C as-brazed Ag0.5Al joints exhibit the highest resistance to shear creep, but aging in air increases the shear creep resistance of the pure Ag and the Ag4Cu braze to a level comparable to the Ag0.5Al braze.

Ag0.5Al joints exhibit far better tolerance to fast thermal cycling than the other two joining variants. In conclusion, considering the results of all the three brazes under different testing conditions, the Ag0.5Al joints exhibit the most satisfactory mechanical strength and overall joint properties of the three investigated brazes.

Besides mechanical properties, detailed considerations regarding adhesion, aging, deformation and damage mechanisms are the key essence of this thesis: Regarding the adhesion mechanism, oxygen is discovered to act as an indispensable bonding agent at the braze/ceramic interface in reactive air brazing and furthermore at the braze/oxidized steel interface. The advanced Ag0.5Al (IOT) braze foil proves excellent potential for fast thermal cycling applications, because of its superior twinning and recrystallization induced accommodation of thermal mismatch stresses. This result shows that in future braze alloy and process development especially the thermomechanical performance can be enhanced by tuning the initial microstructural constitution. Furthermore, it could be shown by the example of a zirconia / austenitic steel joint that reactive air brazing is a promising approach for production of metal / ceramic compounds with high thermal mismatch.

Future work should concentrate on the following topics, which were not covered by this thesis:

- Development of diffusion barrier layers on chromia forming alloys and/or characterization of alumina forming steels to tackle interfacial degradation during long-term isothermal operation.
- Thermomechanical performance under most demanding superimposed thermal cycling and dual atmosphere operation.
- Detailed examination of the feasibility of reactive air brazing for joining materials with larger thermal expansion coefficient mismatches (f. e. zirconia ceramics and austenitic steels, large CTE ceramics like perovskites and ferritic steels).
- Evaluation of varying heating / cooling rates during thermal cycling to estimate thermally induced threshold strain rates to either trigger or inhibit twinning and recrystallization.

References

[Aga96] Agathopoulos, S.; Moretto, P.; Peteves, S. D.; Emiliano, J. V.; Correia, R. N.: Brazing of Zirconia to Ti and Ti6Al4V. In: 98th annual meeting of the American ceramic society in Indianapolis, Indiana, April 14-17, 1996

[All43] Allen, N. P: The effect of pressure on the liberation of gases from metals (with special reference to silver and oxygen). In: Journal of the Institute of Metals 49 (1943), P. 317-346

[Ass97] Assal, J.; Hallstedt, B.; Gauckler, L. J.: Thermodynamic Assessment of the Silver-Oxygen System. In: Journal of American ceramic Society 80 (1997), P. 3054-3060

[Ass98] Assal, J.; Hallstedt, B.; Gauckler, L. J.: Thermodynamic Assessment of the Ag-Cu-O System. In: Journal of Phase Equilibria 19 (1998), P. 351-360

[Bai99] Baird, J.K.; King, T.R.; Stein, C.: Diffusion of oxygen in silver. In: Journal of Physics and Chemistry of Solids 60 (1999), P.891-894

[Bas11] Bassat, J.M.; Mesguich, D.; Ferchaud, C.; Zhang-Steenwinkel, Y.; van Berkel, F.; Aymonier, C.; Watkins, J.J.; Grenier, J.C.: Doped/Undoped Ceria buffer layers for improved LT-SOFC performances with $Pr_2NiO_{4+\delta}$ Cathode. In: ECS Transactions 35(2011), P. 1945-1954

[Bas12] Basuki, W. W; Kraft, O.; Aktaa, J.: Optimization of solid-state diffusion bonding of Hastelloy C-22 for micro heat exchanger applications by coupling of experiments and simulations. In: Materials Science and Engineering A 538 (2012), P. 340-348

[Ber71] Bernard, C.; Lupis, C.H.P: The surface tension of liquid silver alloys: Part Π.Ag-O alloys. In: Metallurgical and Materials Transactions B 2 (1971), P. 2991-2998

[Ber89] Beraud, C.; Courbiere, M.; Esnouf, C.; Juve, D.; Treheux, D.: Study of Copper-alumina bonding. In: Journal of Materials Science 24 (1989), P. 4545-4554

[Bin06] Bin, W.; Heidelberg, A.; Boland, J.; Sader, J.; Sun, X.; Li, Y.: Microstructure-Hardened Silver Nanowires. In: *Nano Letters6* (2006), P. 468-472

[Blu05] Blum, L.; Meulenberg, W.A.; Nabielek, H.; Steinberger-Wilckens, R.: Worldwide SOFC technology overview and benchmark. In: International journal of Applied ceramic tecnology2(2005), P.482-492

[Blu07] Blum, L; Buchkremer, H.-P; Gross, S.; Gubner, A.; (Bert) de Haart, L.G.J.; Nabielek, H.; Quadakkers, W.J.; Reisgen, U.; Smith, M.J.; Steinberger-Eilckens, R.; Steinbrech, R.W.; Tietz, F.; Vinke, I.C.: Solid oxide fuel cell development at Forschungszentrum juelich. In: Fuel cells 07 (2007), P. 204-210,

[Bob10] Bobzin, K.; Schläfer, T.; Kopp, N.: Konturtreue Lote zum Fügen von Keramik an Luft. Löt 2010, 30.06.2010, Deutscher Verband für Schweißen und verwandte Verfahren e. V., P.64-69

[Bob11] K. Bobzin, N. Bagcivan, N. Kopp, T. Beck, B. Kuhn, C. Li: „Entwicklung neuer Lote und Prozesse zum Fügen von Keramik-Metall-Verbunden mittels Reactive Air Brazing“. 14. Werkstofftechnisches Kolloquium 2011, 01-02.09.2011, Werkstoffe und werkstofftechnische Anwendungen Band 043, 237-244, 2011

[Cha88] Chatain, D.; Coudurier, L.; Eustathopoulos, N.: Wetting and interface bonding in ionocovalent oxide-liquid metal systems. In: Revue De Physique Appliquee 23 (1988), P. 1055-1064

[Cha89] Charalambides, P. G. ; Lund, J. ; Evans, A. G. ; Meeking, R. M.: A Test Specimen for Determining the Fracture Resistance of Bimaterial Interfaces. In: Journal of Applied Mechanics 56 (1989), P. 77-82

[Cha90] Charalambides, P. G. ; Cao, H. C. ; Lund, J. ; Evans, A. G.: Development of a Test Method for Measuring the Mixed-Mode Fracture Resistance of

Bimaterial Interfaces. In: Mechanics of Materials 8 (1990), P. 269-283

[Cha93] Chatain, D; Muolo, M.L; Sangiorgi, R.: In S.D. Peteves (Ed.), Designing Ceramic Interfaces, Comm. Eur. Comm. Publ, Luxembourg, 1993, P.359-367

[Cha94] Chatain, D.; Chabert, F.; Ghetta, V.: New experimental Setup for wettability characterization under monitored oxygen activity: II, wettability of Sapphire by silver-oxygen melts. In: Journal of American ceramic society 77 (1994), P. 197-201

[Cha99] Charojrochkul, S.; Choy, K. L.; Steele, B. C. H.: Cathode/Electrolyte Systems for Solid Oxide Fuel Cells Fabricated Using Flame Assisted Vapour Deposition Technique. In: Solid State Ionics 121 (1999), P. 107-113

[Cla69] Clauss, F.J.: Engineer's guide to high-temperature materials, 1969

[Cla83] Claussen, N.: Umwandlungsverstärkte keramische Werkstoffe. In: Zeitschrift für Werkstofftechnik 13 (1983), Nr. 4, P. 137-147

[Din91] Dinsdale, A. T.: SGTE data for pure elements. In: Calphad 15 (1991), P. 317-425

[Din93] DIN V ENV 658: Mechanische Eigenschaften von Keramik-Verbundwerkstoffen bei Raumtemperatur. In: Normenausschu_ Materialprüfung (NMP) im DIN Deutsches Institut für Normung e. V. Teil 6 (Februar 1993)

[Dus62] Dushman, S.; Lafferty, J.J: Scientific foundations of vacuum technique, 1962, New York,

[Dre92] Dreier, G.; Meyer, M.; Schmauder, S.; Elssner, G.: Fracture mechanics studies of thermal mismatch using a four-point bending specimen. In: Acta Metallurgica et Materialia 40 (1992), P. 345-353

[Elr09] Elrefaey, A.; Tillmann, W.: Solid state diffusion bonding of titanium to steel using a copper base alloy as interlayer. In: Journal of Materials processing technology 209 (2009), P. 2746-2752

[Eus99] Eustathopoulos, N.; Nicholas, M. G.; Orevet, B.: Wettability at high temperatures. In: Pergamon Materials Series 3 (1999), P.1-420

[Eus01] Eustathopoulos, N.; Drevet, B.; Muolo, M. L.: The oxygen-wetting transition in metal/oxide systems. In: Materials Science and Engineering A 300 (2001), P. 34-40

[Eva85] R.W.Evans, B.Wilshire, Creep of metals and alloys, book, 1985

[Eva86] Evans, A. G.; Cannon, R. M.: Overview No. 48: Toughening of brittle solids by martensitic transformations. In: Acta metallurgica 34 (1986), P. 761

[Faw09] Fawzy, A.: Creep properties of Ag-2wt% Cu alloy in the solid solution region. In: Journal of alloys and compounds 486 (2009), P. 768-773

[Fer05] Fergus, J. W.: Metallic interconnects for solid oxide fuel cells. In: Materials Science and Engineering A 397 (2005), P. 271-283

[Fro82] Frost, H.J.; Ashby, M.F.: Deformation-Mechanism maps: The plasticity and creep of metals and ceramics, 1982, http://engineering.dartmouth.edu/defmech/

[Fro08] Froitzheim, J.: Ferritic steel interconnectors and their interactions with Ni base anodes in solid oxide fuel cells (SOFC), Dissertaion, RWTH Aachen, 2008

[Fro08b] Froitzheim, J.; Meier, G. H.; Niewolak, L.; Ennis, P. J.; Hattendorf, H.; Singheiser, L.; Quadakkers, W. J.: Development of high strength ferritic steel for interconnect application in SOFCs. In: Journal of Power Sources 178 (2008), P. 163-173

[Gal80] Gallois, B.: Contribution to the physical-chemistry of metal-gas and metal-alumina interfaces, Ph.D thsis, Carnegie Mellon University, Pittsburgh, PA, UA, 1980

[Gor96] Goretta, K.C; Delaney, W.E.; Routbort, J.L.; Wolfenstine, J.; Zhang, W.; Hellstrom, E.E: Creep of silver at 900 ℃, In: Superconductor Science and Technology 9 (1996), P. 422-426

[Gor96b] Goretta, K.C.; Routbort, J.L.; Thayer, R.L.; Carroll, J.P.; Wolfenstine, J.; Kessler, J.; Schwartz, J.: Deformation of Ag/1.2at.%Mg. In: Physica C 265 (1996), P. 201-206

[Got04] Gottstein, G. : Physical foundations of Materials Science, 2004, Springer, Berlin

[Göd11] Gödeke, D.; Dahlmann, U.: Study on the crystallization behavior and thermal stability of glass-ceramics used as solid oxide fuel cell-sealing materials. In: Journal of Power Sources 196 (2011), P. 9046-9050

[Han00] Hanson, W. B.; Ironside, K. I.; Fernie, J. A.: Active metal brazing of Zirconia. In: Acta Materialia 48 (2000), P. 4673-4676

[Hen04] Henderson, D.W.; Woods, J.J.; Gosselin, T.A.; Bartelo, J.: The microstructure of Sn in near-eutectic Sn-Ag-Cu alloy solder joints and its role in thermomechanical fatigue, In: Journal of material research 6 (2004), P. 1608-1612

[Hil03] Hilpert, K.; Quadakkers, W. J.; Singheiser, L: Chapter 74, Interconnects in Handbook of Fuel Cells, P. 1037-1054

[Hof98] Hofinger, I. ; Oechsner, M. ; Bahr, A. H. ; Swain, M. V.: Modified Four-Point Bending Specimen for Determining the Interface Fracture Energy for Thin, Brittle Layers. In: International Journal of Fracture 92 (1998), P. 213-222

[Hol03] Holtappels, P.: Fabrication and Performance of Advanced Multi-Layer SOFC Cathodes. In: Journal of the European Ceramic Society 22 (2002), P. 41- 48

[Hon89] Hong, S.H.; Yu, J.: Effect of prior austenite grain size on creep properties and on creep crack growth in 3.5NiCrMoV steel. In:Scripta metallurgica 23(1989), P. 1057

[Hor08] Horita, T.; Kishimoto, H.; Yamaji, K.; Xiong, Y.; Sakai, N.; Brito, M. E.; Yokokawa, H.: Evaluation of Laves-phase forming Fe-Cr alloy for SOFC interconnects in reducing atmosphere. In: Journal of Power sources 176 (2008), P. 54-61

[Ide07] Ide, S.; Funakawa, Y.; Kato, Y.; Furukimi, O.: Retardation of 20%Cr Steel oxidation with Laves phase precipitation. In: Materials Science Forum 539-543 (2007), P. 4887-4890

[Jar] Jarrige, J.; Joyeux, T.; Lecompte, J. P.; Labbe, J. C.: Influence of oxygen on the joining between copper and aluminium nitride. In: Journal of the European Ceramic society 27 (2007), P. 337-341

[Juh96] Juhl, M.; Primdahl, S.; Manon, C.; Mogensen, M.: Performance/Structure Correlation for Composite SOFC Cathodes. In: Journal of Power Sources 61 (1996), P. 173 - 181

[Kar92] Karakaya, I.; Thompson, W. T.: The Ag-O (Silver-Oxygen) System. In: Journal of Phase equilibria 13 (1992), P. 137-142

[Kar99] Kara-Slimane, A.; Mbongo, B.; Treheux, D.: Adhesion and reactivity in the copper-alumina system: influence of oxygen and silver. In: Journal of Adhesion Science and Technology 13 (1999), P. 35-48

[Kar08] Kar, A.; Ghosh, M.; Ray, A. K.; Ray, A. K.: Effect of interfacial thickness and residual stress on the mechanical property of the alumina-stainless steel braze joint interface. In: Materials Science and Engineering A 498 (2008), P. 283-288

[Kim05] Kim, J. Y.; Hardy, J. S.; Weil, K. S.: Effects of CuO contect on the wetting behavior and mechanical properties of a Ag-CuO braze for ceramic joining. In: Journal of American ceramic society 88 (2005), P. 2521-2527

[Kim07a] Kim, J. Y.; Hardy. J. S.; Weil, K. S.: Ag-Al based air braze for high temperature electrochemical devices. In: International journal of Hydrogen Energy 32 (2007), P. 3754-3762

[Kim07b] Kim, J. Y.; Hardy, J. S.; Weil, K. S.: Dual-atmosphere tolerance of Ag-CuO-based air braze. In: International Journal of Hydrogen Energy 32 (2007), P. 3655-3663

[Kim08] Kim, J. Y.; Choi, J.; Weil, K. S.: Mechanical properties and dual atmosphere tolerance of Ag-Al based braze. In: International Journal of Hydrogen energy 33 (2008), P. 3952-3961

[Kim08b] Kim, J. Y.; Engelhard, M.; Choi, J. P.; Weil, K. S.: Effects of atmospheres on bonding characteristics of silver and alumina. In: International journal of Hydrogen Energy 33 (2008), P. 4001-4011

[Klo05] Kloc, L.; Fiala, J.: Harper-Dorn creep in metals at intermediate temperatures revisited: constant structure test of pure Al. In: Materials Science and Engineering A 410-411 (2005), P. 38- 41

[Kna68] Knacke, O.; Meixner, M.: Blasenbildung im erstarrenden Silber. In: Zeitschrift für Metallkunde 59 (1968), P. 114-117

[Kop06] Koppitz, T.: Interne Untersuchung: Dilatometerversuche an SOFC-Materialien. Forschungszentrum Jülich, Zentralabteilung Technologie (ZEA), Abteilung Sonderfügetechnik, 2006

[Ksi08] Ksiazek, M.; Mikulowski, B.: Bond strength and microstructure investigation of $Al_2O_3/Al/Al_2O_3$ joints with surface modification of alumina by titanium. In: Materials Science and Engineering A 495 (2008), P. 249-253

[Kuh08] Kuhn, B.: Bruchmechanische Untersuchung von Metall/Keramik-verbundsystemen für die Anwendung in der Hochtemperaturebrennstoffzelle (SOFC), Dissertation, 2008

[Kuh09] Kuhn,B.; Wetzel, F.J.; Malzbender, J.; Steinbrech, R.W.; Singheiser, L.: Mechanical performance of reactive-air-brazed (RAB) ceramic/metal joints for solid oxide fuel cells at ambient temperature, In: Journal of Power Sources 193 (2009), P. 199-202

[Kuh11] Kuhn, B.; Jimenez, C. A.; Niewolak, L.; Hüttel, T.; Beck, T.; Hattendorf, H.; Singheiser, L.; Quadakkers, W. J.: Effect of Laves phase strengthening on the mechanical properties of high Cr ferritic steels for solid oxide fuel cell interconnect application. In: Materials Science and Engineering A 528 (2011), P. 5888-5899

[Lan03] Lane, M.: Interface Fracture. In: Annual Review of Materials Research 33 (2003), P. 29-54

[Lev66] Leverant, G.R.; Lenel, F.V.; Ansell, G.S.: The high-temperature steady-state creep of pure silver and internally oxidized silver-magnesium alloys. In: Transactions of the ASM, 59 (1966), P. 890-898

[Lin1] http://en.wikipedia.org/wiki/Zirconium_dioxide

[Lin2] Crofer® 22 H, Crofer® 22 APU: http://www.thyssenkrupp-vdm.com/downloads/materialdatenblaetter/?no_cache=1

[Lin3] http://www.dew-stahl.com/fileadmin/files/dew-stahl.com/documents/Publikationen/Werkstoffdatenblaetter/RSH/1.4841_de.pdf

[Lin4] www.thyssenkrupp-nirosta.de/.../PDF/thermax.pdf - Hitzebeständige Stähle THERMAX® - ThyssenKrupp Nirosta

[Lin5] http://www.sppusa.com/reference/white_paper/wp_ss.pdf

[Lin6] http://www.m-woite.de/en/materials/14841.shtml

[LiY09] Li, Y.; Wu, J.; Johnson, C.; Gemmen, R.; Scott, X.; Liu, X.: Oxidation behavior of metallic interconnects for SOFC in coal syngas. In: International journal of Hydrogen Energy 34 (2009), P. 1489-1496

[Li12a] Li, C.; Kuhn, B.; Brandenberg, J.; Beck, T.; Singheiser, L.: Mechanical behavior of advanced reactive air brazed joints. In: 5th International Brazing and Soldering Conference, April 22-25, 2012, Las Vegas, Nevada, USA

[Li12b] Li, C.; Kuhn, B.; Brandenberg, J.; Beck, T.; Singheiser, L.; Bobzin, K.; Bagcivan, N.; Kopp, N.: Improving contour accuracy and strength of reactive air brazed (RAB) ceramic/metal joints by controlling interface microstructure. In: Advanced Engineering materials 14 (2012), P.394-399

[Lij02] Li, J. Q.; Xiao, P.: Joining alumina using an alumina/metal composite. In: Journal of the European Ceramic Society 22 (2002), P. 1225-1233

[Liu08] Liu, Y.: Performance evaluation of several commercial alloys in a reducing environment. In: Journal of Power Sources 179 (2008), P. 286-291

[Liu09] Liu, G. W.; Li, W.; Qiao, G. J.; Wang, H. J.; Yang, J. F.; Lu, T. J.: Microstructures and interfacial behavior of zirconia/stainless steel joint prepared by pressureless active brazing. In: Journal of Alloys and Compounds 470 (2009), P.163-167

[Mag00] Maguire, E.; Gharbage, B.; Marques, F. M. B.; Labrincha, J. A.: Cathode Materials for Intermediate Temperature SOFCs. In: Solid State Ionics 127 (2000), P. 329 - 335

[Mah10] Mahapatra, M.K.; Lu, K.: Glass-based seals for solid oxide fuel and electrolyzer cells – A review. In: Materials Science and Engineering R 67 (2010), P. 65-85

[Maj03] Majerus, P.: Neue Verfahren zur Analyse des Verformungs- und Schädigungsverhaltens von MCrAlY-Schichten im Wärmedämmschichtsystem. Schriften des Forschungszentrums Jülich; Reihe Energietechnik; ISBN 3-89336-372-6, 2003

[Mal03] Malzbender, J.; Steinbrech, R. W.; Singheiser, L.: Determination of the Interfacial Fracture Energies of Cathodes and Glass Ceramic Sealants in a Planar Solid-Oxide Fuel Cell Design. In: Journal of Material Research 18 (2003), P. 929- 934

[Mal07] Malzbender, J. ; Mönch, J. ; Steinbrech, R. W. ; Koppitz, T. ; Gross, S. ; Remmel, J.: Symmetric Shear Test of Glass-Ceramic Sealants at SOFC Operation Temperature. In: Journal of Materials Science 42 (2007), P. 6297-6301

[Mal09] Malzbender, J; Steinbrech, R.W.; Singheiser, L.: A review of advanced techniques for characterising SOFC behavior, In: Fuel Cells 09 (2009), P. 785-793

[May95] Mayr, C. ; Eggeler, G. ; Webster, G. A. ; Peter, G.: Double Shear Creep Testing of Superalloy Single Crystals at Temperatures Above 1000_C. In:

Materials Science and Engineering A199 (1995), P. 121-130

[Men10] Menzler, N.H.; Tietz, F.; Uhlenbruck, S.; Buchkremer, H.P.; Stöver, D.: Materials and manufacturing technologies for solid oxide fuel cells. In: Journal of material science 45 (2010), P. 3109-3135

[Meu03] Meulenberg, W. A.; Uhlenbruck, S; Wessel, E.; Buchkremer, H. P.: Oxidation behavior of ferrous alloys used as interconnecting material in solid oxide fuel cells. In: Journal of materials science 38 (2003), P. 507-513

[Muo08] Muolo, M. L.; Valenza, F.; Passerone, A.; Passerone, D.: Oxygen influence on ceramics wettability by liquid metals: Ag/α-Al_2O_3 - Experiments and modeling. In: Materials Science and Engineering A 495 (2008), P. 153-158

[Nai81] Naidich, J. N.: The wettability of solids by liquid metals. In: Progress in surface and membrane science 14 (1981), P.353-470

[Nie00] Nielsen, R.: "Zirconium and Zirconium Compounds" in Ullmann's encyclopedia of industrial chemistry, Wiley-VCH, Weinheim

[Pri66] Price, C.E.: On the creep behavior of silver. In: Acta Metallurgica 14 (1966), P. 1781-1799

[Qu06] Qu, W. ; Jian, L. ; Hill, J. M. ; Ivey, D. G.: Electrical and Microstructural Characterization of Spinel Phases as Potential Coatings for SOFC Metallic Interconnects. In: Journal of Power Sources 153 (2006), P. 114-124

[Rei08] Reichle, M. S.; Reisgen, U.; Koppitz, T.; Federmann, D.: Investigation of Reactive Air Brazing with Silver based brazing filler metals to improve the joining technology for the high temperature solid oxide fuel cell (SOFC), In: 8th European SOFC forum, 2008, Luzern, Switzland,

[Rya12] Ryan, E.M.; Recknagle, K.P.; Liu, W.; Khaleel, M.A.: The need for Nono-scale modeling in solid oxide fuel cells. In: Journal of Nanoscience and Nanotechnology 12(2012), P. 6758-6768

[Sal07] Salmang ; Scholze: Technische Keramik. Verlag Springer Berlin Heidelberg; ISBN 978-3-540-63273-3, 2007

[San82] Sangiorgi, R.; Muolo, M. L.; Passerone, A.: Surface tension and adsorption in liquid silver-oxygen alloys. In: Acta metallurgica 30 (1982), P. 1597-1604

[Sch42] Schenk, R. ; Bathe, A. ; Keuth, H. ; Süss, S. : On the activation of metas by foreign additions. IV. – Contributions to the chemistry of silver. In: Zeitschrift für anorganische und allgemeine Chemie 249 (1942), P. 88-89

[Sci01] Sciti, D.; Bellosi, A.; Esposito, L.: Bonding of zirconia to super alloy with the active brazing technique. In: journal of the European Ceramic Society 21 (2001), P. 45-52

[Ser11a] Serier, B.; Bouiadjra, B. B.; Belhouari, M.; Treheux, D.: Experimental analysis of the strength of silver-alumina junction elaborated at solid state bonding. In: Materials and Design 32 (2011), P. 3750-3755

[Ser11b] Serier, B.; Sellam, S.; Bouiadjra, B. B.; Treheux, D.: Effects of oxygen dissolved in metal on the strength of Silver-Alumina junctions formed in the solid state. In: Vacuum 85 (2011), P. 955-960

[Sim03] Simner, S. P.; Shelton, J. P.; Anderson, M. D.; Stevenson, J.W.: Interaction

Between La(Sr)FeO3 SOFC Cathode and YSZ Electrolyte. In: Solid State Ionics 161 (2003), P. 11-18

[Sin97] Singhal, SC.: Status of solid oxide fuel cell technology. In: Proceeding of 5th international symposium on materials science: SOFC (SOFC-V) (1997), P. 37

[Ste01] Steele, B. C. H.: Materials for Fuel-Cell Technologies. In: Nature 414 (2001), P. 345-352

[Sin03] Sinha, N.K.: Limitations of stress relaxation tests for determining stress dependence of strain rate at high temperatures. In: Scripta Materialia 48 (2003), P.731-736

[Ski01] Skinner, S. J.: Recent Advances in Perovskite-Type Materials for Solid Oxide Fuel Cell Cathodes. In: International Journal of Inorganic Materials 3 (2001), P. 113 - 121

[Smi62] Smithells, C.J.: Metals reference book, Butterworths, Washington, 1962, P.136-155

[Ste01] Steele, B.C.H.: Materials for Fuel-cell Technologies. In: Nature 414(2001). P. 345-352

[Tel07] Teland, A.U.; Bieler, T.R.; Zamiri, A.; Pourboghrat, F.: Incremental recrystallization/grain growth driven by elastic strain energy release in a thermomechanically fatigued lead-free solder joint. In: Acta Materialia 55(2007), P. 2265-2277

[Ter04] Terashima, S.; Takahama, K.; Nozaki, M.; Tanaka, M.: Recrystallization of Sn grains due to thermal strain in Sn-1.2Ag-0.5Cu-0.05Ni solder. In: Materials Transactions 4(2004), P. 1383-1390

[Tie03] Tietz, F.: Materials selection for solid oxide fuel cells. In: Materials Science Forum 426-432 (2003), P.4465-4470

[Tum89] Tummala, R. R.; Rymaszewski, E. J.: Microelectronics Packaging Handbook

[Tur96] Turner, M. R.; Evans, A. G.: An Experimental Study of the Mechanisms of Crack Extension Along an Oxide/Metal Interface. In: Acta materialia 44 (1996), P. 863- 871

[Uch08] Uchida, H.; Watanabe, M.: High-performance electrodes for medium-temperature solid oxide fuel cells. In: Modern Aspects of Electrochemistry, 2008, Chapter 2, P. 69

[Van00] Van herle, J.; Ihringer, R.; Sammes, N.M.; Tompsett, G.; Kendall, K.; Yamada, K.; Wen, C.; Kawada, T.; Ihara, M.; Mizusaki, J.: Concept and technology of SOFC for electric vehicles. In: Solid state Ionics 132 (2000), P. 333-342

[Wei03] Weil, K. S.; Kim, J. Y.; Hardy, J. S.; Development of Brazing Technology for use in High-Temperature Gas Separation Equipment. In: 17th Annual conference on Fossil Energy Materials, 22.-24. April 2003; Baltimore, Maryland (2003)

[Wei05a] Weil, K. S.; Coyle, C. A.; Darsell, J. T.; Xia, G. G.; Hardy, J. S.: Effects of thermal cycling and thermal aging on the hermeticity and strength of silver-copper oxide air-brazed seals. In: Journal of Power Sources 152 (2005), P. 97-104

[Wei05b] Weil, K. S.; Kim, J. Y.; Hardy, J. S.: Reactive air brazing: a novel method of sealing SOFCs and other solid-state electrochemical devices. In: Electrochemical and solid-state letters 8(2), P. A133-A136

[Wei05c] Weil, K. S.; Hardy, J. S.; Rice, J. P.; Kim, J. Y.: Brazing as a means of sealing ceramic membranes for use in advanced coal gasification processes. In: Fuel 85 (2006), P. 156-162

[Woo97] Woodford, D.A.: Stress relaxation testing for creep design analysis of metals, ceramics and polymers. In: Creep and Fracture of Engineering materials and structures, 1997

[Xia02] Xia, H.; Wu, A.; Fan, Y.; Zou, G.; Ren, J.: Effects of ion implantation on the brazing properties of high purity alumina. In: Surface & Coating technology 206 (2012), P. 2098-2104

[Yam90] Yamashita, M.: The stress-relaxation behavior of type 304 stainless steel. In: International journal of pressure vessels and piping 42 (1990), P.203-216

[Zha11] Zhao, Y.; Malzbender, J.; Gross, S.M.: The effect of room temperature and high temperature exposure on the elastic modulus, hardness and fracture toughness of glass ceramic sealants for solid oxide fuel cells. In: Journal of the European Ceramic society 31 (2011), P. 541-548

Figures

Fig. 2.1 Schematic view of the working principle of a solid oxide fuel cell [Rya12] 4
Fig. 2.2 Anode–supported cell concept (right) compared with the electrolyte-supported (left) [Blu05] 5
Fig. 2.3 Schematic "explosion" drawing of a repeating unit in light-weight planar SOFC-design [Kuh08] 8
Fig. 2.4 Phase diagram of the Ag-O system [Kar92] 16
Fig. 2.5 Variation of contact angle, surface tension and work of adhesion in the $Ag/O/Al_2O_3$ system as a function of the oxygen content in the surrounding atmosphere: 18
Fig. 2.6 Stacking of atoms at the Ag/Al_2O_3 (0001) interface, simulated by DFT (density functional theory) calculations: Four silver (grey atoms) layers on the left hand side, an oxygen (smaller-red) atom "layer" at the interface and alumina terminated with Al (Purple) [Muo08] 20
Fig. 2.7 Adsorption of oxygen-metal clusters at the metal-vapour and metal-oxide interface according to the model of Naidich [Nai81] 20
Fig. 2.8 Wetting behavior of three RAB-brazes on Al_2O_3 [Li12b] 21
Fig. 2.9 X-ray radiographic views of hermeticity testing samples (SOFC half cells brazed to deep-drawn Crofer® 22 APU sheets) utilizing the following braze systems: a) pure Ag, b) improved Al-added braze [Li12b] 22
Fig. 2.10 Phase diagram of the Ag-Cu system [Ass98] 24
Fig. 2.11 Phase diagram of the Ag-Al system [Din91] 25
Fig. 2.12 Typical curves of logarithmic creep and normal creep [Eva85] 26
Fig. 2.13 Deformation mechanism map of pure Ag [Fro82] 27
Fig. 3.1 Brazing jigs for ambient temperature delamination and high temperature double shear specimens 34
Fig. 3.2 Temperature of the specimens during thermal cycling [Kuh08] 36
Fig. 3.3 Schematic cross-sectional view of the: a) manifold-to-manifold joint; b) cell-to-manifold joint in an SOFC-stack [Kuh08] 36
Fig. 3.4 From stack design to sample geometry [Kuh08] 37
Fig. 3.5 Test setup for ambient temperature delamination test 38
Fig. 3.6 Typical load-deflection curve in ambient temperature delamination testing 39
Fig. 3.7 Schematic drawing of a cell to cell-frame braze joint in light weight planar stack design. Shear stresses develop between the metallic cell frame and cell 41
Fig. 3.8 Schematic view of the symmetric double shear testing set-up 42
Fig. 3.9 Testing set-up for double shear testing 43
Fig. 3.10 Schematic view of the strain measurement setup in machine (a); positioning of the specimen for the evaluation of machine and elastic ESE deformation (b) 45
Fig. 3.11 Elastic ESE and machine deformation versus load at 800 ℃ 45
Fig. 4.1 Microstructure of the steel/braze interface a) Crofer 22H; b) Crofer 22H_v 48

Fig. 4.2 Schematic drawing of typical crack progress layer and the elemental (Cr,Mn) distribution in the reaction layer: a) Crofer® 22 H/Ag/TZ3Y joints; b) Crofer® 22 H_v/Ag/TZ3Y 48
Fig. 4.3 Delaminated surface of the 1.4841/pure Ag/TZ3Y joint: (a) Steel surface; (b) ceramic/braze interface 49
Fig. 4.4 Cross-sectional overview of a Crofer® 22 H/Ag4Cu/TZ3Y braze joint 50
Fig. 4.5 Morphology of the reaction layer at braze/steel interface. a) Crofer® 22 H/Ag4Cu/TZ3Y; b) Crofer® 22 H/Ag8Cu/TZ3Y 50
Fig. 4.6 Schematic illustration of the elemental distribution in the reaction layers of AgCu joints 51
Fig. 4.7 Cross-sectional overview of the delaminated 1.4841/Ag4Cu/TZ3Y joint 51
Fig. 4.8 Element mapping of the reaction layer at the braze/steel interface of a 1.4841/Ag4Cu/TZ3Y joint 53
Fig. 4.9 Cross-section of a Crofer® 22 H/Ag0.5Al (PVD)/TZ3Y joint: a) PVD layer towards TZ3Y; b) PVD layer towards steel 54
Fig. 4.10 Surface morphology of a delaminated Ag0.5Al(PVD)/steel interface, a) delaminated surface at the steel interface; b) delaminated surface on the braze interface 54
Fig. 4.11 Microstructure of Crofer® 22 H/Ag0.5Al (IOT)/TZ3Y joints: (a) Braze foil in as-received condition; (b) Braze foil annealed in air at 900 ℃ for 100 h prior to brazing 55
Fig. 4.12 8YSZ surface delaminated in double shear testing 55
Fig. 4.13 EBSD analysis of the cross-section of an SOFC half-cell/Ag/TZ3Y joint 56
Fig. 4.14 Surface morphologies of TZ3Yand SOFC half-cell electrolyte (NiOx+8YSZ): a) TZ3Y surface: as received; b) TZ3Y surface: delaminated by thermal cycling; c) 8YSZ surface: as received; d) 8YSZ surface: delaminated in high temperature shear testing 57
Fig. 4.15 SEM and TEM micro-graphs of (a) delaminated SOFC half-cell surface after double shear testing at 800 ℃; (b) the braze/ceramic interface in the as-brazed state 58
Fig. 4.16 Fracture energies of the joints (pure Ag, Ag4Cu, Ag0.5Al) after air annealing at 800 ℃ with differing annealing time 60
Fig. 4.17 Microstructure of the braze/steel interface after 500 h of air annealing (a) Crofer® 22 H/Ag/TZ3Y; (b) Crofer® 22 H_v/Ag/TZ3Y 62
Fig. 4.18 Microstructure of Crofer® 22 H/Ag4Cu/TZ3Y joints after 3000 hours of annealing in air at 800 ℃ 62
Fig. 4.19 Element mappings of the reaction layer at the braze/steel interface of Crofer® 22 H/Ag4Cu/TZ3Y joints after 3000 hours of annealing in air at 800 ℃ 64
Fig. 4.20 Delamination crack and microstructure of Ag0.5Al joints after annealing in air for (a) 1500 hours and (b) 3000 hours 65
Fig. 4.21 Fracture energies of the three brazes (pure Ag, Ag4Cu, Ag0.5Al) after annealing in reducing atmosphere (Ar4Vol%H_2) at 800 ℃ 66
Fig. 4.22 Microstructure of a pure Ag joint after 3000 h of annealing in reducing atmosphere at 800 ℃ 67
Fig. 4.23 Element mapping of the cross-section of a pure Ag joint after 3000 h of annealing in reducing atmosphere at 800 ℃ 68
Fig. 4.24 Element mapping of the cross-section of a Ag4Cu joint after 3000 h of annealing in reducing atmosphere at 800 ℃ 69
Fig. 4.25 Comparison of the reaction layer at the braze/steel interface after 1500 h of annealing in reducing atmosphere at 800 ℃: a) pure Ag braze; b) Ag4Cu braze 70
Fig. 4.26 Cross-sectional view of an Ag0.5Al joint after 1500 hours annealing in reducing atmosphere at 800 ℃ (fractured during ambient temperature delamination testing) 70

Fig. 4.27 Element mapping of a Ag0.5Al joint after 3000 hours of annealing in reducing atmosphere (Ar4Vol%H_2) at 800 ℃ 72
Fig. 4.28 Stress-strain curves of as-brazed pure Ag-, Ag4Cu- and Ag0.5Al-joints at 800 ℃ (air) 73
Fig. 4.29 Schematic sketch of possible mechanisms of shear deformation of the joints in double shear specimens: a) braze deformation, b) delamination at the braze/ceramic interfaces, and c) delamination at the braze/steel interfaces 74
Fig. 4.30 Cross-sectional views of a pure Ag joint (a, b), an Ag4Cu joint (c, d) and an Ag0.5Al joint (e, f) after shear testing at 800 ℃ 75
Fig. 4.31 Cross-sectional views of a Ag0.5Al (a) and a Ag4Cu joint (b) after shear testing at 550 ℃ 78
Fig. 4.32 Failure pattern of an aged (800 ℃, 500 h, air) Ag4Cu joint after 800 ℃ shear testing: Fracture of the braze matrix 79
Fig. 4.33 Creep rate vs. stress of the three braze variants (800 ℃) 80
Fig. 4.34 Norton plot of the three brazes after annealing in air for 500 h at 800 ℃ 81
Fig. 4.35 Fracture energy of pure Ag joints with increasing number of thermal cycles 83
Fig. 4.36 Detached specimen after 500 thermal cycles (without additional delamination testing) 84
Fig. 4.37 Delamination of pure Ag joints after 250 rapid thermal cycles 84
Fig. 4.38 Fracture energy of Ag4Cu joints with increasing number of thermal cycles 85
Fig. 4.39 Delaminated Ag4Cu joint after 50 thermal cycles (after ambient temperature delamination testing) 86
Fig. 4.40 Cross-sectional view of an Ag0.5Al joint after 4825 thermal cycles 87
Fig. 4.41 Curved braze matrix overlapping the joining partners after 1000 thermal cycles 87
Fig. 4.42 Deformation rate of the braze matrix at the ceramic and steel interface during heating 89
Fig. 4.43 Deformation rate of the braze matrix at the ceramic and steel interface during cooling 90
Fig. 4.44 Single crystal matrix microstructure of a pure Ag joint in the as-brazed state [Bra12] 91
Fig. 4.45 Twinned matrix crystal structure of a pure Ag braze after 250 thermal cycles 91
Fig. 4.46 Crystallographic orientation of the matrix of a pure Ag joint after 500 rapid thermal cycles 92
Fig. 4.47 Morphology of the reaction layer in a pure Ag joint after 500 rapid thermal cycles 93
Fig. 4.48 Crystallographic orientation of the matrix of an Ag4Cu braze joint in a) the as-brazed state and b) after 220 rapid thermal cycles 94
Fig. 4.49 Grain structure of a Ag0.5Al joint in the as-brazed state: a) EBSD mapping and b) crystal orientation of the braze matrix in a {100} stereographic projection 94
Fig. 4.50 Grain structures of Ag0.5Al joints: a) Crystal structure after 463 thermal cycles, b) crystal orientation of the braze matrix in {100} stereographic projection after 463 thermal cycles, c) crystal structure after 1000 thermal cycles and d) crystal orientation of the braze matrix in {100} stereographic projection after 1000 thermal cycles 95

Tables

Tab. 2.1 Properties and fabrication requirements of SOFC sealants [Mah10] 8
Tab. 2.2 Chemical compositions of Crofer® 22 H and Crofer® 22 APU 14
Tab. 2.3 Chemical composition of 1.4841 (AISI 314 / 314L) 15
Tab. 3.1 Dimensions of the four-point bending specimens 37
Tab. 3.2 Temperature dependent parameters of the machine deformation correction curve 46
Tab. 4.1 Thickness of the reaction layer after annealing in air 65
Tab. 4.2 Shear strength in the as-brazed state at different temperatures 77
Tab. 4.3 Shear strength in the as-brazed state and after aging 78

Acknowledgement

First of all, I would like to thank all the people that have helped me during the three years of Ph.D study. Without their help, this thesis could not be fulfilled successfully.

I would like to express my earnest thanks to Prof. Dr.-Ing Singheiser and Prof. Dr.-Ing Beck for allowing me to carry out this work in the institute of Energy and Climate Research (IEK-2).

Furthermore I would like to express a deep sense of gratitude to Prof. Dr.-Ing Beck and Dr.-Ing Kuhn, who guided me with immense patience. Thanks to the inspiring discussion sessions and their constant encouragement, this thesis was able to be accomplished successfully.

I would also like to express my sincere thanks to Harald Reiners, Alexander Moser and Daniela Liebert for their help in mechanical testing; Dr. Wessel Egbert, Dr. Grüner Daniel, Jörg Bartsch and Volker Gutzeit for their help in sample preparing and microstructure analysis. I am also grateful to Dr. Jörg Brandenberg for giving me lots of scientific ideas and suggestions.

During the three years of study, our group “material mechanics” provided me with a pleasant and friendly environment, in which I had a great time and would hereby thank everyone in our group. I would also like to thank all the staff of IEK-2 who helped me during my work period in our institute.

Last but not least, I take this occasion to thank my parents and my husband He for their support and for always standing beside me.